

# UC Berkeley

## UC Berkeley Electronic Theses and Dissertations

### Title

Challenges for Synthetic Gecko Adhesives: Roughness, Fouling, and Wear

### Permalink

<https://escholarship.org/uc/item/7xq3b53d>

### Author

Gillies, Andrew George

### Publication Date

2013

Peer reviewed|Thesis/dissertation

**Challenges for Synthetic Gecko Adhesives: Roughness, Fouling, and Wear**

by

Andrew George Gillies

A dissertation submitted in partial satisfaction of the  
requirements for the degree of  
Doctor of Philosophy

in

Engineering - Mechanical Engineering

in the

Graduate Division

of the

University of California, Berkeley

Committee in charge:

Professor Ronald S. Fearing, Co-Chair

Professor Tony Keaveny, Co-Chair

Professor Lisa Pruitt

Professor Robert J. Full

Fall 2013

# Challenges for Synthetic Gecko Adhesives: Roughness, Fouling, and Wear

Copyright 2013  
by  
Andrew George Gillies

## Abstract

Challenges for Synthetic Gecko Adhesives: Roughness, Fouling, and Wear

by

Andrew George Gillies

Doctor of Philosophy in Engineering - Mechanical Engineering

University of California, Berkeley

Professor Ronald S. Fearing, Co-Chair

Professor Tony Keaveny, Co-Chair

The past decade has seen rapid advancement in gecko synthetic adhesives (GSAs) and their performance has also steadily increased. However, there still remains a gap between the capabilities of current GSAs, and the properties required for GSAs to perform as the gecko does: on natural undulating surfaces with several scales of roughness, in dirty environments where particle contamination is the norm, and for thousands or even tens of thousands of cycles. For continued progress to be made in GSAs, focus must shift from trying to attain high adhesive values under ideal conditions, to exploring the weaknesses in current GSAs and contrasting those with the principles that underpin the success of the natural gecko systems in real world challenging conditions. Here we show results from the testing and simulation of various GSA systems in rough environments, with contaminating particles of varying size and for repeated cycling. We report that with careful geometry and material consideration, large increases in 'real world' performance can be obtained, and in some cases active control can be utilized to increase controllability.

To better understand adhesion on macroscopic rough surfaces, we studied the ability of live Tokay Geckos to adhere to an engineered substrate constructed with sinusoidal patterns of varying amplitudes and wavelengths in sizes similar to the dimensions of the toes and lamellae structures (0.5 to 6 mm). We found shear adhesion was significantly decreased on surfaces that had amplitudes and wavelengths approaching the lamella length and inter-lamella spacing, losing 95% of shear adhesion over the range tested. We discovered that the toes are capable of adhering to surfaces with amplitudes much larger than their dimensions even without engaging claws, maintaining 60% of shear adhesion on surfaces with amplitudes of 3 mm. As well, Gecko adhesion can be predicted by the ratio of the lamella dimensions to surface feature dimensions. In addition to setae, remarkable macroscopic-scale features of gecko toes and lamellae that include compliance and passive conformation are necessary to maintain contact, and consequently, generate shear adhesion on macroscopically rough surfaces.

Similarly, we sought to understand the impact of surface roughness on the adhesion of two types of GSA arrays: those with hemispherical shaped tips and those with spatula shaped tips. Our simulations showed that the nanoscale geometry of the tip shape dramatically alters the macroscale adhesion of the array, and that on sinusoidal surfaces with roughness much larger than the nanoscale features, there is still a clear benefit to having spatula shaped features. Similar to experimental results found with the macroscale features of the gecko adhesive system, when roughness approaches the size of the fiber features, adhesion drops dramatically.

We have also investigated the impact of two design parameters on the dry self-cleaning capability of GSAs by experimentally testing two GSAs after fouling with small ( $1\ \mu\text{m}$ ), medium ( $3\text{-}10\ \mu\text{m}$ ) and large ( $40\text{-}50\ \mu\text{m}$ ) particles. We found that a GSA made from a hard thermoplastic with nanoscopic fibers was able to recover 96-115% of its shear adhesion after fouling with small and large but not medium particles, while a GSA made from a soft polymer and microscopic fibers recovered 40-55% on medium and large particles. Further examination by scanning electron microscopy (SEM) revealed that the soft polymer structures were not shedding the smaller particles during recovery steps, but were instead being absorbed into the surface, and that, regardless of their size, particles did not release from the soft polymer surface.

An analysis of the contact strength between fibers, particles and substrates of various dimensions and elasticity reveals that dry self-cleaning will be more effective for GSAs fabricated with smaller fiber diameters and for GSAs fabricated from materials with smaller loss functions, such as hard thermoplastics. This has important implications on the choice of materials and geometries used for GSAs when dry self-cleaning capability is a desired function in the material, and indicates that hard polymer GSAs with smaller fiber diameters are less prone to fouling.

As indicated by results of dry self-cleaning on a passive soft polymer fibrillar adhesive, we set out to design a system with active control and release of particles. We have demonstrated controllable adhesion to glass spheres with a new magnetically actuated synthetic gecko adhesive made from a magnetoelastomer composite. Capable of controlling adhesion to glass spheres  $500\ \mu\text{m}$  to  $1\ \text{mm}$ , this represents an important step in realizing an adhesive with dry self-cleaning capabilities across a wide range of particle sizes.

We also examined the behavior of high density polyethylene (HDPE) and polypropylene (PP) microfiber arrays during repeated cycles of engagement on a glass surface, with normal preload less than  $40\ \text{kPa}$ . We found that fiber arrays maintained 54% of the original shear stress of  $300\ \text{kPa}$  after 10,000 cycles, despite showing marked plastic deformation of fiber tips. This deformation was attributed to shear induced plastic creep of the fiber tips from high adhesion forces, adhesive wear or thermal effects. We hypothesize that a fundamental material limit has been reached for these fiber arrays, and that future gecko synthetic adhesive designs must take into account the high adhesive forces generated to avoid damage. Although the synthetic material and natural gecko arrays have a similar elastic modulus, the synthetic material does not show the same wear-free dynamic friction as the gecko.

The discovery of this wear mechanism has uncovered a possible pathway to the fabrication of nanoscale spatula shaped tips. Spatula tips have been shown by the rough surface simulation to greatly improve adhesion strength. Several possible fabrication pathways are proposed and preliminary results on these fabrication techniques are presented.

To my parents Barbara and Campbell, and my brother Todd who have made everything I have achieved possible, and have been there for me no matter how far I've drifted from home.

# Contents

<b>List of Figures</b>	<b>iv</b>
<b>List of Tables</b>	<b>xi</b>
<b>List of Symbols</b>	<b>xii</b>
<b>1 Introduction</b>	<b>1</b>
1.1 Background on natural gecko adhesion . . . . .	1
1.2 Previous work on gecko synthetic adhesives . . . . .	3
1.3 Motivations and current issues . . . . .	4
1.3.1 Adhesion to rough surfaces . . . . .	6
1.3.2 Fouling and dry self-cleaning of synthetic arrays . . . . .	7
1.3.3 Fibrillar surface robustness . . . . .	8
1.3.4 Testing Methodology . . . . .	8
1.4 Contributions . . . . .	9
<b>2 Adhesion to rough surfaces</b>	<b>11</b>
2.1 Adaptability of gecko gekko adhesive system to macroscopically rough surfaces	11
2.1.1 Shear adhesion observations of gecko gekko feet on macroscopically rough surfaces . . . . .	13
2.1.2 Observations of lamellar conformation and adhesion . . . . .	18
2.1.3 Discussion . . . . .	19
2.2 Concluding remarks . . . . .	24
<b>3 Fouling of fibrillar surfaces</b>	<b>25</b>
3.1 Dry self-cleaning properties of hard and soft fiber structures . . . . .	25
3.1.1 Modeling of self-cleaning with shear/static friction . . . . .	28
3.1.2 Experimental testing of dry self-cleaning on hard and soft GSAs . . . . .	32
3.1.3 Discussion of the results . . . . .	42
3.2 Dry self-cleaning with active control of soft polymer fibers . . . . .	45
3.2.1 Fabrication of magneto-elastomer composite adhesive ridges . . . . .	46



3.2.2	Results . . . . .	46
3.2.3	Modeling of fiber bending controlled by an external magnetic field . . . . .	54
3.3	Concluding remarks . . . . .	58
<b>4</b>	<b>Fibrillar surface robustness</b>	<b>59</b>
4.1	Material limits of hard polymer fibrillar surfaces . . . . .	59
4.1.1	Experimental testing of hard polymer thermoplastic arrays . . . . .	59
4.1.2	Mechanisms of failure . . . . .	65
4.2	Preliminary work on spatula fabrication . . . . .	68
4.3	Concluding remarks . . . . .	75
<b>5</b>	<b>Adaptability of synthetic gecko arrays on rough surfaces</b>	<b>77</b>
5.1	Fiber setup . . . . .	77
5.2	Surface characterization and load-drag-pull path . . . . .	78
5.3	Fiber tip contact . . . . .	80
5.3.1	JKR contact model . . . . .	81
5.3.2	Kendall peel model . . . . .	81
5.4	Numerical simulation . . . . .	83
5.5	Comparison of JKR and Kendall peel contact models . . . . .	84
5.6	Arrays on sinusoidal surfaces . . . . .	88
5.7	Discussion of the results . . . . .	91
5.8	Concluding remarks . . . . .	91
<b>6</b>	<b>Conclusion</b>	<b>94</b>
	<b>Bibliography</b>	<b>96</b>

# List of Figures

1.1	Structural Hierarchy of the gecko adhesive system. From Autumn <i>et al.</i> [9]. . . . .	2
1.2	A longitudinal section through a series of lamellae of the tokay gecko ( <i>Gekko gekko</i> ) lateral to the phalanges. From Russell [113]. . . . .	3
1.3	A survey of GSA structures including examples of soft polymer structures by Askak <i>et at.</i> [3], Varenberg and Gorb [131] and Day <i>et al.</i> [29], stiff polymer structures by Lee <i>et al.</i> [85, 86], Xue <i>et al.</i> [138], Zhang <i>et al.</i> [145] and Jeong <i>et al.</i> [67], and carbon nanotube structures by Ge <i>et al.</i> [39] and Qu and Dai [108]. . . . .	5
2.1	Lamellae observed on the toe of a live Tokay gecko ( <i>Gecko gekko</i> ), showing example measurements of the lamellar wavelength and amplitude. . . . .	14
2.2	Creation of the surfaces. (A) A 3D wax mold was printed. (B) Polyurethane (PU) was then cast into the mold and allowed to cure. (C) The PU surface was then removed from the mold. (D) Cross section of the surface showing amplitude $A$ and wavelength $\lambda$ . (E) The flat PU control surface as well as three example surfaces used in the various conditions. . . . .	15
2.3	(A) The experimental apparatus showing how the simulated steps were performed with the Tokay geckos. (B) A sequence of stills taken from video of a foot drag on a surface with amplitude 3 mm and wavelength 5 mm. (c) the testing methodology in which the rear foot is testing on the PU flat control surface, then 3 trials are performed on the condition being tested, and finally, the foot is again tested on the flat PU control surface afterwards. . . . .	17
2.4	Shear (blue line) and normal (green line) adhesion data from a single load-drag-pull step of a Tokay gecko on a sinusoidal surface with an amplitude of 2 mm and a wavelength of 3 mm. . . . .	18

2.5	Percent shear adhesion across surfaces that vary in amplitude (A) and wavelength (T) relative to a flat control surface. (a,b) Percent shear adhesion as a function of amplitude with wavelength held constant across low (a) and high (b) wavelengths shown in inset. (c, d) Percent shear adhesion as a function of wavelength with amplitude held constant across low (c) and high (d) amplitudes shown in inset. Adhesion decreased significantly with increasing amplitudes and decreasing wavelengths (ANOVA $P < 0.001$ ; error bars represent one standard error).	20
2.6	Photos taken from video of load-drag-pull trials on several, engineered rough surfaces. At wavelengths below the lamella dimensions (a, b) the roughness is too large for the toes and lamella to conform (black bracket showing lamellae only contacting tips of ridges). The intermediate surface dimensions (c, d) approximately correspond to the point at which a significant loss in adhesion is measured, where lamella can slightly conform, but the toes cannot (white arrows). At larger surface dimensions (e, f), the lamella and toes can conform to the surface, and there is no significant loss in shear adhesion (black arrow).	21
2.7	Percent reduction in maximum shear force from a flat control surface vs available area for contact in the top 0.87 mm of the sinusoidal surface. Russell and Johnson [117] suggested that increased available area for contact may predict an increase in adhesion, however we found this was not significant ( $r^2 = 0.29$ ) showing that a more complex metric is needed to predict surface adhesive forces (error bars are 95% confidence intervals).	22
3.1	A contact analysis outlined by Hansen and Autumn [53] reveals that with larger particle sizes and smaller spatula geometries, self cleaning is more likely.	27
3.2	Schematic of fiber, contaminant particle, and substrate. The interfacial contact areas $A_{f,p}$ and $A_{p,s}$ depends on the materials properties and the normal load $L$ . These areas and the applied lateral load $F$ determine the shear stress acting at each interface. Plot contributed by Puthoff, in [43], used with permission.	30
3.3	Sliding criteria for particle-surface and fiber-particle interfaces. The critical sliding forces for each contact are given by $F_{f,p}^*$ and $F_{p,s}^*$ . For the given parameters, sliding threshold forces are smaller for the fiber-particle interface; this produces self-cleaning of the fiber. Plot contributed by Puthoff, in [43], used with permission.	30
3.4	The cleaning parameter $\rho \equiv F_{f,p}^*/F_{p,s}^*$ as determined by both fiber radius $R_f$ and contaminant particle radius $R_p$ . Self-cleaning by shear works best for small fibers and/or large particles. Plot contributed by Puthoff, in [43], used with permission.	31

3.5	The cleaning parameter $\rho$ for various combinations of fiber modulus $E_f$ and intrinsic loss parameter $E_{f,\infty}/E_{f,0}$ . Self-cleaning is poorest at high $E_{f,\infty}/E_{f,0}$ . Plot contributed by Puthoff, in [43], used with permission. . . . .	33
3.6	Fabrication of the PP and PDMS fibrillar structures. Polypropylene structures are made by (a) molding into a track-etched membrane filter in a hot press and then (b) etching away the filter with methylene chloride. PDMS structures are fabricated by first (c) cutting a $37 \mu\text{m}$ thick steel shim into a 'comb' shape with a UV ablation laser (d) then with a CNC tool, the comb is used to make progressive cuts into a wax surface. (e) Once cut, PDMS is cast onto the wax mold and (f) released by peeling. . . . .	34
3.7	(a) Force displacement apparatus block diagram. (b) Load-drag-pull step on glass surface. (c) Spacing of steps after fouling to avoid stepping in contaminated areas of the glass slide. (d) Particles shed on glass after successive steps with a fouled PP fibrillar sample. . . . .	35
3.8	(a) An unused clean fabricated polypropylene fibrillar surface. (b) An unused clean fabricated PDMS fibrillar surface. . . . .	36
3.9	A typical load-drag-pull step for: (a) a polypropylene fiber sample on a clean glass substrate. (b) A PDMS fiber sample on a clean glass substrate. . . . .	38
3.10	The shear recovery ratio $\Gamma = (F_{dirt.n})/(F_{clean.n})$ for the polypropylene fibrillar surface after fouling with (a) small (mean= $96 \pm 11\%$ ) (b) medium (mean= $36 \pm 20\%$ ) and (c) large particles (mean= $115 \pm 12\%$ ). (N=3 samples for each particle type, error bars are $\pm$ S.D.) . . . . .	39
3.11	(a) Polypropylene fibrillar structures 40 steps after fouling with $1 \mu\text{m}$ polystyrene spheres, which can be seen between fibers (PS). (b) Fibers fouled with 3-10 $\mu\text{m}$ glass spheres, where some can be seen deeply embedded (EM) between fibers and (c) Fibers contaminated with 40-50 $\mu\text{m}$ glass spheres, only one of which could be found sitting on top (OT) on the sample 40 steps after fouling. . . . .	40
3.12	The shear recovery ratio $\Gamma = (F_{dirt.n})/(F_{clean.n})$ for the PDMS fibrillar surface after fouling with (a) small (mean= $99 \pm 4\%$ ), (b) medium (mean= $40 \pm 15\%$ ) and (c) large particles (mean= $55 \pm 18\%$ ). (N=3 samples for each particle type, error bars are $\pm$ S.D.) . . . . .	41
3.13	(a) PDMS fibrillar structures 40 steps after fouling with $1 \mu\text{m}$ polystyrene spheres, which can be seen deeply embedded in the fiber tips (PS). (b) Fibers fouled with 3-10 $\mu\text{m}$ glass spheres, where many particles can be seen embedded on the outside of the fibers (EM) (c) Fibers contaminated with 40-50 $\mu\text{m}$ glass spheres after 40 recovery steps. Particles can be readily seen embedded between the fibers (EM). . . . .	43
3.14	Comparison of the PP and PDMS fiber structures dry-self cleaning recovery ratio across the various particle sizes tested. . . . .	44

3.15	Fabrication of the magnetoelastomer microridges. (a) A wax surface is inscribed with a custom-built 3 axis CNC machine. (b) The magnetoelastomer material is cast into the wax mold, and allowed to cure in a magnetic field. (c) While curing, the carbonyl iron particles align to form chains along the direction of the magnetic field. . . . .	47
3.16	ME microridge, viewed from the side, showing chains of carbonyl iron particles (white), cured into alignment with a magnetic field (dashed black line). . . .	48
3.17	Results from a sphere indentation test show that vertical ridges are greater than 10 times more compliant at indentation depths of 125 microns, as compared to the flat actuated ridges, which at the same indentation level have the same compliance as a flat control surface (N=3, error bars are 1 s.d.). Vertical ridges also fall under the Dahlquist criterion for tack. . . . .	49
3.18	(a) SEM of the completed magnetoelastomer microridges. The microridges are 325 microns long, 15 mm wide, and taper from 100 microns at their base to less than 10 microns at the tip. (b) Actuation of the ridges, as seen from the top and side. In the presence of a magnetic field, the ridges completely flatten. . . . .	50
3.19	The microridge deflection from vertical as a function of the external magnetic field strength. . . . .	51
3.20	(a) Schematic of the 2-axis wire cantilever apparatus used to test normal and shear adhesion between a glass sphere and the ME composite microridges. (b, c) Images of a sphere adhering to the microridge array, showing normal and shear displacements. (Video of test attached as supplementary information) .	52
3.21	Data from sphere pull-off tests show that the microridge surface has a strong shear-induced normal adhesion effect while the ridges are vertical (red). Once ridges are activated and lie flat, the material acts the same as a smooth control sample and has 10x less normal adhesion (blue). A smooth flat control surface (green) shows slightly larger adhesion than the flat actuated ridges. Open circles are 1mm spheres, asterisks are 500 micron spheres. . . . .	53
3.22	(a) A proof-of-concept test in which the ME composite microridges are used to remove particles from a surface before being transported and actuated to release the particles into an adjacent hopper. (b) Stills from video showing microridges (c) picking the particles off a surface and then (d) actuation of the microridges, causing particle detachment into the hopper. A video of the test is attached as supplementary information. . . . .	54
3.23	Theoretical analysis of beam angle has good agreement with a macroscale prototype of the ME composite microridges, and shows the beam angle dependence on the distance from a 2.5x2.5x1.25 cm neodymium magnet. . . . .	56
4.1	(a) Molding of HDPE film into PC filter (b) Etching of PC filter in methylene chloride. . . . .	60

4.2	Contact area of the fiber sample is calculated by total internal reflection. . .	61
4.3	Load-drag-pull steps for (a) HDPE and (b) PP fiber samples for trial 50, 150 and 300, showing the three phases of a single trial and correlation between cycles 50, 150 and 300. . . . .	62
4.4	Maximum shear force and the corresponding normal force for 300 load-drag-pull steps of (a) HDPE and (b) PP fibers showing no significant change in peak force over the course of the first 300 trials. For 10,000 load-drag-pull steps of (c) HDPE and (d) PP fibers, shear forces eventually start to decrease.	63
4.5	SEM images of HDPE (left column) and PP (right column) after 0, 150, 300 and 10,000 cycles, showing progressive plastic deformation of the fibers over the course of the trials. . . . .	64
4.6	Progressive deformation observed on the fibrillar samples can be explained by visco-plastic creep deformation as described by Freed [37]. Stresses calculated at the fiber tips are consistent with values required to induce creep deformation.	65
4.7	(a) Example image of spatula on <i>gecko gekko</i> (Image courtesy of Kellar Autumn) (b) Ideal angled fiber and terminal spatula plate geometry shown in various literature to be critical to high performance synthetic gecko adhesives [9].	69
4.8	A variety of possible tip fabrication processes and parameters are presented for fibers still in a mold (a)-(c) and free standing (d)-(e). Spatula plates fabricated by: (a) flattening with a smooth tool with stress, $\sigma$ , tip height, $\lambda$ , and approach angle $\theta$ . (b) Abrasion/polishing of the mold surface with stress, $\sigma$ , surface roughness, $\Sigma$ , and polishing time, $\Delta t$ . (c) Tearing/scratching of fiber tips with a cutting tool with stress, $\sigma$ , and approach angle $\theta$ . (d) repeated cycles of shearing resulting in creep deformation with stress, $\sigma$ , approach angle $\theta$ , and number of cycles. (e) Hot melting of free standing fiber tips with temperature, time, $\Delta t$ , and stress, $\sigma$ . . . . .	71
4.9	An example of a scratch map for PE (taken from [20]). The picture shows results from scratch tests performed at room temperature for a range of cone angles and normal loads and at a scratching velocity of 2.6 mm/s. . . . .	72
4.10	(a) Epoxy fibers fabricated via capillary wetting into an AAO template with 200 nm pores, then post processed with a sanding step. (b) Detail of the fiber tips showing slight deformation of the tips. . . . .	74
4.11	(a) An AAO template seeded with 900 nm PS microspheres before filling with polymer. (b) HDPE hairs with reduced density formed by heat molding in a PS seeded AAO template. . . . .	74
4.12	Proposed manufacturing process for fabrication of spatula plates. (a) Starting with fabricated stiff nanofiber arrays (b) Spin or dip coating to protect fibers during post processing (c) Partial etch of the protective coating to expose nanofiber tips (d) Post processing of tips by polishing or deformation (detail outlined in work plan) (e) Final etch release of fibers with spatula tips. . . .	75

5.1	(a) Modeled approximation of the fiber and the relevant parameters indicated. The fiber is modeled with an axial spring and a torsional spring at its based that approximates fiber bending with a pseudo-rigid body model [57]. (b) Hemispherical tips approximated by the JKR contact model and (c) Spatula tips approximated by the Kendall peel model. . . . .	79
5.2	Illustration of the Load-Drag-Pull path. . . . .	80
5.3	Adhesion limits for both the Johnson-Kendall-Roberts model as well as the Kendall peel model. A fiber undergoing axial strain and bending as outlined previously will fall within this force space as a function of the shear and normal load on the fiber, $F_x$ and $F_y$ , as well as the local surface angle, $\theta_{sf}$ . Fibers will remain in contact as long as the forces are within the adhesion envelope. Fiber properties and dimensions are given in Table 5.1. . . . .	82
5.4	A snapshot of the simulation running on a sinusoidal surface. Fibers in red are in contact, fibers in blue are out of contact. . . . .	83
5.5	Example Load-Drag-Pull simulation results for 250 hemispherical tipped fibers using spatula tips with Kendall peel theory plotted in (a) force and (b) time space, and JKR contact theory in (a) force and (b) time space. The green star indicates the point of maximum tensile load on the array and the corresponding shear load. Each simulation was run on a spherical surface with a radius of 2 cm, an indentation depth of 2 $\mu m$ and an initial fiber inclination of 51 degrees. . . . .	86
5.6	(a) Maximum adhesion forces and (b) mean forces during drag for an array of 250 fibers with hemispherical tips modeled with JKR theory for surface indentation depths of 2-5 $\mu m$ . Maximum tensile forces are plotted as absolute values, mean forces are plotted as tensile being negative. . . . .	87
5.7	(a) Maximum adhesion forces and (b) mean forces during drag for an array of 250 fibers with spatula terminated tips for surface indentation depths of 2-5 $\mu m$ . Maximum tensile forces are plotted as absolute values, mean forces are plotted as tensile being negative. . . . .	87
5.8	A comparison of the hemispherical tip JKR model fibers and the spatula tip Kendall model fibers for $\Delta = 3\mu m$ indentation on a spherical surface of 2 cm radius for (a) absolute maximum force, (b) mean force during drag and (c) maximum pulloff in force space. . . . .	89
5.9	Simulation of 250 hemispherical JKR array of fibers on sinusoidal surfaces of amplitudes 1 to 5 $\mu m$ and wavelengths 1-30 $\mu m$ showing (a) mean normal and shear force during drag and (b) absolute maximal adhesion (tensile) during the trial. Fibers have an initial angle of 60°. . . . .	90

- 5.10 A comparison of the hemispherical tip JKR model fibers and the spatula tip Kendall peel model fibers for sinusoidal surfaces of amplitudes 1 to 5  $\mu\text{m}$  and wavelengths 1-30  $\mu\text{m}$  showing (a) mean normal and shear force during drag and (b) absolute maximal adhesion (tensile) during the trial. Fibers have an initial angle of  $60^\circ$ . Adhesive properties of the arrays on a flat surface are marked with star for Kendall and circle for JKR on the far right of the plot. 92



# List of Tables

4.1	Comparison of failure modes. . . . .	67
4.2	State of the art in spatula-like synthetic tip features. Scale bars: $1\mu m$ for 1,2,4,5 and $2\mu m$ for 3. . . . .	70
5.1	Fiber properties used for simulation. . . . .	79

# List of Symbols

$A$	Hamaker constant	6
$R$	Sphere radius	6
$P$	Adhesive pressure	6
$D$	Surface gap	6
$U_{el}$	Stored elastic energy	6
$\delta\gamma$	interfacial free energy per unit surface area	7
$A$	Surface amplitude	13
$T$	Surface wavelength	13
$R_p$	Dirt particle radius	25
$W_{pw}$	Particle-substrate interaction energy	25
$W_{ps}$	Spatular-particle interaction energy	26
$R_s$	Spatula radius	26
$\tau^*$	Interfacial shear strength	28
$F_f$	Static friction limit	28
$G^*$	Interfacial shear modulus	29
$E$	Young's Modulus	29
$\rho$	Cleaning parameter	31
$\Phi$	Loss function	32
$\Gamma$	Recovery ratio	37
$R_f$	Fiber radius	42
$\nu$	Poisson's ratio	46
$I$	Second moment of area	55
$H$	Magnetic field strength	55
$E_{eff}$	Effective elastic modulus	57
$K_t$	Fiber bending stiffness	77
$K_a$	Fiber axial stiffness	78
$\mu$	Friction coefficient	81
$W_{ad}$	Work of adhesion	81
$\alpha$	Peel angle	81
$\Delta$	Surface indentation depth	84

## Acknowledgments

When I first arrived at Berkeley in the summer of 2008, I remember the distinct feeling of being way in over my head. The enormity of the path ahead, and the uncertainty and mystery surrounding just how one carves their niche in academia and makes a significant contribution seemed daunting at best. I was told a story early on about how research is analogous to exploring an unknown cave or pre-dawn mountainside. We feel around in the dark, living in the small island of terrain illuminated by our headlamps. We have a vague idea of where we want to end up, and we understand our immediate surroundings, but the path connecting them is uncertain. And thus, we wander. The path winds, there are highs and there are lows, and there are also dead ends requiring retreat back to known handholds and landmarks. Eventually progress is made and the goal is reached, but in hindsight the path is bizarre and unanticipated.

What is implied in the story is a sense of isolation, that the trip is one of self reliance and independent fortitude. But this couldn't be further from the truth. The people I've met in Berkeley, my colleagues, my labmates, and my friends and family back home have been the single biggest factor in getting me where I am today.

My advisor, Ron Fearing, has been endlessly supportive, and always available to discuss issues and provide motivation with new ideas. Other advisors in the mechanical engineering department, specifically Lisa Pruitt and Tony Keaveny, have also graciously helped me during my visits to Etcheverry. As well, Bob Full, who's political prowess and magic with words has given me an appreciation for the art of clear and well packaged communication.

The members of the Biomimetic Millisystems Lab have also been a source of technical and personal support, and I have earned both lifelong friendships as well as a network of some of the best engineers I've ever worked with. From Bryan Schubert and Aaron Hoover who took the time to show me the ropes when I was just getting going, to Paul Birkmeyer, whos energy for lively brainstorming sessions kept us going well into the night, to Nick Kohut whos insightful commentary allowed me to gain new perspectives, as well as Kevin Peterson, Andrew Pullin, Fernando Bermudez, Ethan Schaler, Duncan Haldane, Austin Buchan and Brian Bush who have all been a great source of support. Many friends and peers have also helped in shaping this journey, including Mark Kopec, Scott Laughton, Vince Romanin, Dave Lettieri, Gabe and Britt Hein, Ashley Shimell, Rich Winslow, Ben Kehoe, George Hines, Jared Garvey, Maritza Ruiz, Matt Lucas, Matthew Beres and Allison Stephens.

And most importantly, I'd like to thank my parents back home, Barbara and Campbell Gillies, and my brother Todd Gillies who have been an endless source of support.

In the end the path isn't nearly as dark as it seemed at the outset. The people above were all there to aid my way. But when I reflect back I can't help but think what a long strange trip its been.

# Chapter 1

## Introduction

### 1.1 Background on natural gecko adhesion

Watching a gecko scramble up a tree or across a ceiling at almost imperceptible speeds can only leave one wondering how such acts are possible. This wonder has led to centuries of physical observations of the gecko adhesive system, as well as many in-depth anatomical studies of the beautiful and complex structures found on the gecko's toes. Much of the anatomy has been thoroughly described, and has revealed a system that is hierarchical in nature; spanning size scales from the millimeter level to the nanometer level that all work in concert to give the gecko its special adhesive capabilities. Taking a trip from the largest sized structures all the way down to the smallest structures is warranted here since it will set the stage for later discussions surrounding the function of the gecko adhesive at each independent size scale. Here we specifically give a description of the adhesive system of a particular gecko species, the *Gecko gekko* or Tokay gecko. Although the entire gecko body is necessary for climbing, it can be argued that the adhesive system starts with the feet and toes, which measure 5 mm in length and 2 mm in width, and are terminated with a curved claw. At the proximal end of the toe is the hyperextensible phalanges, which are connected with the flexor tendon and allows the toe to hyperextend away from the surface in an action known as digital hyperextension [112, 114]. Each toe is highly vascularized, and connected to sinuses which run the length of the toe distal to the phalanges. On the bottom surface of the toe, there is an array of overlapping scale-like structures known as lamella or scaps. Connective tendons known as the lateral digital tendon system connect each of these lamella to the metatarsophalangeal joint capsule and the flexor musculature [113]. By action of the digital tendon system, the lamella can be individually acted upon to move them into an out of contact with a surface sequentially [114]. Each lamella consists of adipose tissue terminated by an array of hairs known as setae, which are generated by an outer epidermal layer that lies on the outer surface of the lamella [113], with a density of approximately 5300 setae/mm<sup>2</sup>, meaning each toe has about 150,000 setae [110]. Each setae consists of a flexible

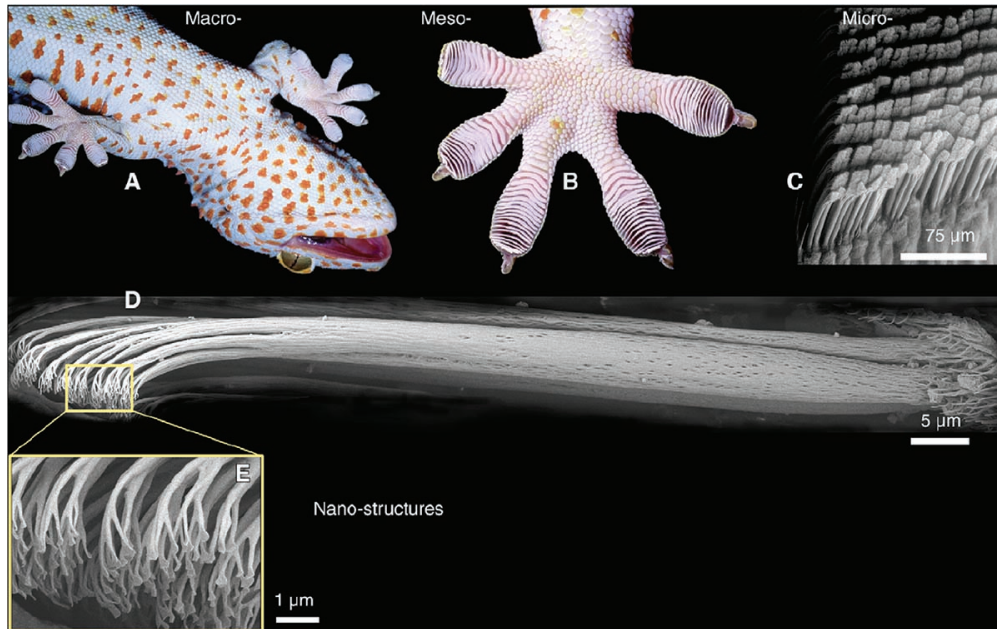


Figure 1.1: Structural Hierarchy of the gecko adhesive system. From Autumn *et al.* [9].

shaft and measures  $4.7 \mu\text{m}$  in diameter and  $30\text{-}130 \mu\text{m}$  long [110]. The setae branch multiple times along the length of the hair, each split terminating in a plate-like structure known as the spatula. Each seta terminates in approximately 100-1000 spatular plates that measure  $200 \text{ nm}$  wide,  $200 \text{ nm}$  long and taper to  $10 \text{ nm}$  at their distal end [110, 8].

Whole body adhesion studies of the *gecko gekko* have revealed that each foot can adhere with a force of approximately  $10 \text{ N}$  [64]. With an average mass of  $50 \text{ g}$ , this implies that a gecko can support more than 40 times its own body weight with only its two front feet! Autumn *et al.* first measured the adhesive force of a single gecko foot hair, reporting a pull-off force of  $194 \mu\text{m}$  per seta [8]. More interesting than the actual pull-off force measured was the discovery of the action that was necessary to engage and disengage the seta. Namely that the macroscopic orientation and pre-load increased the adhesive force parallel to the surface to 600 times greater than frictional measurements of the material. A small perpendicular preload ( $5\text{-}10 \mu\text{m}$ ) followed by a small displacement of the seta parallel to the surface ( $5 \mu\text{m}$ ) was necessary for engagement and resulted in drastically larger adhesive forces. As well, a critical angle of detachment was discovered, that was shown to be independent of pulling force. Above approximately  $30$  degrees, setae were found to detach. Autumn *et al.* hypothesized that the digital hyperextension observed in the gecko during engagement and disengagement allowed the setae to be easily attached and released by crossing this angular threshold [8].

Although gecko adhesion has fascinated humans and piqued the interest of scientists for thousands of years, significant insights into the physical principles that give rise to the adhe-

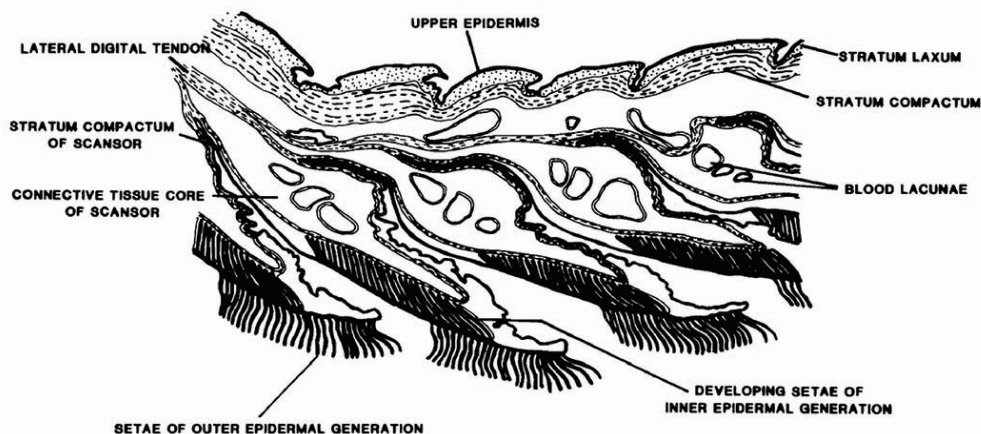


Figure 1.2: A longitudinal section through a series of lamellae of the tokay gecko (*Gekko gecko*) lateral to the phalanges. From Russell [113].

sive properties have only recently been uncovered. Researchers have revealed that the geckos amazing ability to climb vertically or inverted on nearly any surface can be attributed to van der Waals forces generated between the surface and the millions of hierarchical nanohairs made from  $\beta$ -Keratin (Young's modulus  $\approx 1.5$  GPa) [10, 9], as described above. Through a clever experiment involving highly polarized hydrophobic and hydrophilic surfaces, they were able to reject competing hypothesis that thin-film capillary forces were responsible for adhesion. This resulted in the extremely important realization that the adhesive properties of gecko setae are only dependent on the size and shape of the spatular tips, and are not strongly affected by surface chemistry - ie. material property [10]. The implication was that smaller spatulae will result in a greater adhesive force per unit area, and that continued subdivision of terminal features would result in a greater surface density, and therefore enhance the adhesive properties. This discovery paved the way for the development of artificial dry fibrillar based adhesives known as Gecko-inspired Synthetic Adhesives (GSAs) [6, 81].

## 1.2 Previous work on gecko synthetic adhesives

Since the Autumn *et al.* [10] discovery of the principles underlying the gecko adhesive system, there has been an explosion in interest from investigators trying to replicate the form and function of fibrillar adhesives, and over 250 publications have appeared since 2000, and are well documented by the gecko adhesion bibliography recorded and maintained by Dr. Ron Fearing at <http://robotics.eecs.berkeley.edu/~ronf/Gecko/gecko-biblio.html>.

Autumn [123] has identified seven benchmark properties that are characteristic of gecko-like adhesives, which are (1) anisotropic attachment, (2) a high adhesion coefficient, (3) a low detachment force, (4) material-independent adhesion, (5) self-cleaning, (6) anti-self-adhesion,

and (7) a nonsticky default state. Although the overall adhesive strength of GSA systems is important, these benchmark properties are equally important since they give rise to the controllable aspect of the gecko adhesive system that make them interesting to investigators and desirable as a new technology.

Recently, GSAs [6] have been made using a variety of fabrication techniques and materials. These adhesives generally consist of a surface covered in millions of micro to nanoscopic fibers, the dimensions of which allow for the effective stiffness of the array to be reduced while maintaining morphological stability [124]. Structures can loosely be categorized into three types: those consisting of primarily low elastic modulus polymers (Young's modulus  $\leq 10$  MPa) [3, 122, 131, 74, 94, 45, 99, 29], high elastic modulus polymers (Young's modulus  $\approx 1$  GPa) [145, 40, 80, 119, 67], and arrays of carbon nanotubes [141, 39, 108].

The soft polymer adhesives generally consist of larger dimension structures ( $\approx 10\mu m$ ), fabricated by first forming a negative mold either through direct machining of a rigid substrate such as wax [54, 29], or using traditional microfabrication techniques such as photolithography [95, 30], and casting an elastomeric material such as polydimethylsiloxane (PDMS). Once the elastomer is cured, it is peeled from the mold to reveal the fibrillar structures. These adhesives are generally characterized by high normal adhesion strengths.

The hard polymer adhesives generally consist of smaller dimension structures ( $\approx 1\mu m$ ), typically fabricated by filling micro porous templates by injecting thermoplastic polymer through the application of heat and pressure [85, 138]. Other techniques for hard fibrillar surface fabrication involve fabrication of a soft mold using traditional photolithography or nanosphere lithography techniques [80]. In either case, the negative mold must either be etched away or be made of a soft deformable material to release the hairs due to the higher stiffness and smaller surface dimensions of the fibrillar features, which is in contrast to the soft fibrillar structures which can be peeled from the mold due to the flexibility of the elastomeric features. Stiff fibrillar arrays generally generate less normal adhesive forces, however they generate extremely high friction forces.

Arrays of carbon nanotubes or nanowires have also been fabricated via various chemical vapor deposition techniques [39, 108] and tested for adhesive properties. These adhesives show very high normal adhesion, however high preloads are generally required to engage the adhesives, and adhesive properties degrade rapidly with repeated use [108].

A recent thorough review of the current fabrication techniques and current challenges has also been compiled by Sameoto and Menon [118].

### 1.3 Motivations and current issues

The past decade has seen rapid advancement in GSAs and their performance has also steadily increased. Many of the benchmark properties identified by Autumn have been achieved to some degree, and adhesive forces up to  $30 N/cm^2$  in shear are reported for structures presented in this body of work [41], and another example exhibiting up to  $21.9 N/cm^2$  in

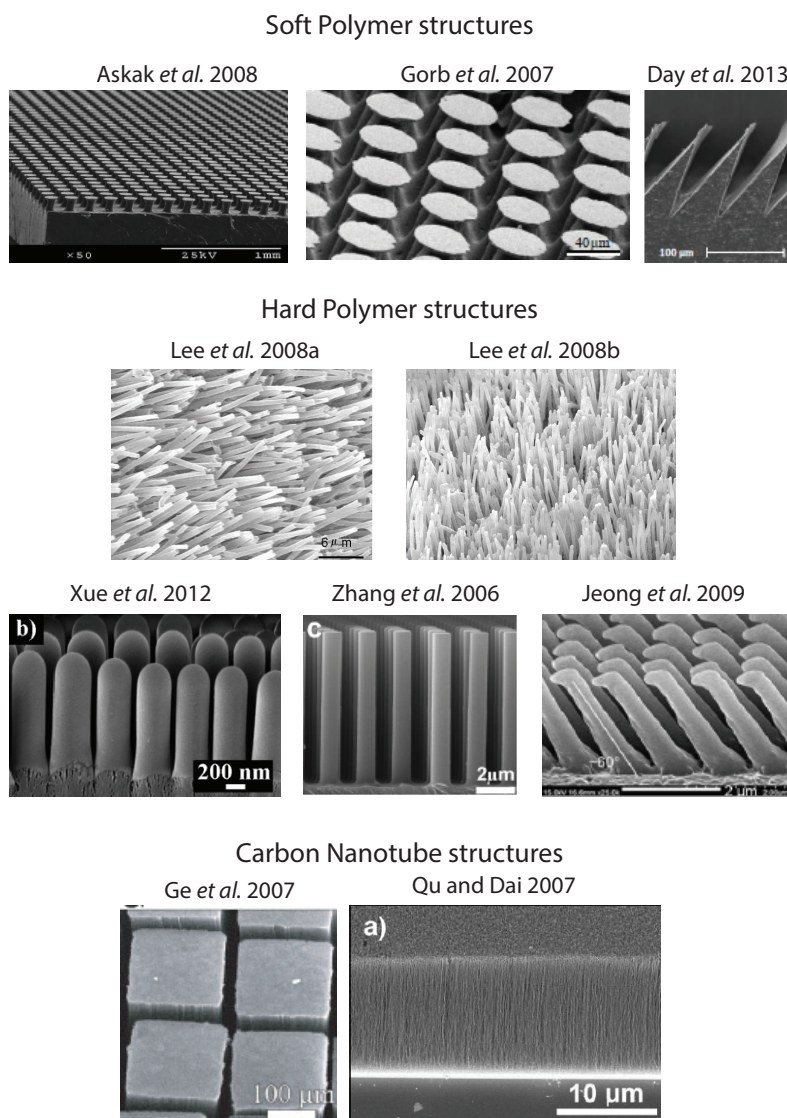


Figure 1.3: A survey of GSA structures including examples of soft polymer structures by Askak *et al.* [3], Varenberg and Gorb [131] and Day *et al.* [29], stiff polymer structures by Lee *et al.* [85, 86], Xue *et al.* [138], Zhang *et al.* [145] and Jeong *et al.* [67], and carbon nanotube structures by Ge *et al.* [39] and Qu and Dai [108].



the normal pulloff direction [28], and many others reporting adhesive values in the 5-10  $N/cm^2$  range [118]. However, these reported values have been recorded under ideal surface conditions, namely on smooth glass surfaces that have been thoroughly cleaned, and the adhesives are generally only tested for a few cycles. Therefore, there still remains a gap between the capabilities of current GSAs, and the properties required for GSAs to perform as the gecko does: on natural undulating surfaces with several scales of roughness, in dirty environments where particle contamination is the norm, and for thousands or even tens of thousands of cycles. For continued progress to be made in GSAs, focus must shift from trying to attain high adhesive values under ideal conditions, to exploring the weaknesses in current GSAs and contrasting those with the principles that underpin the success of the natural gecko systems in real world challenging conditions.

### 1.3.1 Adhesion to rough surfaces

The variety of surfaces found in nature pose a formidable challenge to any adhesive designer. Often these surfaces have roughnesses at a variety of length scales, ranging from nanometers to large undulations on the centimeter scale. These roughnesses can be critical, as it has been shown that just a few nanometers in roughness is enough to disrupt the adhesion between clean elastically hard surfaces [101], and that a root mean square (RMS) roughness of only 1  $\mu m$  is enough to completely remove the adhesion between a soft rubber with a Young's Modulus of 1 MPa and a hard flat substrate [103]. This is due to the nature of the van der Waals bonds that give rise to the adhesive forces between solids. The strength of this bond between two spheres will have an adhesive force of [66]:

$$F = AR/12D^2 \quad (1.1)$$

Where  $A$  is the Hamaker constant, taken to be  $10^{-19}$  for typical solids [66]. With spheres of radius  $R = 1$  cm separated by a gap of  $D = 0.2$  nm, the adhesive force will be  $2 \times 10^{-3}$  N. When this gap is increased to  $D = 10$  nm, the adhesive force drops to  $10^{-6}$  N, a factor of 2500. Similarly, two planar surfaces will show an adhesive pressure of [66]:

$$P = A/6\pi D^3 \quad (1.2)$$

Plates separated by 0.2 nm theoretically will show an adhesive pressure of  $10^8 N/m^2$ , but this is reduced by 5 orders of magnitude when the gap is increased to  $D=10$  nm. This dramatic drop in the van der Waals bond with separation gap outlines the importance of intimate contact between the adhesive structure and the counter-surface.

In the case of primarily elastic adhesives such as the gecko adhesive system, adhesive contact will be maintained as long as there is an energetic balance between the elastic energy stored in the material and the surface binding energy arising from contact. Stored elastic energy,  $U_{el}$ , arises from the strains required to bring the material into contact with the surface, and the binding or surface energy,  $\delta\gamma A$  is formed when two surfaces are brought

together, where  $\delta\gamma$  is the change in the interfacial free energy per unit surface area and  $A$  is the true area of contact [103]. Reaching this equilibrium is challenging on rough surfaces, as the adhesive material must deform much more in order to form true contact area with the surface, and for stiffer materials, this puts the energetic equilibrium out of balance leading to detachment. To accommodate this, the gecko adhesive reduces the necessary stored elastic energy by having thin terminal fibers, effectively reducing the stiffness of the surface from the bulk modulus of  $\approx 2$  GPa to  $\approx 85$  kPa [9]. However, due to the varying scales of roughness found on natural surfaces, a single level of thin hairs is not sufficient. To 'reach' and make contact with nanoscale roughness the hairs need to be on the order of nanometers, but if the same hairs were to be used to accommodate millimeter scale roughness, the hairs would be extremely weak and self condense [102]. Thus the system involves several branching scales of hairs and structures which are postulated to be necessary at complying to the varying levels of roughness found on natural surfaces.

Although the majority of recent studies on the gecko adhesive system and work on GSAs have focused on the nanoscale or on smooth surfaces (with several notable exceptions [60, 77, 103, 116, 106, 14, 83, 109]), it is clear that an integrated approach must be taken that considers the relationship between the surface roughness, the size of the adhesive structures, and their ability to conform at a variety of length scales [102]. Understanding the abilities and limitations of these structures on varying length scales of roughness is necessary to create an adhesive that is able to adhere to naturally rough surfaces.

### 1.3.2 Fouling and dry self-cleaning of synthetic arrays

Adhesives in the natural world also must overcome the large amounts of contaminants found on surfaces such as dirt and dust or loose frangible material such as a sandstone wall. Traditional pressure sensitive adhesives (PSA) are made using soft viscoelastic polymers (Young's modulus  $\leq 100$  kPa at 1 Hz [26, 104]), and will collect dirt and lose adhesion rapidly with repeated use, often within just a couple cycles [84].

For the gecko to operate continually in its environment, it must be able to cope with this contamination. Recently, it has been shown that the gecko adhesive structures can shed particles after fouling in order to preserve the adhesive properties of the foot pads [53]. This dry self-cleaning occurs by an energetic disequilibrium between the adhesive forces attracting a dirt particle to the substrate and those attracting the same particle to one or more spatulae.

Although GSAs have shown several of the same remarkable behaviors as the gecko including directional adhesion, strong attachment with minimal preload, and quick detachment [99, 119, 84], minimal attention has been paid to dry self-cleaning, with only a handful of studies that directly address fouling and contamination issues in dry environments [84, 43, 42], with the aid of water droplets moving across the adhesive surface and taking advantage of the lotus effect [144, 129, 121] and theoretical treatments considering the mechanics behind dry self cleaning [63, 105, 103]. While dry self-cleaning has been exhibited with GSAs, this effect has only been shown across a narrow range of particles and materials

choices. A better understanding of the interaction between particles, surfaces and adhesive structures will be required before adhesives can be employed in use cases involving repeated cycles in dirty environments.

### 1.3.3 Fibrillar surface robustness

Robustness of the adhesive is another critical component that must be carefully considered for high cycle applications such as robot climbing [6], industrial gripping systems [67], and automobile tires where controllable adhesion, reusability, durability and long lifetime are desired properties. In typical solids, contact forces decrease at the onset of sliding, and continue to decrease as the interfacial velocity increases and there is a loss in interfacial contact due partly to wear [13]. For a gecko using traditional adhesives, this would have severe consequences, as any slip while climbing would result in a fall. However, studies have shown that this is not the case, and in fact contact forces *increase* with sliding velocity [49]. Gravish *et al.* discovered that gecko arrays subjected to 30,000 cycles did not show any signs of wear or a reduction in adhesive forces. The surprising result may explain how the gecko is able to travel through its environment and maintain adhesion between its two month long molting cycles.

The principles behind this wearless dynamic friction have been explained by Gravish *et al.* through a model involving nanoscopic stick slip events [49]. In the model, contacting elements are either statically attached to the surface, or in the process of breaking contact and slipping to a new contact position. These uncorrelated stick slip events give rise to the adhesion witnessed during sliding, and increase to a peak velocity before falling off. Their results were confirmed at the macroscale through testing of a soft polymer GSA, which exhibited the stick-slip behavior. This stick slip behavior is critical in preserving the robustness of the adhesive structures. If the structures are subjected to sliding, wear will occur.

GSAs with intended uses in high cycle environments must therefore be designed and evaluated with this in mind. Several investigators have attempted to quantify the wear or long lifetime properties of GSAs [99, 41, 15, 79]. Although potential failure mechanisms have been described, and there is potential for combined modes of failure such as creep deformation and adhesive wear, there is still a need for close examination of the wear modes in GSAs, and design principles that will promote wear-free contact than can enable high cycle uses.

### 1.3.4 Testing Methodology

Due to the coupling of normal and tangential adhesive forces exhibited in the gecko adhesive system, it is important that any testing methodology selected is able to capture this interplay by allowing measurement in more than a single axis. In the past several years, the load-drag-pull (LDP) testing methodology has emerged as a repeatable methodology that is useful for

both natural and synthetic systems [6]. LDP testing involves moving the sample through a displacement controlled path which brings the sample into contact with a counter-surface, while reaction forces are measured in each axis. Due to the controllability and repeatability of this displacement controlled methodology, and its adoption by many other GSA investigators, the LDP test was used throughout this body of work. However, important considerations must be taken when interpreting the results of the LDP test. Due to the displacement controlled nature of the LDP test, it is not directly relevant to map the results to systems and applications that have different boundary conditions. For example, in the case of a robot climbing a wall, the path of the robot body is dictated by the forces acting on the system, and it can be considered a force controlled system. In a force controlled system, a load will be applied to the adhesive, and if this load does not exceed the adhesive limit, contact will be maintained. This is in contrast to the displacement controlled LDP system, where the adhesive will be driven past this failure point, but the path will still be followed, allowing the adhesive to possibly re-engage. We therefore generally report either the maximum adhesive forces during an LDP trial, or the mean forces during the drag phase of a trial, since this could approximately be considered the adhesion limits of the system that one might expect during applications with different boundary conditions.

## 1.4 Contributions

This work builds upon previous accomplishments in the fields of natural and synthetic adhesion. Specific contributions are summarized in the list below:

- *Natural Gecko adhesion on macroscopically rough surfaces (Chapter 2)*: A study of the capability of the *gecko gekko* to adhere to macroscopically rough surfaces was carried out to give insight into the function of the intermediate structures of the foot: the toes and lamellae. The discovery that the toes are capable of adhering to surfaces with amplitudes much larger than their dimensions even without engaging claws, maintaining 60% of shear adhesion on surfaces with amplitudes of 3 mm, and that adhesion can be predicted by the ratio of the lamella dimensions to surface feature dimensions.
- *A new soft polymer GSA (Chapter 3)*: A new type of synthetic GSA has been developed from a soft polymer. This newly developed GSA, consisting of 100-300 micron high ridges, is made with a wax mold cutting process. Testing revealed that the GSA is capable of tensile adhesion of 1.5 kPa while holding 5.5 kPa in shear on smooth glass. In addition, the new GSA is also able to adhere to a variety of rough surfaces including metal, wood, painted walls, acrylic and white marker board.
- *A comparison of hard and soft GSA dry self-cleaning properties (Chapter 3)*: Testing of dry self-cleaning was carried out across a wide variety of particle sizes on the new GSA described above. Experiments were directed towards characterizing the capabilities of

the soft polymer GSA to self-clean, as well as comparing the self-cleaning capabilities with hard thermoplastic GSAs, finding that a GSA made from a hard thermoplastic with nanoscopic fibers was able to recover 96 to 115% of its shear adhesion after fouling with small and large but not medium particles, while a GSA made from a soft polymer and microscopic fibers recovered 40 to 55% on medium and large particles, with SEM imaging revealing particles embedding within the polymer.

- *A magnetically actuated GSA (Chapter 3)*: The development of a new MR elastomer fibrillar adhesive based on the wax cutting technology above, showing that particle capture and control of sub millimeter glass spheres is possible by activation of an external magnetic field which is used to alter the fiber geometry.
- *Wear properties of hard polymer GSAs (Chapter 4)*: Further testing of a hard thermoplastic GSA made from either polypropylene or polyethylene has revealed that long lifetimes are possible. The GSA was tested up to 10,000 cycles on glass, with only a 54% decrease in shear adhesion. We also discovered that it is possible to form spatula like tips on the end of the fibers through a shear deformation process. Spatulae may be partially responsible for the long lifetime of the GSA, and may represent a new pathway to forming nanoscale structures on the tip of the hard thermoplastic fibers.

# Chapter 2

## Adhesion to rough surfaces

### 2.1 Adaptability of gecko gekko adhesive system to macroscopically rough surfaces

The gecko's exceptional climbing ability has been attributed primarily to the fibrillar structures found on the toe pads [127, 8, 14, 9]. As described in Section 1.1, toe pads are in-folded to form rows which hold modified keratinized scales called lamellae. These lamellae are composed of hundreds of tiny hairs called setae, which are then further subdivided into hundreds of nanoscale sized spatulae [112, 113]. This hierarchical system, along with claws [18, 142] that are used for mechanical interlock, allow the gecko to attach to a wide variety of surfaces ranging from smooth glass and plants to the roughest tree bark.

Although the majority of research on the gecko adhesive system has focused on the nanoscale features, the lamellae, the tendons, blood vessels and muscles of the foot are known to play an important role [111, 100, 128]. Russell [112, 113] proposed that the intermediate structures are used to cushion the foot against the surface, and to allow the flexible lamellae to conform more closely to the surface to which they are adhering. Another theory on the function of the intermediate structures is that the size, shape and angle of the larger hierarchical structures aid in rapid detachment of the foot [24, 38]. Other investigators have also shown analytically that the hierarchical structures uniformly distribute the adhesive force across the attachment pads, resulting in stronger and more robust adhesion on rough surfaces [23, 77]. Investigators have also identified a range of surface roughness that is too rough for the setae alone to adhere to, but is also too smooth for the claws to form a mechanical interlock on, indicating that the intermediate sized structures may be critical in allowing the hierarchical system to adhere across a wide range of length scales [14, 130]. Vanhooydonck *et al.* found that the acceleration of the geckos, and thus the effective force they were able to produce, decreased when running vertically on mesh and cloth as compared to fine-grained wood, although the final running speed was the same [130]. However, this study was not conclusive because 1) acceleration of the center of mass is not limited by peak

adhesive force of the foot for these surfaces. There is no reason to expect peak single leg forces to approach even the static adhesive or shear capacity unless the number of attached spatulae could be reduced by 1 to 2 orders of magnitude. 2) Peak body accelerations estimated by twice differentiating position digitized from a 250fps video do not provide a good estimate of the instantaneous forces acting at the interface between setae and substrate. A recent study by Russell and Johnson compared surface topology on a wide range of irregular surfaces including sandstone, glass, acetate, sandpaper, cinderblock and oak, focusing primarily on the available contact area of each surface [116, 70], and later found that deployment of the gecko adhesion system is based on the surface incline, and not on roughness [115]. These studies indicate that the gecko is able to adhere to rough surfaces at some reduced level of adhesion. However it is still unclear how adhesion to rough surfaces is accomplished, and to what degree surfaces of varying roughness compromise total foot clinging ability. Furthermore, the randomly rough nature of the surfaces used in studies thus far limits the ability to compare models of lamellar contact mechanics, as well as data from other studies and among diverse species.

We attempt to better understand toes and lamellar function by measuring how geckos adhere to surface features that are too rough for the setae alone to adhere to, but are too smooth for the claws to form a mechanical interlock [14, 130], and to identify any possible limitations of the hierarchical structure, as it is known analytically that roughness will dramatically decrease adhesion between smooth surfaces [101, 126]. We studied whole-foot gecko adhesion on extruded sinusoidal patterns of varying amplitudes and wavelengths similar to the dimensions of the lamella and toe structures. By observing the maximum shear force a gecko foot can attain on a variety of controlled surfaces, we propose to quantify these macroscopic structures' role in shear adhesion. We hypothesize that surface amplitudes greater than lamellae depth will cause a decrease in shear adhesive force and that increasing surface wavelength will increase shear adhesion.

Our data will be useful for validation of models attempting to explain contact mechanics of the lamellar structures due to the computable nature of the sinusoidal surfaces used to test shear adhesion. As well, this information can be used to explain how evolutionary forces shaped lamellar traits by allowing a more rigorous comparison between surface features found in the species environment and the dimensions and fidelity of the toe structures found on various lizard's feet. Insights from this study can provide biological inspiration for the design of hierarchical synthetic adhesives and further improve their adhesive capability on rough surfaces.

### 2.1.1 Shear adhesion observations of gecko gekko feet on macroscopically rough surfaces

#### Species selection

Live Tokay geckos (*Gecko gekko*) ( $106 \pm 13$  g ( mean  $\pm$  s.d.) N=4) were used for our experiments because: 1) they have been used extensively in adhesion research, and protocols are well established, 2) the fabrication process for the engineered rough surfaces made possible surface features that are similar in size to the intermediate structures of the Tokay gecko foot and 3) the Tokay gecko has one of the most well developed lamellar structures of the lizards that exhibit dry adhesion.

#### Gecko lamellae dimensions

Dimensions of the lamellae were determined by taking photographs with a camera mounted on a microscope, and measuring structures using image analysis software (ImageJ, NIH, Bethesda, MD). The lamellar wavelength was defined to be the average distance between lamellae, and the lamellar amplitude was defined as the average proximal to distal length directed along the length of the lamella as indicated in figure 2.1. Lamella had an average amplitude of  $0.87 \pm 0.13$  mm (mean  $\pm$  s.d. N=10) and wavelength of  $0.7 \pm 0.16$  mm (mean  $\pm$  s.d. N=10).

#### Engineered surface fabrication

We used computer aided design software (SolidWorks, Dassault Systems, Lowell, MA) to create designs of sinusoidal surfaces with various combinations of amplitudes (A) and wavelengths (T, Fig. 2.2) . We made these designs into wax molds using a 3D printer (Thermojet, 3D Systems, Rock Hill, SC). Polyurethane (PU) was cast into the wax molds and de-molded once cured. Each PU surface was 50 mm long by 50 mm wide. Sinusoidal surfaces were selected because they are easy to characterize and because the rounded edges prevented claw engagement which would interfere with the surface-lamellar interaction. Amplitudes and wavelengths were chosen to be the same order of magnitude as the lamellae to toe dimensions, with 35 surfaces being created in total with amplitudes of  $0.5\text{-}3$  mm  $\pm$  0.08 mm and wavelengths of  $0.5$  mm to  $6$  mm  $\pm$  0.08 mm. The flat control surfaces were made of PU, cast into molds made in the same 3D printer as the sinusoidal surfaces to minimize differences in microscale roughness.

#### Experimental apparatus and testing methodology

We mounted the sinusoidal surfaces on a 6-axis force transducer (Nano-17, ATI-IA, Apex, NC), which were then attached vertically to the edge of a rigid table. Data acquisition software (MATLAB , Mathworks, Natick, MA) was used to collect and analyze the forces in



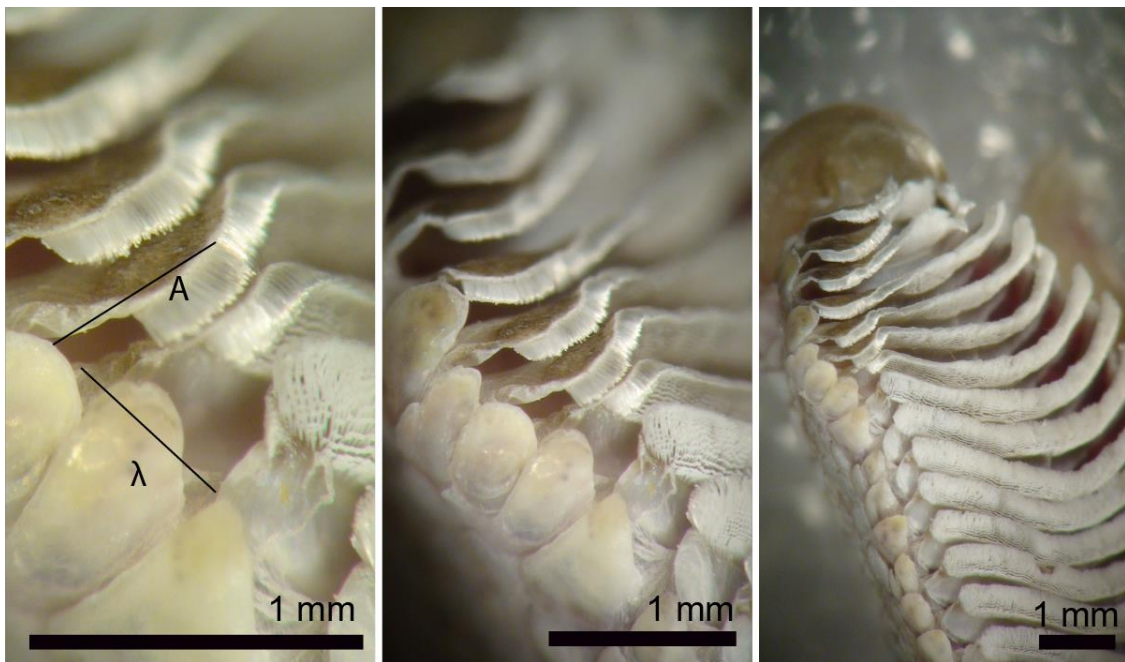


Figure 2.1: Lamellae observed on the toe of a live Tokay gecko (*Gecko gekko*), showing example measurements of the lamellar wavelength and amplitude.

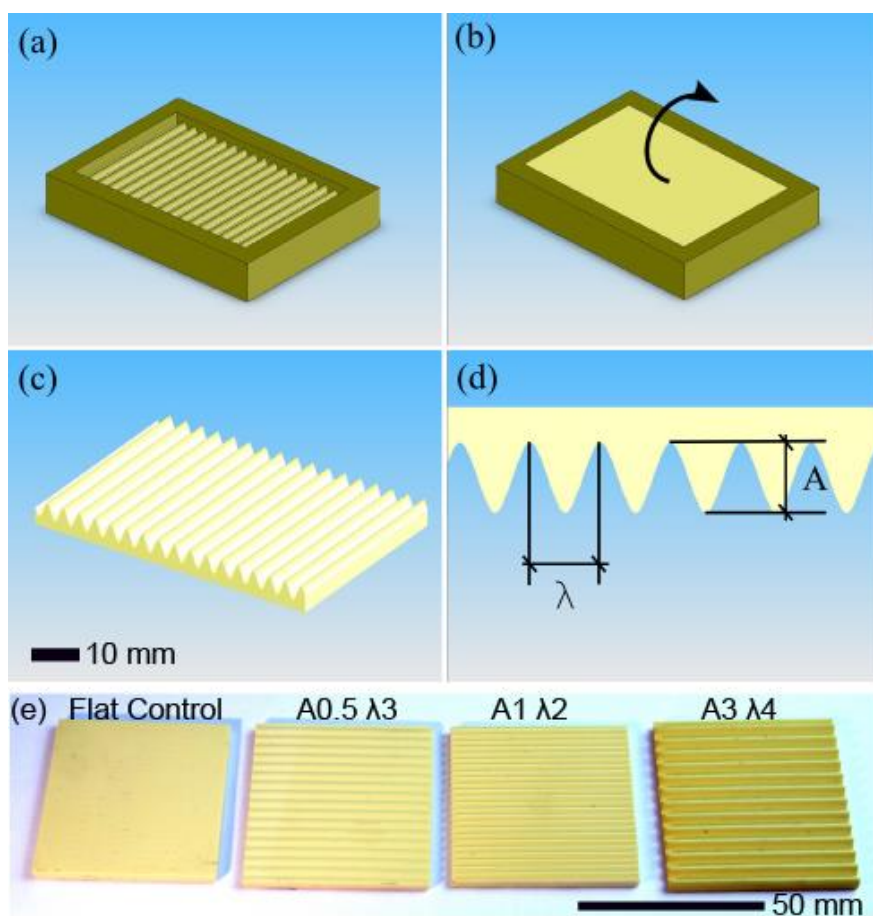


Figure 2.2: Creation of the surfaces. (A) A 3D wax mold was printed. (B) Polyurethane (PU) was then cast into the mold and allowed to cure. (C) The PU surface was then removed from the mold. (D) Cross section of the surface showing amplitude  $A$  and wavelength  $\lambda$ . (E) The flat PU control surface as well as three example surfaces used in the various conditions.

the x, y, and z-axes. Additionally, a side view video camera was set up to record the behavior of gecko feet, toes, lamella, and claws. Simulated steps were performed by manually moving a gecko foot in a load-drag-pull path that allows measurement of the peak engagement forces (Fig. 2.3). Tokay geckos were held vertically, with their head up, and a back foot was used to engage the bottom of the sinusoidal surface. A pre-load normal force of approximately 1.2 N was applied to the entire gecko foot for approximately 1 second by pressing with a gloved hand, and then released. When the normal force returned to 0 N, the gecko was dragged upwards vertically along the surface at a steady speed of 2 to 5  $mm/s^{-1}$ , being careful not to apply additional normal or lateral forces. Gravish *et al.* [49] have determined this to be a reasonable drag velocity range, because 1  $mm/s$  is the transition velocity above which there is a power law increase in force. Following this power law, we calculated that we should expect to see less than a 1% difference in measured adhesion due to velocity effects across the range of allowable velocities. Small errors in velocity in our range should not have a large effect on measured forces. As the foot approached the upper edge of the surface, we pulled the foot off in the normal direction.

### **Trial selection criteria**

Before and after each trial, we tested the gecko on the flat PU control surface to ensure the gecko was adhering consistently. If geckos could not attain a benchmark force of 9 N on the control surface before and after the surface trial, we discarded the trial. Trials were also excluded if any claw engagement, foot disengagement, significant lateral or normal forces above 1 N, or if dragging speeds were out of our set range, as calculated by measuring the time of the drag phase across a set distance with a stopwatch. As well, individuals were not used during periods when their setae were molting. Two hundred and twenty four trials yielded acceptable data across four individuals. We attempted to have each animal serve as its own control by testing the same rear foot of each gecko on all surfaces at least twice. However, due to variations in animal behavior and the criterion used to accept or reject trials not every gecko is represented equally in every condition. The vast majority of conditions (30/35) had at least 6 acceptable trials from at least two geckos across the range of conditions. Our data set represents an attempt to balance the challenge of collecting data from live animals with gathering sufficient data across the large number of conditions.

The shear force for each trial was taken as the maximum generated during the steady-state drag period, as seen in Fig. 2.4. We used maximum shear force values for each surface to determine the change in maximum performance between the control surface and the sinusoidal, engineered surfaces.

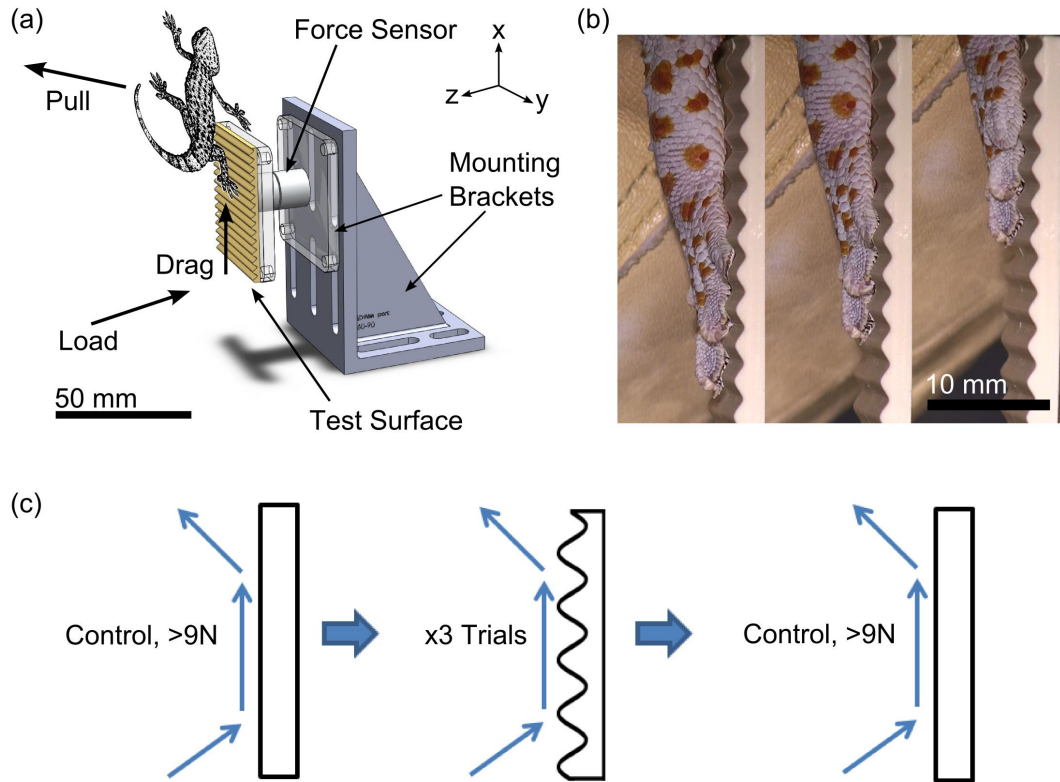


Figure 2.3: (A) The experimental apparatus showing how the simulated steps were performed with the Tokay geckos. (B) A sequence of stills taken from video of a foot drag on a surface with amplitude 3 mm and wavelength 5 mm. (c) the testing methodology in which the rear foot is testing on the PU flat control surface, then 3 trials are performed on the condition being tested, and finally, the foot is again tested on the flat PU control surface afterwards.

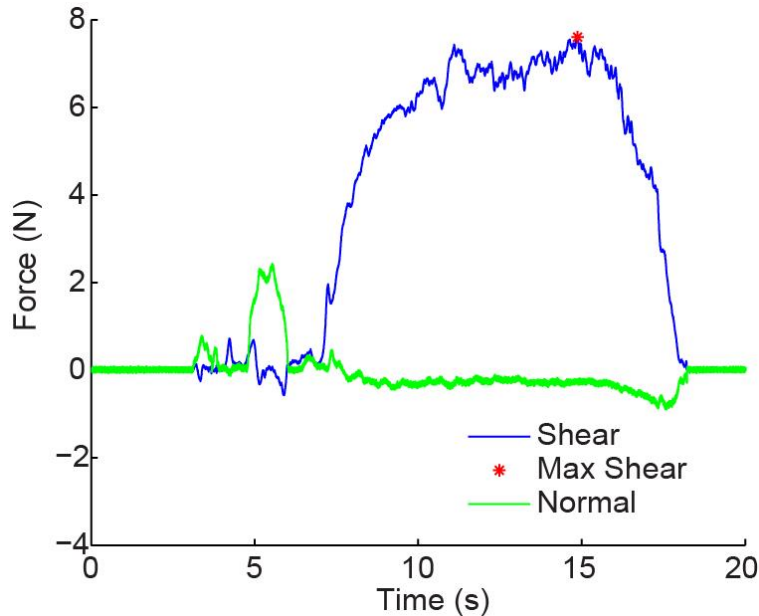


Figure 2.4: Shear (blue line) and normal (green line) adhesion data from a single load-drag-pull step of a Tokay gecko on a sinusoidal surface with an amplitude of 2 mm and a wavelength of 3 mm.

## 2.1.2 Observations of lamellar conformation and adhesion

### Shear adhesive force as a function of time

As we loaded the gecko's foot, normal force increased to our target preload of 1-2 N (Fig. 2.4). After dragging, shear adhesive force increased rapidly to a steady-state, while normal force remained near zero (Fig. 2.4). Shear adhesive force steady-state was maintained for more than 5 s allowing estimation of the maximum value for the given trial. The force traces were not filtered. Data were collected at 1000 Hz. Maximum shear adhesive forces ranged from 0.21 to 14 N.

### Effect of surface amplitude and wavelength

To determine the effect of surface features, we plotted the percent relative maximum shear in relation to a flat PU control surface as a function of the surface wavelength and amplitude (Fig. 2.5). Multi-Factor ANOVA results showed no significant effect of individual ( $P=0.06$ ). As amplitude increased, maximum shear adhesion decreased significantly for each wavelength tested (ANOVA,  $F(4,213) = 74.3$ ;  $P < 0.001$ ; Fig. 2.5A, B). As wavelength increased, maximum shear adhesion increased significantly at each amplitude tested (ANOVA,  $F(6,213) = 88.6$ ;  $P < 0.001$ ; Fig. 2.5C, D). The condition with surface amplitude of 1 mm and wavelength

of 6 mm showed no significant difference in adhesion from a flat control surface made from the same material (One sample T-Test,  $P=0.076$ ). Video evidence shows that the surface feature dimensions that caused this decrease in adhesion correspond approximately to the dimensions of the gecko toe and lamella features.

### **Conformation of toes and lamella to engineered rough surface**

Video footage of trials revealed a wide range of toe and lamella conforming behavior, from the entire toe and lamella contacting sinusoids, to lamella and toes not conforming at all to the surface (Fig. 2.6). At wavelengths below the lamella dimensions (Fig. 2.6A, B), the toes and lamella were not conforming to the surface and instead are only resting on the peaks of the engineered surface. It is on these surfaces that we measured the most significant reduction in shear adhesion. The intermediate surface dimensions (Fig. 2.6C, D) approximately correspond to the point at which lamella can slightly conform, but the toes cannot, reducing the number of contacting lamella. Toes are seen slightly curling around the surface features, but not enough to bring all the lamella into contact. We observed lamella extending from the bottom of the toes, but not being long enough to reach the deepest parts of the surface. At the largest surface dimensions (Fig. 2.6E, F), the lamella and toes conform to the surface, and they appear to make complete contact. There is no significant loss in adhesion on these surfaces from a flat control surface of the same material (surface:  $A=1$ ,  $T=6$ , One sample T-Test,  $P=0.076$ ).

### **2.1.3 Discussion**

The interactions between the gecko lamella and surface features that allow the gecko to adhere with such large forces remain a complex phenomenon. Previous studies of whole body forces have given some indication of how roughness may decrease adhesive forces, but the randomly rough nature of these surfaces and lack of data have made making conclusions about toe and lamellar contact mechanics difficult [70, 130]. The systematic approach taken by this study is the first to shed light on how varying both surface amplitude and wavelength effect adhesion at the whole foot level. Specifically, the data suggests that the ratio of lamella to surface feature size plays a large role in whole foot clinging ability as indicated by both force measurements, and video data which show lamellar features interdigitating to various levels depending on the amplitude and wavelength of the surface as shown in Figure 2.7.

Russell and Johnson (2013) [117], suggested that setae or lamella features would be able to make contact with the uppermost portion of the surface corresponding to the length of the lamella. They go on to predict that this potential area of available contact could be used to predict adhesive forces. However, our data show that just using the available area of contact only poorly predicts adhesive forces. Figure 7 shows the measured shear adhesive force as a function of the projected area available for contact for the top 0.87 mm of the conditions tested (as this depth is the measured lamella length for the Gecko gekko individuals we

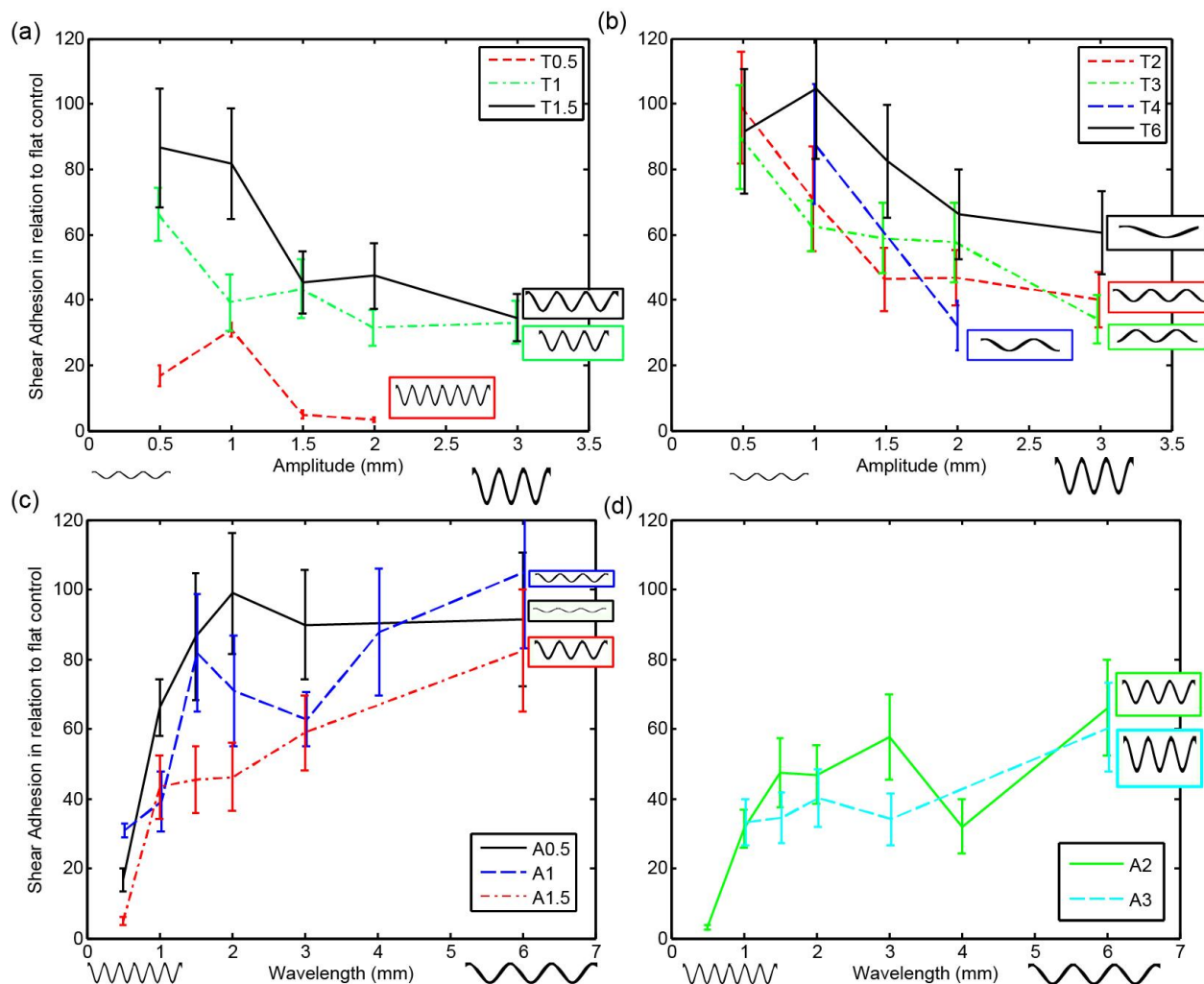


Figure 2.5: Percent shear adhesion across surfaces that vary in amplitude (A) and wavelength (T) relative to a flat control surface. (a,b) Percent shear adhesion as a function of amplitude with wavelength held constant across low (a) and high (b) wavelengths shown in inset. (c, d) Percent shear adhesion as a function of wavelength with amplitude held constant across low (c) and high (d) amplitudes shown in inset. Adhesion decreased significantly with increasing amplitudes and decreasing wavelengths (ANOVA  $P < 0.001$ ; error bars represent one standard error.).

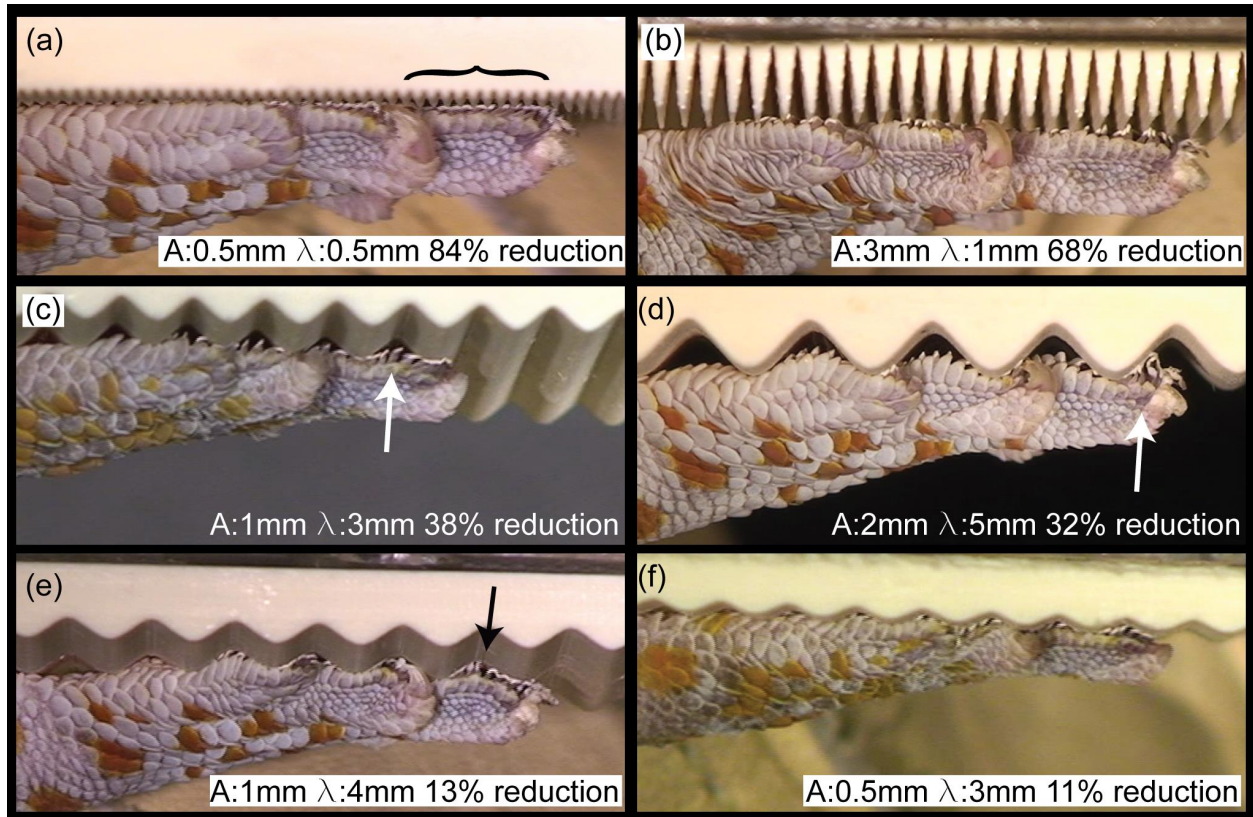


Figure 2.6: Photos taken from video of load-drag-pull trials on several, engineered rough surfaces. At wavelengths below the lamella dimensions (a, b) the roughness is too large for the toes and lamella to conform (black bracket showing lamellae only contacting tips of ridges). The intermediate surface dimensions (c, d) approximately correspond to the point at which a significant loss in adhesion is measured, where lamella can slightly conform, but the toes cannot (white arrows). At larger surface dimensions (e, f), the lamella and toes can conform to the surface, and there is no significant loss in shear adhesion (black arrow).



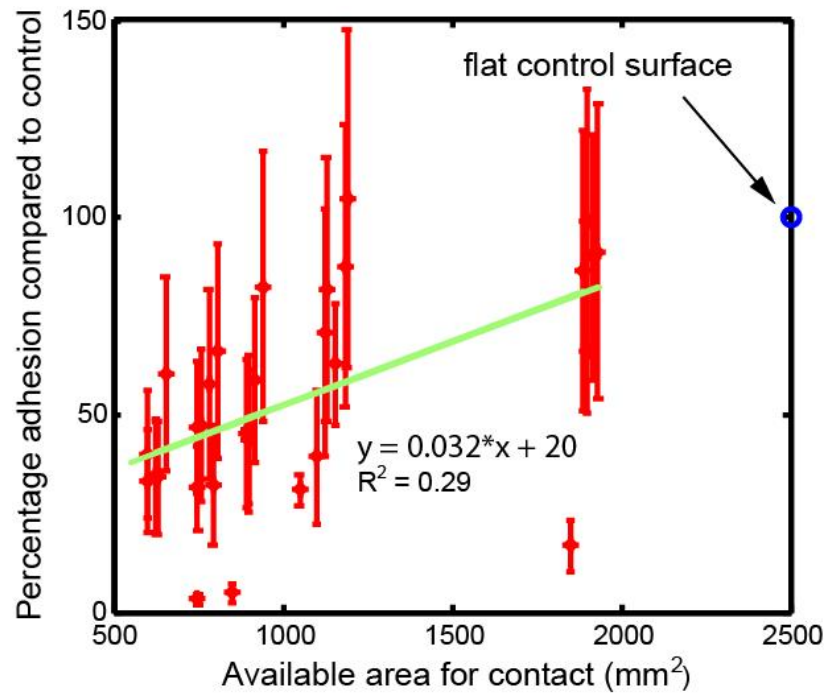


Figure 2.7: Percent reduction in maximum shear force from a flat control surface vs available area for contact in the top 0.87 mm of the sinusoidal surface. Russell and Johnson [117] suggested that increased available area for contact may predict an increase in adhesion, however we found this was not significant ( $r^2 = 0.29$ ) showing that a more complex metric is needed to predict surface adhesive forces (error bars are 95% confidence intervals).

used in this study). As can be seen, no clear trend exists between the available area for contact and the shear adhesion. The data suggest the available area of contact is a weak predictor of shear adhesive capabilities ( $r^2 = 0.29$ ), and as Russell and Johnson contend, more exploration is needed surrounding the relationship between toe-pad geometry, surface features and adhesive capability across a wider variety of species.

It may be that beyond certain amplitudes and below certain wavelengths the lamella can no longer adapt to the surface, and adhesion is lost due to geometric constraints (e.g. the lamella cannot fit between the surface features to make contact with the surface). Interestingly, Huber *et al.* [60] reported that for spatular attachment, a roughness on the same size scale as the feature size created a decrease in the adhesive force. This is strikingly similar to the trend we have found at the lamellar size scale, and may suggest that the smaller size scale structures are behaving similarly to the larger size scale structures, and again supports the hypothesis that it is the relationship between the anatomical feature size and the surface feature size that best predicts adhesive capability .

It is also possible that the local angle of the surface features determines clinging ability, and this has been demonstrated at the setal size scale [8]. During contact, the lamella can be seen bending to an angle in order to conform to the surface, and this angle may be determined by the ratio of lamella to surface feature size. However, further modeling would be required to conclusively say how local lamellar angle effects whole foot adhesion. It is our hope that data from this study could be used to verify such a model.

The significant drop in adhesive forces on surfaces with higher amplitude and shorter wavelengths suggest that the lamellae and toe structures have evolved to conform to only a certain range of rough surfaces. There has been some speculation that there may be a positive relationship between lamellae number and clinging ability [65], however our data suggests that clinging ability on rough surfaces may also be linked to lamellae dimensions. It is still difficult to make these conclusions since data from other species does not yet exist. These results do indicate that surface roughness plays an important role in explaining the disproportionately high safety factor of the gecko adhesive system, which is in some cases stated to be several-hundred fold [7]. This was pointed to by Vanhooydonck, but lack of strong data prevented a stronger conclusion [130]. Our data may be used to explain how evolutionary forces shaped lamellar traits by allowing a more rigorous comparison between surface features found in the species natural environment and the dimensions and fidelity of the toe structures found on various lizards feet. More data will need to be collected from a wider variety of species as well as characterization of substrates found in the natural environment to allow further conclusions.

These results also hold strong implications for the design of synthetic gecko adhesives; a new controllable adhesive inspired by the gecko. Current synthetic gecko-inspired adhesives incorporate only micro and nano structures that adhere ideally to smooth surfaces, but few synthetic adhesives have incorporated macroscale structures similar to those found on gecko feet that would allow for adhesion on macroscopically rough surfaces. In one case, Lee *et al* fabricated nanofiber arrays on lamellae-analogues from a hard polymer and demonstrated

that adhesion on non-planar surfaces were five times greater than arrays without lamellar support structures [83]. Our results suggest that adhesion to rough surfaces of these gecko inspired adhesives may be improved if the relative size between the adhesive geometry and surface geometry is carefully considered. Further understanding of the mechanisms of adhesion on a macroscale level may enable adhesion on nonplanar surfaces; one of the ultimate engineering goals required for wide-scale application of synthetic gecko-inspired adhesives.

## 2.2 Concluding remarks

The role in adhesion of the toes and lamellae - intermediate sized structures - found on the gecko foot remains unclear. Insight into the function of these structures can lead to a more general understanding of the hierarchical nature of the gecko adhesive system, but in particular how environmental topology may relate to gecko foot morphology. We sought to discern the mechanics of the toes and lamellae by examining gecko adhesion on controlled, macroscopically rough surfaces. We used live Tokay geckos, (*Gekko gecko*), to observe the maximum shear force a gecko foot can attain on an engineered substrate constructed with sinusoidal patterns of varying amplitudes and wavelengths in sizes similar to the dimensions of the toes and lamellae structures (0.5 to 6 mm). We found shear adhesion was significantly decreased on surfaces that had amplitudes and wavelengths approaching the lamella length and inter-lamella spacing, losing 95% of shear adhesion over the range tested. We discovered that the toes are capable of adhering to surfaces with amplitudes much larger than their dimensions even without engaging claws, maintaining 60% of shear adhesion on surfaces with amplitudes of 3 mm. Gecko adhesion can be predicted by the ratio of the lamella dimensions to surface feature dimensions. In addition to setae, remarkable macroscopic-scale features of gecko toes and lamellae that include compliance and passive conformation are necessary to maintain contact, and consequently, generate shear adhesion on macroscopically rough surfaces. Findings on the larger scale structures in the hierarchy of gecko foot function could provide the biological inspiration to drive the design of more effective and versatile synthetic fibrillar adhesives.

# Chapter 3

## Fouling of fibrillar surfaces

### 3.1 Dry self-cleaning properties of hard and soft fiber structures

Particle capture and release is a significant problem in many industries such as in semiconductor manufacturing, solar panel cleaning and reusable adhesives for robot locomotion in complex and dirty environments [55]. Current methods of particle manipulation or control are insufficient for these applications where liquid solutions cannot be used [129, 144], vibration or air jets are ineffective due to high surface area to volume ratios [98], scrubbing is not an option due to delicate surfaces, geometric or environmental constraints [19, 137], and electrostatics [32] or other methods [52, 133, 33] are not sufficient.

Traditional pressure sensitive adhesives (PSA) are made using soft viscoelastic polymers (Young's modulus  $\leq 100$  kPa at 1 Hz [26, 104]) that conform to a surface to achieve high adhesion. However, these soft polymers tend to foul quickly, and lose their ability to adhere to a surface after several uses.

In contrast to traditional soft-polymer pressure sensitive adhesives, Hansen and Autumn have revealed that gecko hairs can shed dirt particles during use, keeping the adhesive pads clean enough to allow the gecko to continue climbing [53]. This dry self-cleaning is explained by a change in the conformation of the nanofibrillar surfaces through passive mechanical action. The authors used contact models to explain that self-cleaning occurs by an energetic disequilibrium between the adhesive forces attracting a dirt particle to the substrate and those attracting the same particle to one or more spatulae. Specifically, they describe the interaction energy between a spherical dirt particle of radius  $R_p$  and a substrate by Equation 3.1 [53]:

$$W_{pw} = \frac{-A_{pw}R_p}{6D_{pw}} \quad (3.1)$$

where  $p$  and  $w$  refer to particle and substrate,  $A$  is the Hamaker constant ( $\approx 10^{19}$  J for

van der Waals interactions in air), and  $D$  is the particle-to-substrate gap [53]. Similarly, the spatula-particle interaction can be characterized for a spatula approximated by a portion of a sphere of radius  $R_s$  by Equation 3.2:

$$W_{ps} = \frac{-A_{ps}R_pR_s}{6D_{ps}(R_p + R_s)} \quad (3.2)$$

Taking the ratio of these interaction energies, and equating it to  $N$ , the number of spatula in contact with a particle, gives the equilibrium point when the adhesive energies are in balance:

$$N = \frac{W_{pw}}{W_{ps}} = \left(1 + \frac{R_p}{R_s}\right) \frac{A_{pw}D_{ps}}{A_{ps}D_{pw}} \quad (3.3)$$

Considering the Hamaker constants and the gaps to be the same for each interaction, an approximate trend can be determined for the self cleaning behavior, dependent on the particle and spatula size. Figure 3.1 shows the maximum number of spatula that can be adhered before dry self-cleaning will not occur. The trend shows that for larger particle sizes and smaller spatula geometries, self cleaning is more likely. For geometries similar to a gecko spatula, they estimate that 26 or more spatula would need to adhere to a  $2.5 \mu\text{m}$  particle in order for self-cleaning of the particle to not occur; a case that is geometrically impossible.

It has also been theorized that geckos shed particles from their feet through a unique dynamic self-cleaning mechanism via digital hyperextension. Hu *et al.* [59] have described a model in which dry-self cleaning can be explained by inertial forces of particles overcoming adhesive forces during digital hyperextension of the foot. Their results indicate that digital hyperextension of the arrays can give a two-fold increase in recovery.

Whether the source of dry self cleaning is caused by static disequilibrium or a dynamic effect, it has only been previously reported in natural gecko hairs and in the polypropylene gecko-inspired synthetic adhesives previously developed in the Fearing lab [84]. Arrays of the stiff polypropylene fibers were contaminated with gold particles  $1.5 \mu\text{m}$  and  $2 \mu\text{m}$  in diameter before simulated steps were performed by attempting to adhere them to a vertical glass slide while suspending an increasing amount of weight from the samples. In contrast to PSA samples which recovered zero of their initial adhesive strengths, the PP fibers recovered 33% of their shear force. It was also noted that about 60% of the particles were transferred onto the glass slide, and that arrays of PP fibers were unable to recover from larger  $3\text{-}5 \mu\text{m}$  particles. Using a similar contact mechanical model from Hansen and Autumn [53], Lee calculated that particles larger than  $5.2 \mu\text{m}$  would not self clean [84].

This apparent ability to dry self-clean in dry environments is in contrast to the lotus effect, which requires droplets of water to shed particles from the highly hydrophobic non-adhesive surface [11]. Several synthetic gecko adhesives have shown this 'lotus' or wet self-cleaning effect. Notably, Tsai *et al.* [129] fabricated a GSA made from e-beam photoresist and carbon nanotubes (CNT), and showed that although these materials are hydrophilic,

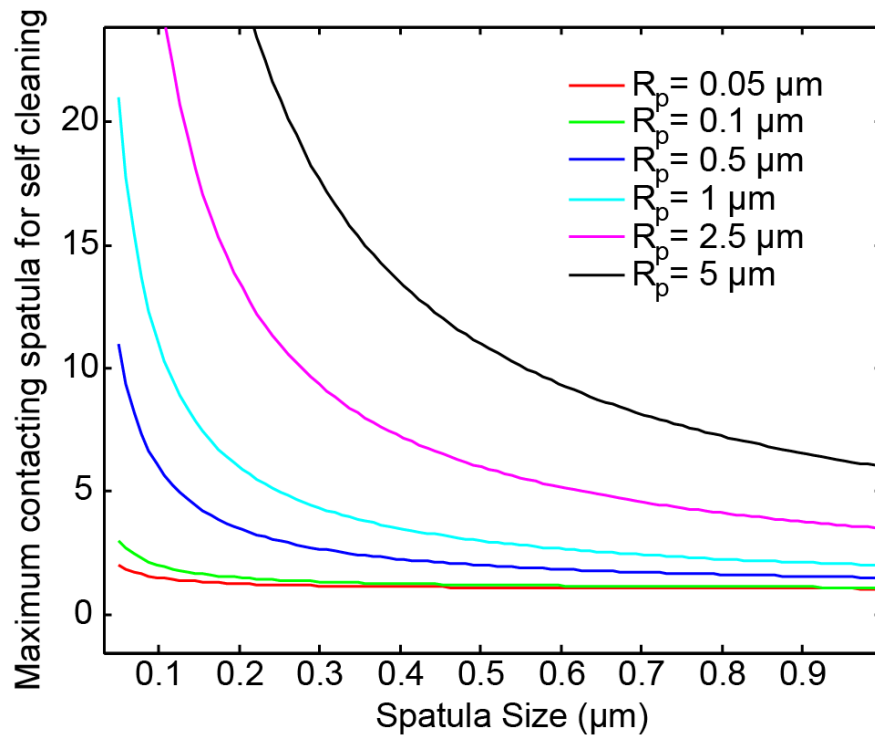


Figure 3.1: A contact analysis outlined by Hansen and Autumn [53] reveals that with larger particle sizes and smaller spatula geometries, self cleaning is more likely.

they exhibit superhydrophobic behavior due to the surface geometry. A contact angle of  $157^\circ$  was achieved. As well, Kim, Cheung and Sitti [75] created a polyurethane mushroom shaped microfiber array that exhibited superhydrophobic behavior, which was attributed to the mushroom shaped tips. Further experimentation revealed that water droplets passed over an array fouled with silica contaminants were able to clean the array to nearly its original state.

With the rapid advancement of many types of GSAs under way, it will be advantageous to understand the impact that the design parameters have on the dry self-cleaning effect discussed above. To date, no work has been done to directly compare what effect material choice or fiber diameter have on the dry self-cleaning property. Therefore, a comparison of the dry self-cleaning capabilities of two example types of GSAs fabricated with different materials and dimensions was carried out; one made from a hard thermoplastic polymer (Young's modulus  $\approx 1$  GPa) with fiber diameters  $\approx 600$  nm and the other made from a soft elastomer (Young's modulus  $\leq 10$  MPa) with fiber diameters  $\approx 25$   $\mu\text{m}$ . Each type was subjected to a standard testing protocol across various particle sizes, which was used to quantify the cleaning effect through the establishment of an empirical recovery ratio.

An analysis of the contact strength between fibers, particles and substrates of various dimensions and elasticity was also carried out to explain the experimental findings and generalize the results. The Hansen and Autumn model cited above only accounts for forces normal to the interacting surfaces, and applies to the cases where surfaces are separated normally. However, the vast majority of use cases for the GSA (and the experimental setup used to test the adhesive properties of the array) involve shearing between the counter surfaces which give rise to shearing or static friction forces between the array, particles and the substrate. Therefore, the analysis below extends the self-cleaning predictions to cases involving shearing of the surfaces, and a fiber in side contact with the contaminating particle, as shown by Puthoff *et al.* [43].

### 3.1.1 Modeling of self-cleaning with shear/static friction

Macroscopic friction forces are independent of the contact area between bodies, as described by Amontons' Law [13]. This is, however, not the case for microscopic, single-asperity contacts. In these cases, the static force required to produce interfacial sliding  $F_f$  is related to the strength of the interfacial bond in shear  $\tau^*$  (a stress) and the contact area  $A$ , given by [22]

$$F_f = \tau^* A, \quad (3.4)$$

Whether or not contacting bodies will slide relative to one another will be determined by the criterion  $\tau \geq \tau^*$ , where  $\tau = F/A$  is the applied shear stress.

In problems with multiple, serial contacts (such as those incorporating a particle lodged between two surfaces) the sliding criterion will be different for each individual contact, since

(i) the parameter  $\tau^*$  depends on the properties of the materials involved and (ii) the applied stresses will vary with differing contact areas  $A$ . The interfacial shear strength of materials #1 and #2 can be estimated from their effective interfacial shear modulus  $G^*$  as [22]

$$\tau^* \approx \frac{G^*}{C} = \frac{1}{C} \left( \frac{2 - \nu_1}{G_1} + \frac{2 - \nu_2}{G_2} \right)^{-1}, \quad (3.5)$$

where  $G_1$ ,  $G_2$ ,  $\nu_1$ , and  $\nu_2$  are the shear moduli and Poisson's ratios of the different materials and  $C \approx 25\text{--}30$  is an empirical factor relating the 'yield stress' of the interface to the shear modulus. The other determining factor in the sliding criterion, the contact area between the bodies, will be in general unknown, although good solutions exist for the contact of spherical bodies under applied normal loading [69, 31]. These contact areas will depend on the contact modulus  $E^* \equiv [(1 - \nu_1^2)/E_1 + (1 - \nu_2^2)/E_2]^{-1}$ , which includes the Young's moduli,  $E_1$  and  $E_2$ , of the different materials.

The three-body contact problem for a contaminated fiber with a particle between itself and a substrate is shown in Figure 3.2. The fiber is pulled with transverse force  $F$  and imparts a normal load  $L$  to the particle. The triplets of elastic constants of the fiber, particle, and surface are, respectively,  $\{E_f, G_f, \nu_f\}$ ,  $\{E_p, G_p, \nu_p\}$ , and  $\{E_s, G_s, \nu_s\}$ . Following Johnson-Kendall-Roberts (JKR) contact mechanics, there is a circular contact region between the particle and the surface with an area of [69]

$$A_{p,s} = \pi \left( \frac{3R_p}{4E_{p,s}^*} \right)^{2/3} \left( L + 3\pi\gamma R_p + \sqrt{6\pi\gamma R_p L + (3\pi\gamma R_p)^2} \right)^{2/3}, \quad (3.6)$$

where  $L$  is the normal load and  $\gamma$  is the work of adhesion. The contact between the cylindrical fiber and the particle is a shape that is difficult to calculate, so here we assume it to be an ellipse whose semimajor axis is aligned with the axis of the fiber [58] and is equal to the JKR radius for the spherical case. If this ellipse has eccentricity  $e$ , then the area  $A_{f,p}$  will be calculated in a similar manner to  $A_{p,s}$  above, but will include an additional factor of  $(1 - e^2)$ .

Using Equations 3.4, 3.5, and 3.6, the sliding criterion can be determined for the particle and the surface at all applied transverse forces  $F$  for fixed  $L = 250$  nN and  $R_p = 500$  nm. We assume a stiff particle ( $E_p = 10$  GPa), a surface of intermediate modulus ( $E_s = 1$  GPa), and that  $\nu_p = \nu_s = \frac{1}{3}$ . The surface energy term  $\gamma$  is fixed at  $0.05$  J/m<sup>2</sup>, typical for van der Waals interactions [66]. Similar calculations apply for the criterion for sliding between the fiber and the particle. We take  $R_f = 1000$  nm, so  $e = 0.859$ . The resulting curves are in Figure 3.3. Sliding occurs at a lower threshold force for the fiber-particle system than for the particle-surface system, i.e. the fiber will self-clean under these conditions.

The analysis above sets the threshold force for sliding at the  $i$ - $j$  interface at  $F_{i,j}^*$ , as determined by the solutions to the curves in Figure 3.3. This is the force of static friction



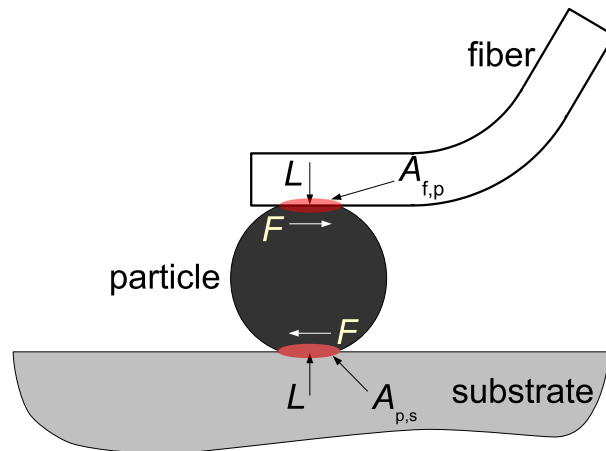


Figure 3.2: Schematic of fiber, contaminant particle, and substrate. The interfacial contact areas  $A_{f,p}$  and  $A_{p,s}$  depends on the materials properties and the normal load  $L$ . These areas and the applied lateral load  $F$  determine the shear stress acting at each interface. Plot contributed by Puthoff, in [43], used with permission.

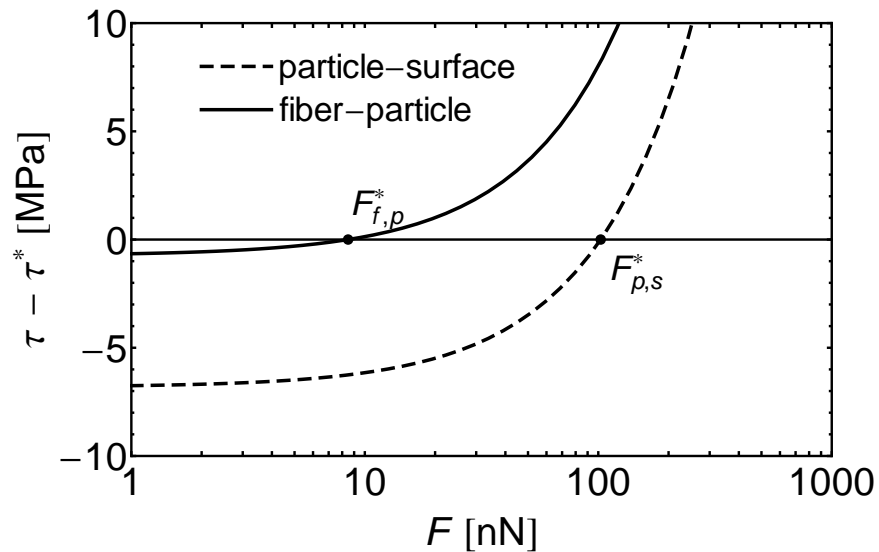


Figure 3.3: Sliding criteria for particle-surface and fiber-particle interfaces. The critical sliding forces for each contact are given by  $F_{f,p}^*$  and  $F_{p,s}^*$ . For the given parameters, sliding threshold forces are smaller for the fiber-particle interface; this produces self-cleaning of the fiber. Plot contributed by Puthoff, in [43], used with permission.

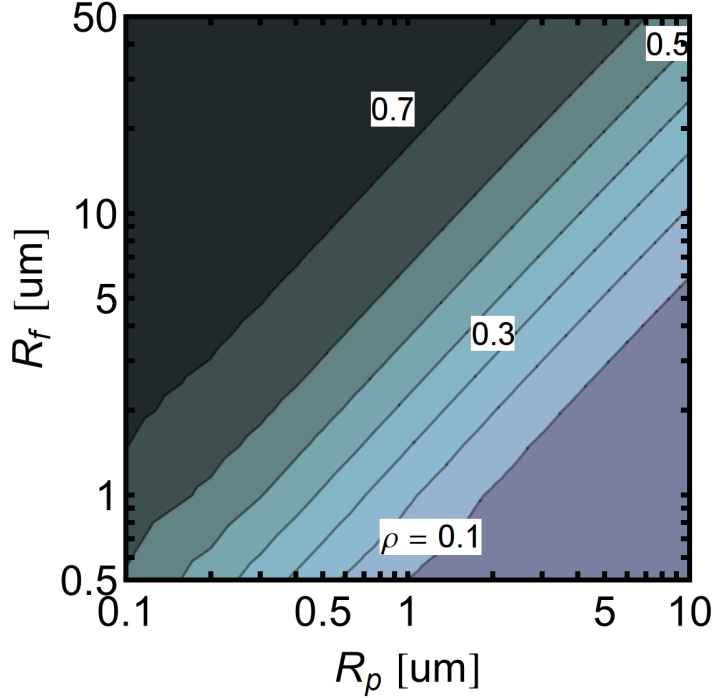


Figure 3.4: The cleaning parameter  $\rho \equiv F_{f,p}^*/F_{p,s}^*$  as determined by both fiber radius  $R_f$  and contaminant particle radius  $R_p$ . Self-cleaning by shear works best for small fibers and/or large particles. Plot contributed by Puthoff, in [43], used with permission.

for the given interface and, in the case of a smooth or stick-slip mechanism, is required for sustained sliding [22]. We can explore how the different variables affect the cleaning properties of a fiber/particle/substrate system by defining a 'cleaning parameter'  $\rho$  as:

$$\rho \equiv \frac{F_{f,p}^*}{F_{p,s}^*}. \quad (3.7)$$

When  $\rho < 1$ , sliding at the fiber-particle interface is favored and self-cleaning will be significant. When  $\rho \approx 1$  or greater, self-cleaning is not expected to occur. Figure 3.4 shows how the cleaning parameter changes with both particle and fiber size. The data in Figure 3.4 indicate strong ( $\rho \leq 0.77$ ) self-cleaning at all the  $R_f$ - $R_p$  combinations illustrated, though we note that, for combinations where  $R_p \gg R_f$ , up to  $n$  fibers may be associated with each contaminant particle. A straightforward modification of Equation 3.7 to read  $\rho \approx \beta \frac{F_{f,p}^*}{F_{p,s}^*}$ , where the arbitrary numerical parameter  $\beta = \beta(n)$ , can accommodate this additional detail.

The preceding analysis is a purely static one; we assume that the materials involved are

perfectly elastic and exhibit no time-dependent behavior. This is not the case for real engineering materials, particularly those commonly in use in fibrillar adhesives such as PDMS, latex, and lightly-cured urethane. In a dynamic picture of interfacial sliding, dissipative mechanisms will come into play and will affect the cleaning picture. Furthermore, deformation in individual fibers or wetting of contaminants can enhance the area of contact  $A$ .

Dissipation by internal relaxation mechanisms (viscous or plastic) will produce an effectively larger shear resistance  $\tau_{\text{eff}}^*$ . The magnitude of the interfacial strength increase will depend on the dissipative properties of the material and the sliding velocity  $v$  [107, 93], so we write:

$\tau_{\text{eff}}^* = \tau^* [1 + \Phi(\text{“lossiness”}, v)]$ . The form of the loss function  $\Phi$  is *a priori* unknown, but it typically increases as the Young’s moduli of the materials decrease and they become more rubberlike. Our measure of lossiness is the ratio of the short timescale/low-temperature modulus  $E_\infty$  to the rubbery modulus  $E_0$ . Assuming a simple relationship like  $\Phi = (E_\infty/E_0) f(v)$ , where  $f$  is an unknown, dimensionless function of  $v$ , we have:

$$\tau_{\text{eff}}^* = \tau^* \left[ 1 + \frac{E_\infty}{E_0} f(v) \right]. \quad (3.8)$$

Figure 3.5 is an exploration of the  $\{E_\infty/E_0, E\}$  parameter space for the fiber material. All the other material and geometrical properties are fixed at the values indicated for Figure 3.3, above. At fixed velocity, we take  $f(v) = \text{constant} = 10$ , for arguments sake. (In a quasi-static picture of frictional sliding, the  $v$  term is a representation of the strain rate in the materials.) An inspection of Figure 3.5 indicates that self-cleaning is inhibited at large values of  $\{E_{f,\infty}/E_0, Ef\}$  and  $E_f$ .

### 3.1.2 Experimental testing of dry self-cleaning on hard and soft GSAs

Polypropylene (PP) fibrillar surfaces were fabricated by molding a 12  $\mu\text{m}$  thick polypropylene film into a 20  $\mu\text{m}$  thick polycarbonate (PC) track-etched membrane filter (ISOPORE, Millipore Inc) containing 600 nm diameter pores, as described previously [41], and shown in Figure 3.6. The resulting fibers are 600 nm in diameter and 18  $\mu\text{m}$  long, with a pitch of  $\approx 1 \mu\text{m}$ . The resulting structures can be seen in Figure 3.8a.

Polydimethylsiloxane (PDMS) (Sylgard 170, Dow Corning) fibrillar samples were manufactured by first fabricating a 33  $\mu\text{m}$  thick steel shim into a ‘comb’ shape with a UV ablation laser, leaving comb dimensions of 25  $\mu\text{m}$  wide teeth at the base, tapering to 15  $\mu\text{m}$  at the tip, 70  $\mu\text{m}$  in length and a pitch of 40  $\mu\text{m}$ . Then with a CNC tool, the comb is used to make progressive cuts into a wax surface [42, 29]. Once cut, PDMS is cast onto the wax mold and the structures are released by peeling. The final fibers are 25 by 33  $\mu\text{m}$  in diameter at the base, tapering to 15 by 33  $\mu\text{m}$  at the tip, 70  $\mu\text{m}$  tall and spaced 40  $\mu\text{m}$  apart. The resulting structures can be seen in Figure 3.8b.

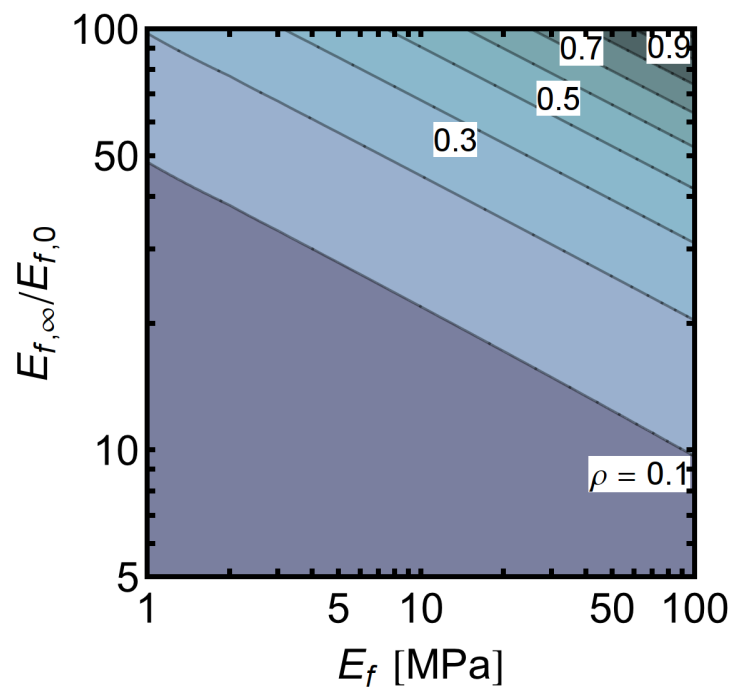


Figure 3.5: The cleaning parameter  $\rho$  for various combinations of fiber modulus  $E_f$  and intrinsic loss parameter  $E_{f,\infty}/E_{f,0}$ . Self-cleaning is poorest at high  $E_{f,\infty}/E_{f,0}$ . Plot contributed by Puthoff, in [43], used with permission.

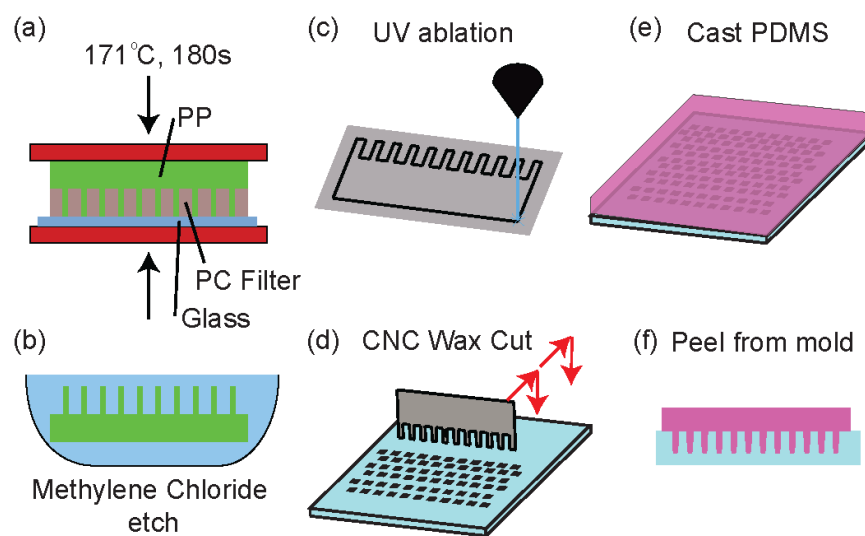


Figure 3.6: Fabrication of the PP and PDMS fibrillar structures. Polypropylene structures are made by (a) molding into a track-etched membrane filter in a hot press and then (b) etching away the filter with methylene chloride. PDMS structures are fabricated by first (c) cutting a  $37 \mu\text{m}$  thick steel shim into a 'comb' shape with a UV ablation laser (d) then with a CNC tool, the comb is used to make progressive cuts into a wax surface. (e) Once cut, PDMS is cast onto the wax mold and (f) released by peeling.

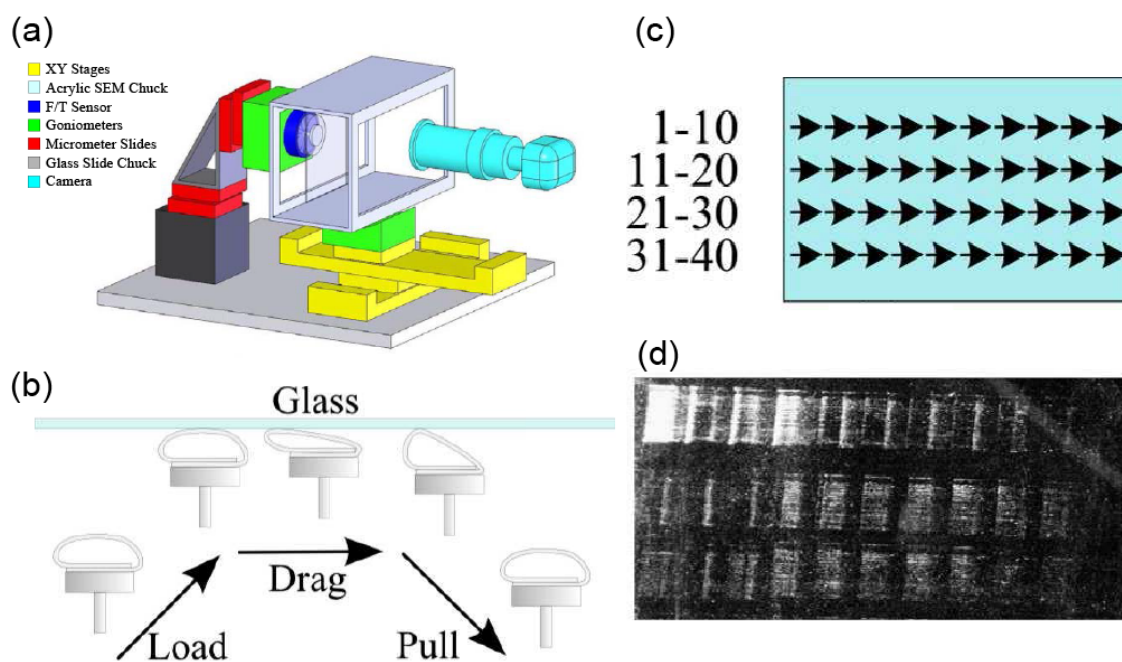


Figure 3.7: (a) Force displacement apparatus block diagram. (b) Load-drag-pull step on glass surface. (c) Spacing of steps after fouling to avoid stepping in contaminated areas of the glass slide. (d) Particles shed on glass after successive steps with a fouled PP fibrillar sample.

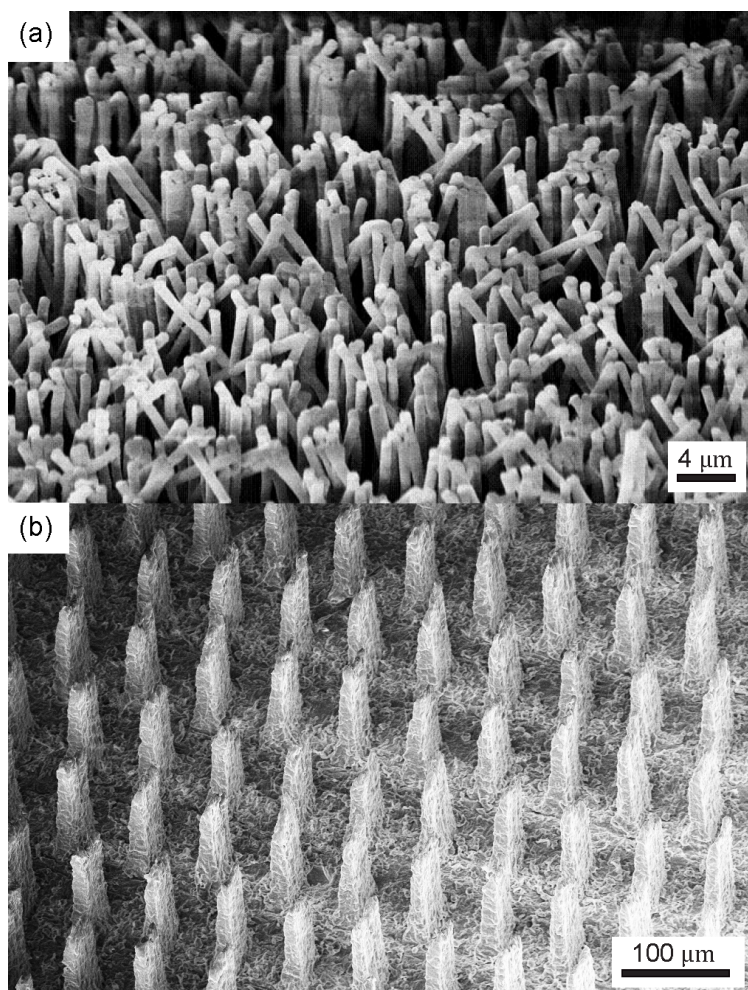


Figure 3.8: (a) An unused clean fabricated polypropylene fibrillar surface. (b) An unused clean fabricated PDMS fibrillar surface.

The custom force displacement apparatus, shown in Figure 3.7a, is described in Gillies 2011 [41]. Load-drag-pull step tests (Figure 3.7b) were performed on a custom built force displacement apparatus that mimics the methods used by Gravish *et al.* [48] and Hansen *et al.* [53], which allows for a repeatable testing protocol. Samples are arranged in a loop to facilitate better contact with the surface, as well as to achieve some level of self alignment.

The self-cleaning property of the GSAs were quantified with a protocol similar to that used by Hansen *et al.* [53] which consists of three stages. In stage one, pre-training of the GSAs was first measured by running nine samples of each type through 50 load-drag-pull steps on clean glass in order to pre-train the fibers. In stage two, samples were stepped across a clean glass slide 40 times, each step in a new location that would act as a benchmark for the self-cleaning steps. In the third stage, the samples are fouled (described below) and then stepped across the same 40 locations used in the benchmark stage so that a direct comparison of the adhesive properties before and after the fouling can be made independent of local substrate conditions.

Fouling of the PP and the PDMS samples was performed by taking a single LDP step on a glass slide coated in one of three types of fouling agents, referred to as small ( $1\ \mu\text{m}$  polystyrene microspheres), medium ( $3\text{-}10\ \mu\text{m}$  glass microspheres) and large ( $40\text{-}50\ \mu\text{m}$  glass microspheres) particles.

### Hard polymer array dry self-cleaning

Figure 3.9a shows an example of a load-drag-pull step of a PP sample before fouling. Stress on the Y-axis is calculated by dividing the measured force by the estimated microfiber contact area, determined from in-situ observations obtained with a camera, using frustrated total internal reflection at the interface of the side-illuminated glass substrate and the microfiber array [86]. During the drag a high shear stress of  $\approx 140\ \text{kPa}$  is measured while the normal stress goes from a compressive state during loading into a slight tensile stress during the drag phase indicating that shear adhesion is taking place, a behavior typical of GSAs.

To measure the effect of fouling on the samples, a recovery ratio is defined as  $\Gamma = (F_{dirt_n})/(F_{clean_n})$ , where  $F_{dirt_n}$  is the maximum shear force during the recovery step  $n$  and  $F_{clean_n}$  is the maximum shear force from the benchmark step  $n$ . Figure 3.10 shows the recovery ratio for the PP fibrillar samples for 40 steps following the fouling step for the small, medium and large particles. Samples recovered  $96\pm 11\%$  of their initial shear adhesion within 10-15 steps on the glass when fouled with small particles, and recovered  $115\pm 12\%$  of their shear adhesion when fouled with large particles. The increase in shear adhesion beyond the initial trials is likely due to fibers continuing to 'train' after the fouling step, as reported by Lee *et al.* [85]. However samples fouled with medium sized particles only recovered  $36\pm 20\%$ . During the self-cleaning steps, particles were left on the glass by the samples, as seen in Figure 3.7d, with the amount of particles left on the glass from each subsequent step decreasing, indicating that the majority of the particles are removed from the sample onto the glass in the first several steps. This was observed with all particle sizes.



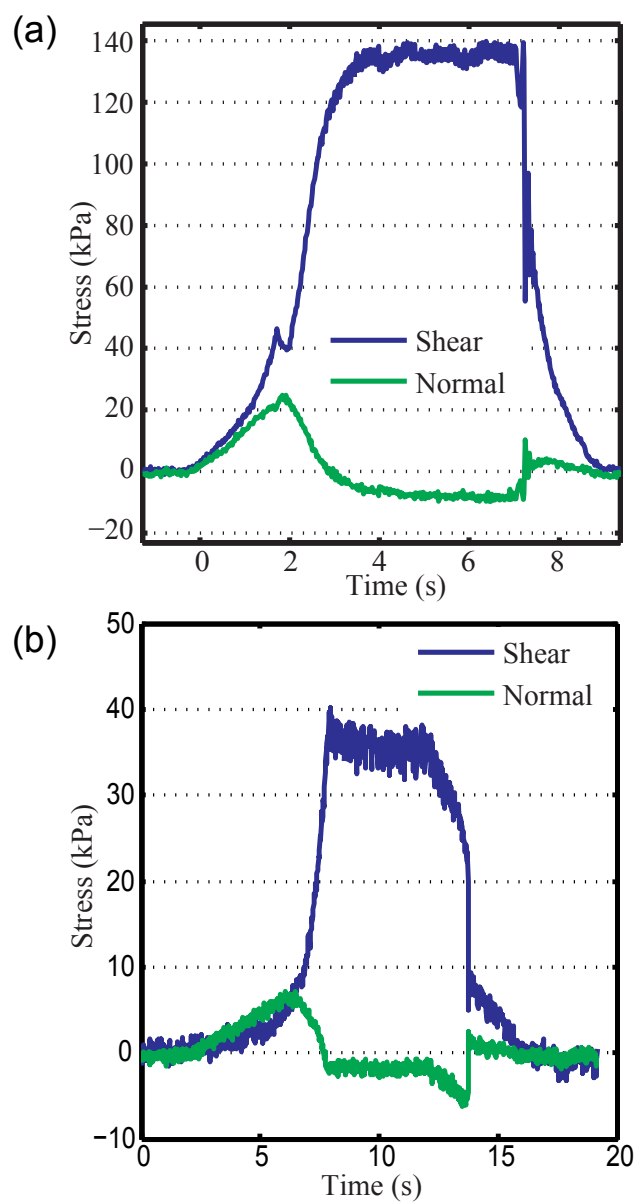


Figure 3.9: A typical load-drag-pull step for: (a) a polypropylene fiber sample on a clean glass substrate. (b) A PDMS fiber sample on a clean glass substrate.

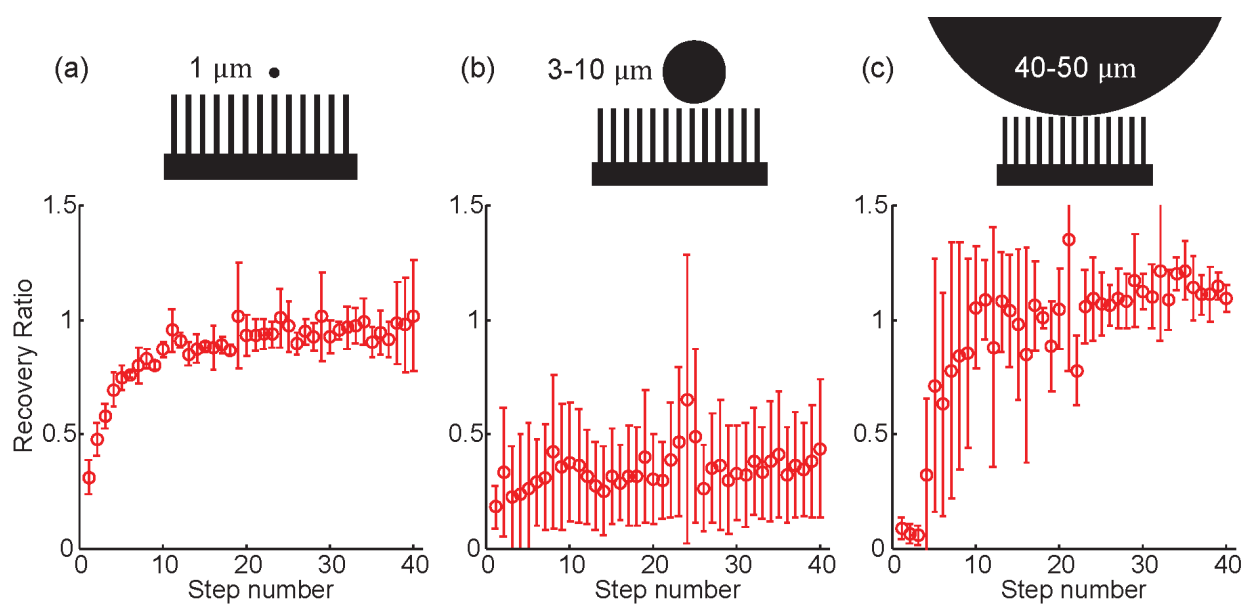


Figure 3.10: The shear recovery ratio  $\Gamma = (F_{dirt,n})/(F_{clean,n})$  for the polypropylene fibrillar surface after fouling with (a) small (mean= $96 \pm 11\%$ ) (b) medium (mean= $36 \pm 20\%$ ) and (c) large particles (mean= $115 \pm 12\%$ ). (N=3 samples for each particle type, error bars are  $\pm$  S.D.)

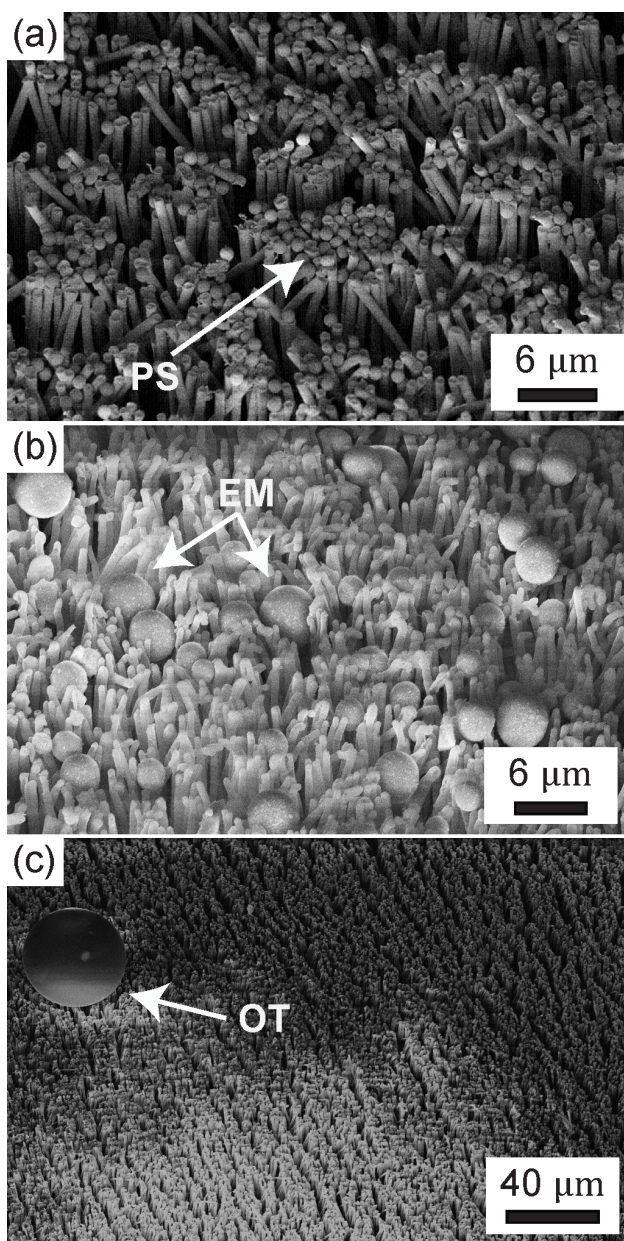


Figure 3.11: (a) Polypropylene fibrillar structures 40 steps after fouling with 1  $\mu\text{m}$  polystyrene spheres, which can be seen between fibers (PS). (b) Fibers fouled with 3-10  $\mu\text{m}$  glass spheres, where some can be seen deeply embedded (EM) between fibers and (c) Fibers contaminated with 40-50  $\mu\text{m}$  glass spheres, only one of which could be found sitting on top (OT) on the sample 40 steps after fouling.

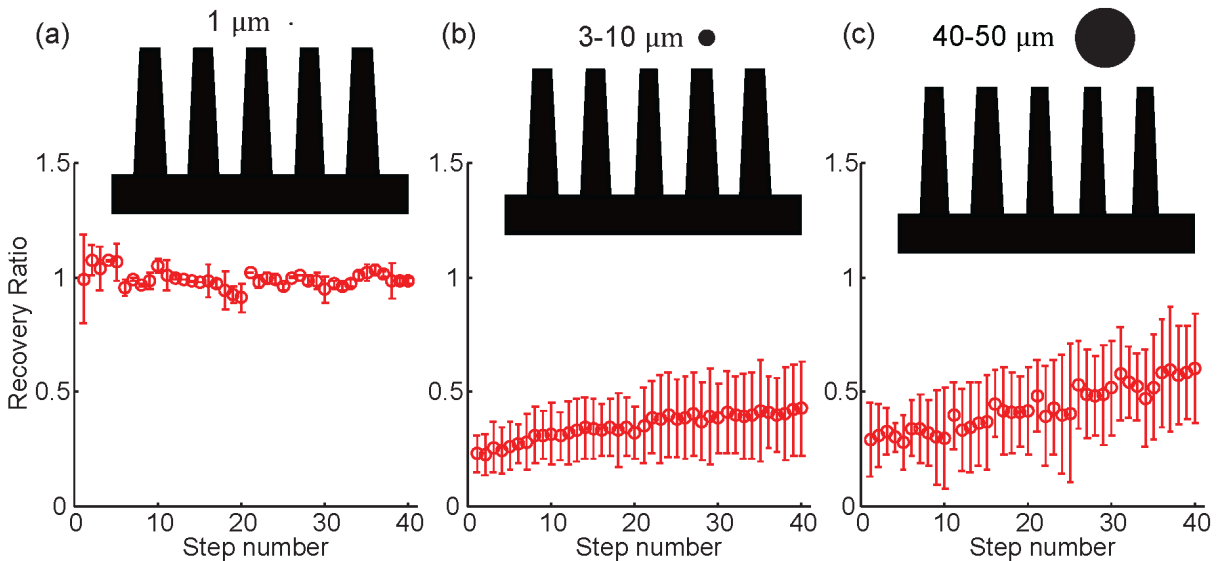


Figure 3.12: The shear recovery ratio  $\Gamma = (F_{dirt.n})/(F_{clean.n})$  for the PDMS fibrillar surface after fouling with (a) small (mean= $99\pm 4\%$ ), (b) medium (mean= $40\pm 15\%$ ) and (c) large particles (mean= $55\pm 18\%$ ). (N=3 samples for each particle type, error bars are  $\pm$  S.D.)

Figure 3.11 shows the PP structures 40 steps after fouling with (a)  $1\ \mu\text{m}$  polystyrene spheres, (b)  $3\text{-}10\ \mu\text{m}$  glass spheres and (c)  $40\text{-}50\ \mu\text{m}$  glass spheres. After the 40 cleaning steps, fibers in the contact zone appear to have shed a majority of the  $1\ \mu\text{m}$  PS spheres, however, some spheres can still be seen on the fibers, adhering to the sides of the fibers below the tips, with others still remaining on top. However, fibers contaminated with  $3\text{-}10\ \mu\text{m}$  glass spheres still have spheres in the contact zone, some being deeply embedded between the fibers. Of the fibers fouled with  $40\text{-}50\ \mu\text{m}$  glass spheres, only a single glass sphere could be found on the sample after the 40 cleaning steps.

### Soft polymer array dry self-cleaning

Figure 3.9b shows an example of a load-drag-pull step of a PDMS sample before fouling. Stress on the Y-axis is calculated as described for the PP fiber samples. From the plot we can see a similar behavior to the PP sample, indicating that shear adhesion of  $\approx 40\ \text{kPa}$  is taking place under a slight tensile load. This is less shear adhesion than the PP samples, but is still performing well for a soft polymer GSA.

Recovery from fouling of the PDMS samples was calculated the same as for the PP samples, using the recovery ratio,  $\Gamma$ . Figure 3.12 shows the recovery ratio for the PDMS fibrillar samples for 40 steps following the fouling step for the small, medium and large particles. When fouled with small particles, PDMS fibers recovered  $99\pm 4\%$  of initial shear

adhesion, however no particles could be seen deposited on the glass during the recovery steps. When fouled with medium and large sized particles, PDMS samples lost  $40\pm 15\%$  and  $55\pm 18\%$  of their initial shear adhesion, respectively.

Figure 3.13 shows the PDMS structures 40 steps after fouling with (a)  $1\ \mu\text{m}$  polystyrene spheres, (b)  $3\text{-}10\ \mu\text{m}$  glass spheres and (c)  $40\text{-}50\ \mu\text{m}$  glass spheres. After the 40 cleaning steps,  $1\ \mu\text{m}$  PS spheres can be seen deeply embedded within the fiber tips, almost to the point of being 'absorbed' by the PDMS. Fibers contaminated with  $3\text{-}10\ \mu\text{m}$  glass spheres are still coated in particles after 40 recovery steps. Fibers coated with  $40\text{-}50\ \mu\text{m}$  glass spheres are also still covered in particles, showing particles embedded between the fibers after the 40 cleaning steps.

### 3.1.3 Discussion of the results

The results indicate that the fouling particle size has a large impact on the self-cleaning properties of the two GSAs. In general, the experimental results are consistent with the analytical prediction that harder fibrillar structures with nanoscale dimensions will dry self-clean more readily than softer fibrillar structures with microscale dimensions. This is evidenced by SEM images showing particles releasing from the PP structures, while becoming deeply embedded in the PDMS structures. As well, a comparison of the empirical recovery ratio between the two GSA types across the various particle sizes (Figure 3.14) reveals that the harder PP structures dry self-clean across a wider range of particle sizes, and that larger particles more readily self clean. These results are supported by the analysis, as seen in Figure 3.4, which shows that smaller fibers and larger particles are more likely to self clean. The analysis also predicts that materials with a higher loss modulus (Figure 3.5 and Figure 3.8) are less likely to self clean, which is also found in the experimental data in Figure 3.14. From this, we can state a general design rule that to maximize adhesion while avoiding fouling, structures with low loss functions,  $E_{f,\infty}/E_{f,0}$ , and smaller fiber diameters,  $R_f$ , are favored.

However, we have observed two phenomena in our experimental data that cannot be explained by our analysis. Namely, the inability of the PP structures to recover from medium sized particles, despite particles observed on the glass substrate after recovery steps, and that PDMS fibers do not lose adhesion from small particle contamination, despite particles found deeply embedded in the fiber tips after the recovery steps. This indicates that there may be several mechanisms in operation that are still not understood.

For the first phenomenon, SEM images of the PP structures after recovery from medium particle fouling reveal  $3\text{-}8\ \mu\text{m}$  particles embedded near the surface of the array. Unlike the  $1\ \mu\text{m}$  PS particles seen between the fibers after recovery, these particles are large enough to disrupt the contact of the fibers with the substrate, preventing them from adhering. We postulate that an intermediate range of particles exists for which they are small enough to fit between the fibers, but large enough to disrupt contact. Once the fibers are too large to become embedded between fibers, they will preferentially shed to the substrate, as seen with the larger  $40\text{-}50\ \mu\text{m}$  particles. Since the analysis does not consider fibrillar spacing, this

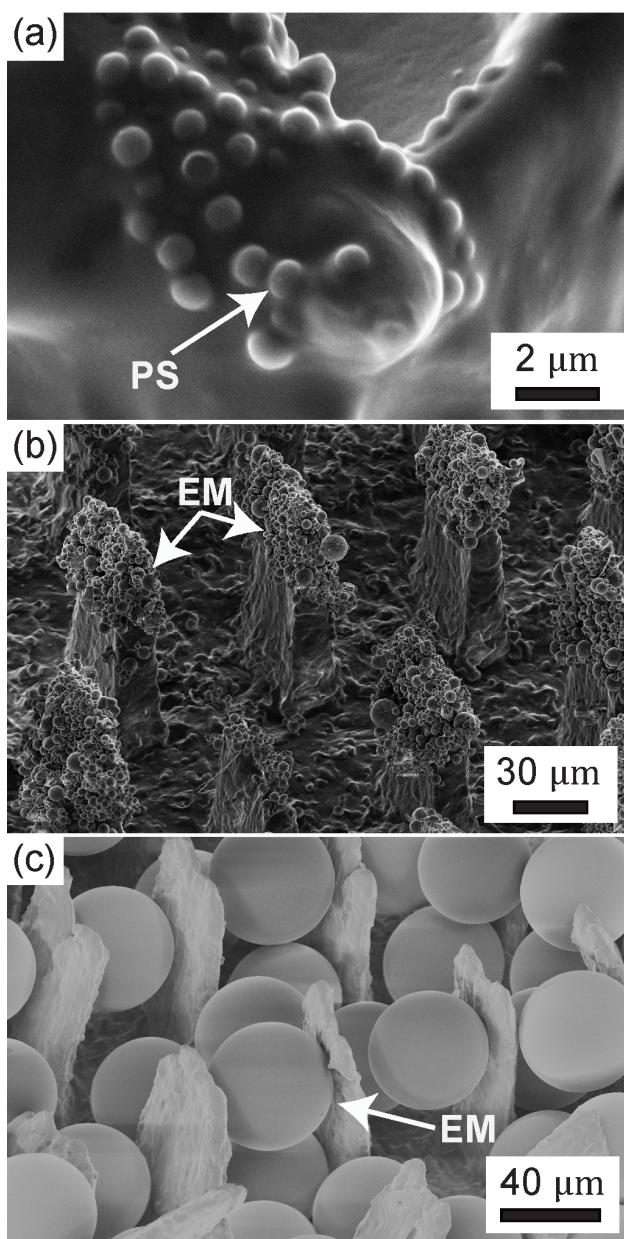


Figure 3.13: (a) PDMS fibrillar structures 40 steps after fouling with  $1\ \mu\text{m}$  polystyrene spheres, which can be seen deeply embedded in the fiber tips (PS). (b) Fibers fouled with  $3\text{-}10\ \mu\text{m}$  glass spheres, where many particles can be seen embedded on the outside of the fibers (EM) (c) Fibers contaminated with  $40\text{-}50\ \mu\text{m}$  glass spheres after 40 recovery steps. Particles can be readily seen embedded between the fibers (EM).

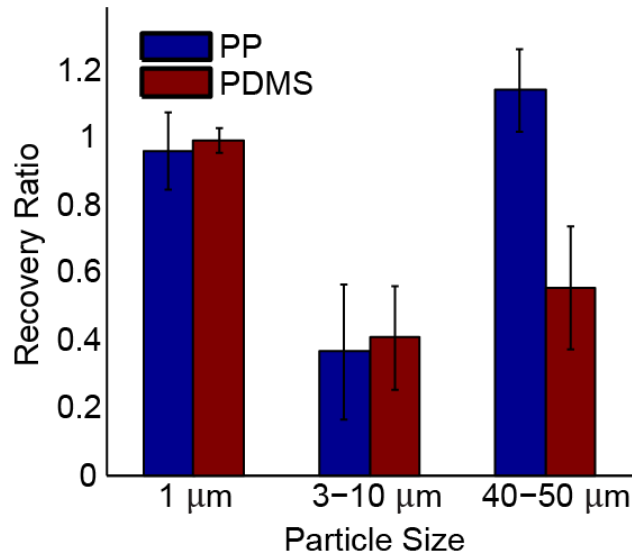


Figure 3.14: Comparison of the PP and PDMS fiber structures dry-self cleaning recovery ratio across the various particle sizes tested.

experimental observation is not captured.

For the second phenomenon, we observe deep embedding of the 1  $\mu\text{m}$  sphere within the PDMS fiber (Figure 3.13a) almost as if the sphere is being absorbed. It could be the case that the PDMS fiber is so soft, and the particle so small that the fiber is able to wrap around the small particle and still make contact with the surface. This type of large deformation is beyond the scope of the analysis, and therefore would not be captured. It is also possible that the PS spheres are so small that they too aid in adhesion by acting as small contact points, or spatulae, increasing contact with the glass.

Furthermore, removal of particles from the fibers to the surface may not be the only mechanism by which the samples are recovering adhesion. PS microspheres seen on the SEM image of the PP sample after cleaning indicate that recovery is occurring despite their presence. It is possible some particles are pushed down between the fibers, away from the surface where they were first interfering with the fibers. Also, it is possible that some particles are being removed to the substrate during the lifting phase, in the normal direction, instead of being cleaned in shearing. As well, large clumps of particles at the trailing edge of the contact zone indicate that fibers are being brushed backwards off the sample. This may be why the loop geometry is able to recover much more shear adhesion than the 30% recovery reported by Lee *et al.* [84]. The loop structure gives a shorter path along which the particles can escape, as opposed to the long flaps used previously by Lee *et al.* [84].

## 3.2 Dry self-cleaning with active control of soft polymer fibers

Although soft polymer GSAs do not show the same dry self-cleaning properties as the stiff fiber counterparts, there is still interest in a soft polymer GSA capable of shedding particles due to their relative ease of manufacture, their superior performance for larger area pads, and for applications where soft polymer GSAs are already being employed, such as in a dynamic climbing robot [16]. To increase the versatility and effectiveness of soft GSA materials, and to improve self-cleaning capabilities, we studied active controllable adhesion to spherical particles with the new soft polymer GSA.

Recent efforts have investigated switchable adhesion via chemical functionality and topography, with some success by means of pH or temperature changes [72]. Switchable adhesion has been shown by Jeong *et al.* in a nontransferring dry adhesive in transport of large smooth surface such as LCD screens, and Kim *et al.* created a microstructured elastic surface capable of transfer printing by modulating pressure on flat stiff objects [67, 76]. Nadermann *et al.* [96] also showed a fibrillar surface terminated by a continuous film can be switched between two metastable states which show markedly different adhesive properties as shown by normal load-pull tests.

The literature also offers several examples of actively controlled fibrillar surfaces. Belardi created magnetic artificial cilia fabricated from photoreactive copolymer precursors filled with magnetic nanoparticles by a new photolithographic process [12]. The cilia are operated in a fluidic environment for micromixing, but adhesion to the array was not reported. Evans produced high aspect ratio nanorod arrays of a PDMSferrofluid composite material, and exhibited actuation for applications in photonics and sensing [36]. Northern fabricated a GSA on nickel cantilevers that, when actuated, decreased the adhesion of the structure to a glass flat punch [97]. However, to the authors knowledge, no examples exist of a GSA showing controllable adhesion to particles for the purposes of particle capture and control. Here we report a new GSA made from a magnetoelastomer (ME) composite material actuated by an external magnetic field. The GSA is comprised of parallel microfabricated wedge-shaped microridges that are 100  $\mu\text{m}$  wide at their base, and taper to less than 10  $\mu\text{m}$  thick at their tips. The microridges are 325  $\mu\text{m}$  long, and are formed in 15 mm wide rows, 325  $\mu\text{m}$  apart, similar to earlier work [54].

ME composites are a new class of materials, generally involving a dispersion of carbonyl iron particles in a poly-dimethyl siloxane (PDMS) network [21]. Such materials have an elastic stiffness that can be tuned by an external magnetic field. To increase the magnetic reinforcement effect, the ME composite can also be cured under a magnetic field in order to align the carbonyl iron particles during curing [132]. Relevant examples of devices that employ this material to effect a change in mechanical response include a microfluidic mixer capable of large deformations and a tunable elastic stiffness member capable of changes in elastic modulus of 10x [90, 87].



### 3.2.1 Fabrication of magneto-elastomer composite adhesive ridges

Microridges are fabricated by first creating a wax mold with similar techniques mentioned above. The mold is formed by melting paraffin wax on a glass slide at 80 °C, with a thickness of 3 mm, and allowed to cool so that the top surface is smooth and uniform. The glass slide is then mounted into a custom-built 3 axis CNC machine, consisting of 3 microstepper stages (Zaber T-LSR150A) aligned with 2 two manual rotation stages (Newport RSP-2) and two linear slides with micrometers (Newport 423 slide) used for fine adjustment. The entire apparatus is mounted onto an air table (Newport VH series). The cutting tool (Bits and Bits, Profile Tool 10 degree 3.175 mm x 38.1 mm) is mounted in the CNC chuck, and guided by the stages to cut 15 mm long slices in the wax that are 325  $\mu\text{m}$  deep and have a row spacing of 325  $\mu\text{m}$ . 125 rows are cut, giving a mold that is approximately 15 x 40 mm, similar to methods used previously [54, 122, 41].

The magnetoelastomer composite is formed by first mixing the liquid PDMS base (Mold Max 20, Smooth-On Inc.) with carbonyl iron powder, 6-9 micron particle size, ( $\geq 99.5\%$ , Sigma-Aldrich) in a 25 by weight ratio. Once the base and the carbonyl iron are thoroughly mixed by hand, the PDMS curing agent is added and thoroughly mixed. The mixture is cast into the wax mold and degassed in vacuum at 5 kPa abs for 10 minutes. After degassing, a second glass slide is placed over the liquid PDMS mixture, with a 400 g weight on top. This stack is then placed over a 5 x 5 x 0.635 cm Grade N42 nickel plated neodymium rare earth magnet (K and J Magnets). The weight prevents the magnetoelastomer from bulging in the magnetic field. The elastomer is then allowed to cure in the presence of a permanent magnet, 4 mm from the bottom surface, with a field strength of approximately 2000 Gauss (Fig. 3.15). During curing, the carbonyl iron particles form into chains that are aligned with the magnetic field. The microridge array is demolded after curing for 24 hours at room temperature. Cross sections of the resulting material reveal the alignment of the carbonyl iron particle chains with the magnetic field (Fig. 3.16).

### 3.2.2 Results

The effective elastic modulus of the array was tested by using a sphere indentation apparatus similar to that described by Schubert [119]. A glass sphere indenter, with a radius of 20.3 mm was brought into contact with the array, under displacement control using a microstepper stage (Zaber T-LSR150A), while forces were recorded with a 6-axis force-torque sensor (Nano43, ATI Industrial Automation Inc.). Normal force measurements were used in conjunction with surface displacement measurements to determine the effective elastic modulus by the following equation [44]:

$$F_{normal} = \frac{4E_{eff}}{3(1-\nu^2)} \sqrt{R_p h^3} \quad (3.9)$$

Where  $\nu$  is the Poisson's ratio, taken here to be 0.5,  $R_p$  is the radius of the probe and  $h$

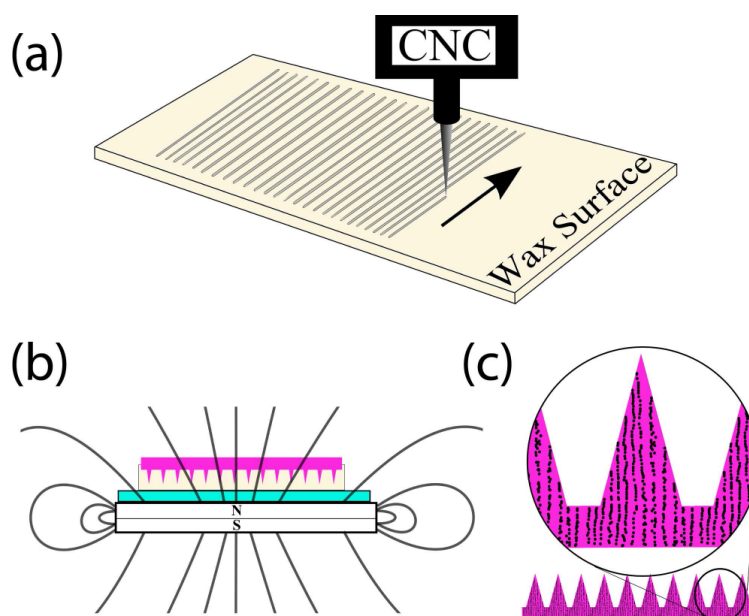


Figure 3.15: Fabrication of the magnetoelastomer micridges. (a) A wax surface is inscribed with a custom-built 3 axis CNC machine. (b) The magnetoelastomer material is cast into the wax mold, and allowed to cure in a magnetic field. (c) While curing, the carbonyl iron particles align to form chains along the direction of the magnetic field.

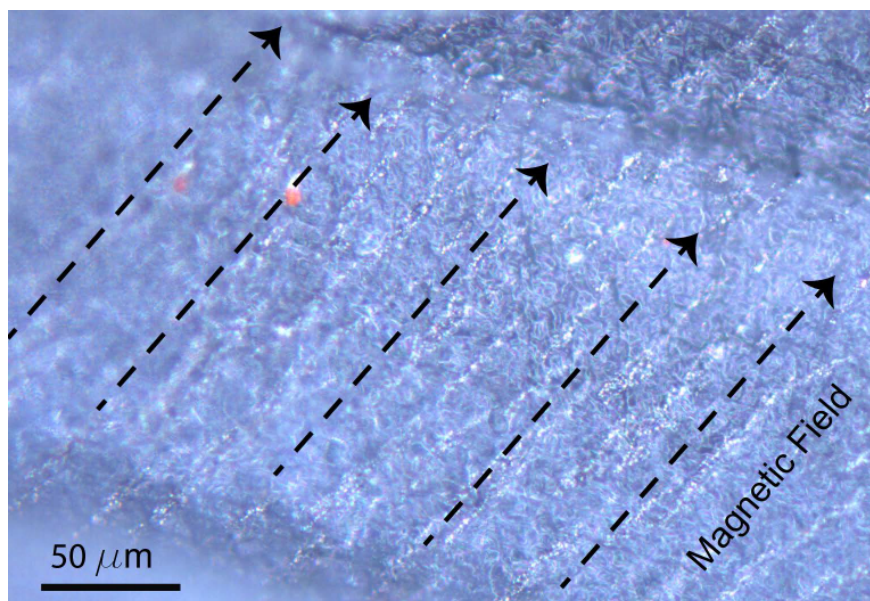


Figure 3.16: ME microridge, viewed from the side, showing chains of carbonyl iron particles (white), cured into alignment with a magnetic field (dashed black line).

is the height of indentation from the neutral surface position. The results (Fig. 3.17) show a low slope at the beginning of the indentation as the ridges bend over, and then a steepening of the curve as the ridges fully compress, and the backing begins to depress. From the above equation, an effective elastic modulus of 65 kPa is calculated for the vertical ridge surface, 1.4 MPa for the magnetically flattened surface, and 1.5 MPa for the control surface, at an indentation depth of 125  $\mu\text{m}$ . 125  $\mu\text{m}$  is used at the nominal indentation depth because this is the approximate ridge penetration depth as observed in images of spheres on the array. Figure 3.17 shows that vertical ridges are greater than 10 times more compliant at indentation depths of 125 microns, as compared to the flat actuated ridges, which at the same indentation level have effectively the same elastic modulus as a flat control surface.

Actuation of the array is tested by placing the material near a 1x1x0.5 in nickel plated neodymium magnet (K and J Magnetics). Placing the magnet within 5 mm of the array causes the microridges to bend into alignment with the magnetic field, and as the magnet is moved away, the microridges return to their original vertical position (Fig. 3.18). Using an online magnetic field calculator (K and J Magnetics online field calculator, available at <http://www.kjmagnetics.com/calculator.asp>), the array deflection is plotted as a function of the magnetic field strength (Fig. 3.19).

Adhesion was tested using a 2-axis wire cantilever force sensor and an optical dissection microscope (Zeiss) connected to a computer via a digital camera (Paxcam). The cantilever, made from copper wire measuring 0.21 mm in diameter, had a glass sphere of varying size

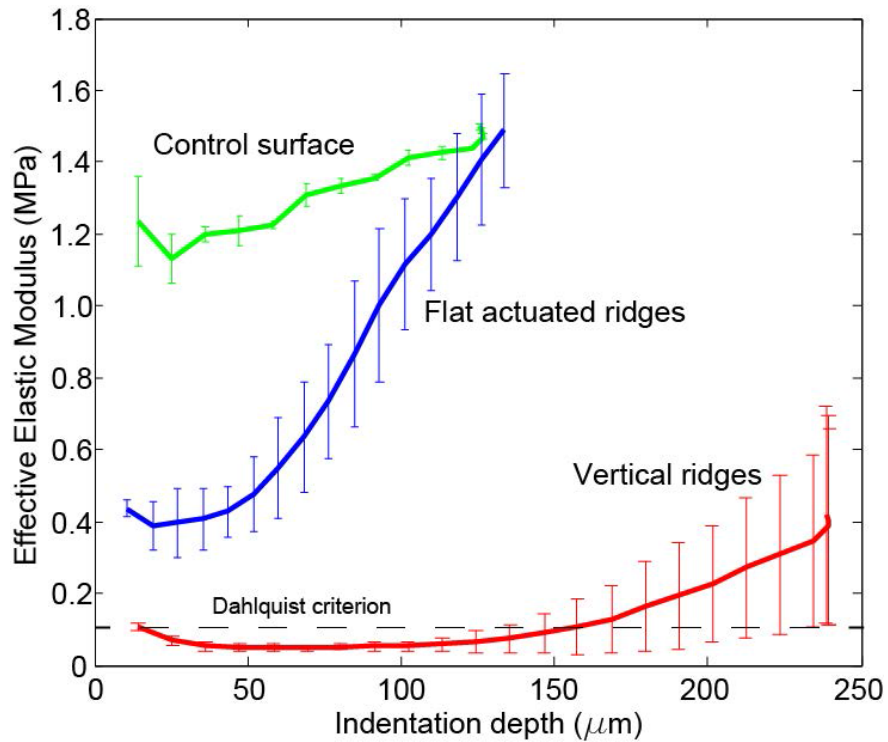


Figure 3.17: Results from a sphere indentation test show that vertical ridges are greater than 10 times more compliant at indentation depths of 125 microns, as compared to the flat actuated ridges, which at the same indentation level have the same compliance as a flat control surface ( $N=3$ , error bars are 1 s.d.). Vertical ridges also fall under the Dahlquist criterion for tack.

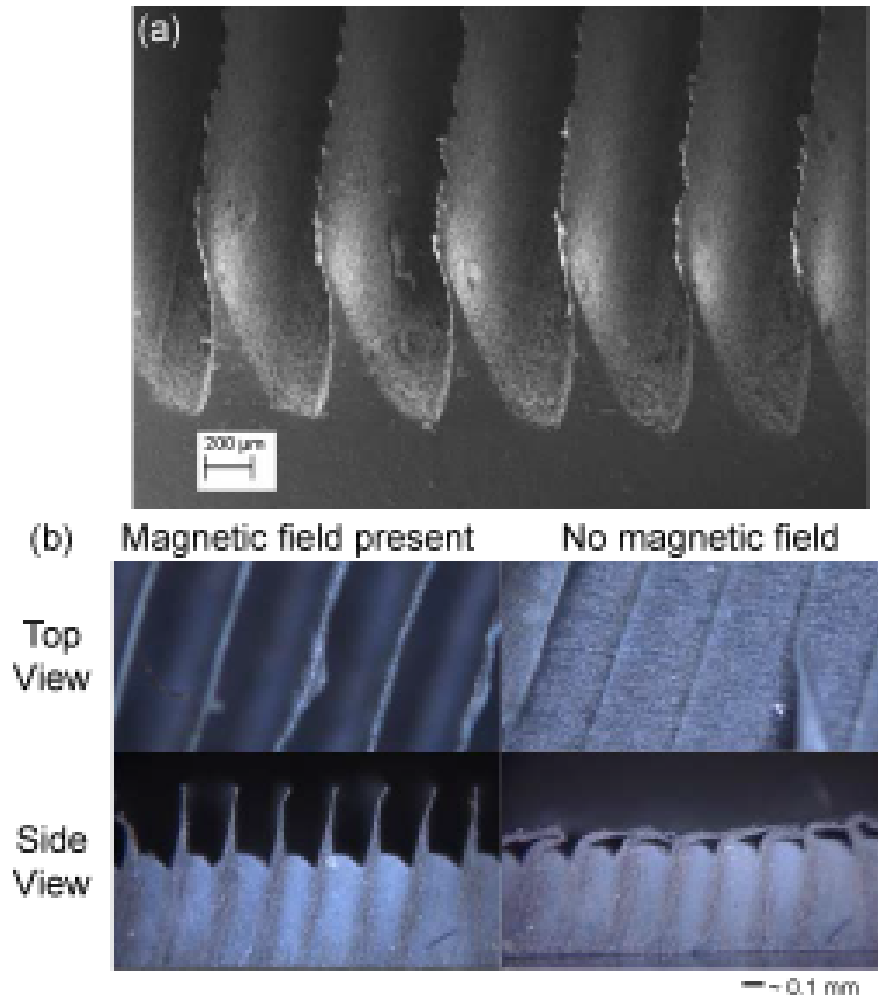


Figure 3.18: (a) SEM of the completed magnetoelastomer microridges. The microridges are 325 microns long, 15 mm wide, and taper from 100 microns at their base to less than 10 microns at the tip. (b) Actuation of the ridges, as seen from the top and side. In the presence of a magnetic field, the ridges completely flatten.

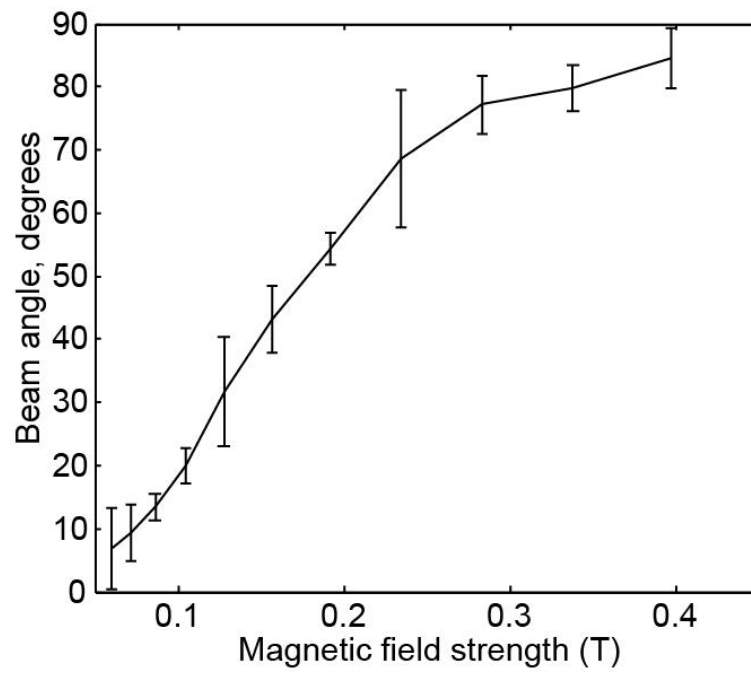


Figure 3.19: The microridge deflection from vertical as a function of the external magnetic field strength.

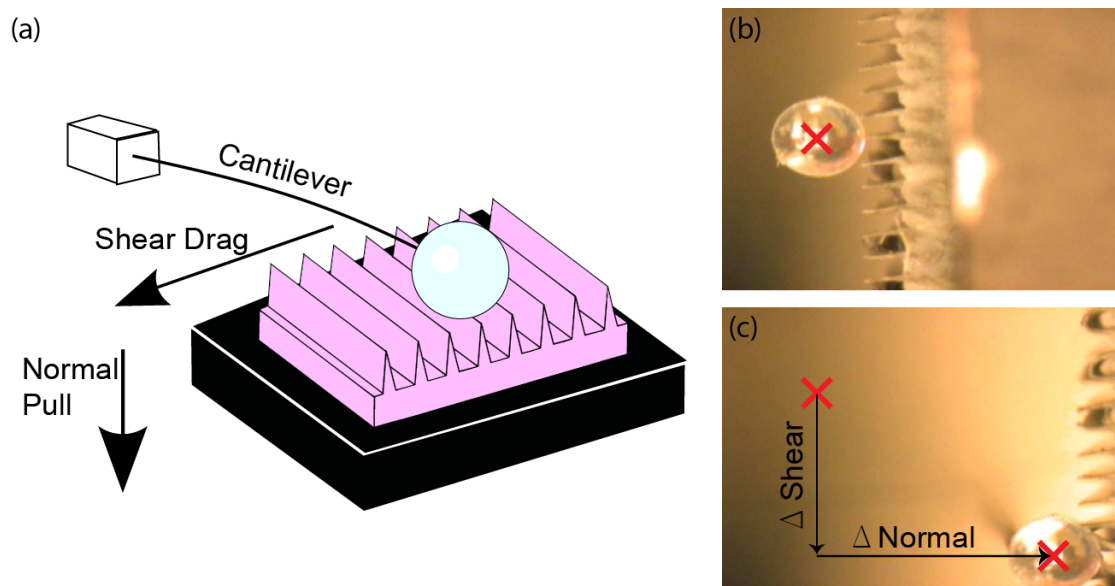


Figure 3.20: (a) Schematic of the 2-axis wire cantilever apparatus used to test normal and shear adhesion between a glass sphere and the ME composite microridges. (b, c) Images of a sphere adhering to the micridge array, showing normal and shear displacements. (Video of test attached as supplementary information)

affixed to the tip via cyanoacrylate glue. The ME ridges were brought into contact with the glass sphere using two Newport linear slides with micrometers (Newport 423 slide). Deflections of the cantilever were recorded during the load-drag-pull tests using the software package Tracker (Tracker Video Analysis and Software Tool, Copyright (c) 2012 Douglas Brown). From the deflection measurements, adhesive forces can be calculated via Euler beam bending, where  $F_{adh} = 3EI\frac{\Delta}{l^3}$ . Taking deflections in the normal and transverse directions is translated into normal and shear adhesion (Fig. 3.20).

Adhesion was tested on arrays in the vertical unactuated position and in the flattened actuated position with sphere probe sizes of 0.5 and 1 mm diameter. For the vertical position, results show that normal adhesion has a strong dependence on the shear load placed on the sphere (Fig. 3.21). This effect, known as shear-induced normal adhesion, is a common feature of GSAs, and is used to control the normal adhesive strength by adjusting the shear loading on the array [5]. When the array is flattened in the presence of a magnetic field, the normal adhesion shows no dependence on the shear load, and the adhesion is ten times less than the vertical orientation. Adhesion tests on a smooth ME composite control sample confirm that the flattened ridges are effectively behaving like a smooth surface.

A proof of concept apparatus was also created to show how the material could be used for particle removal and release. Using a 3-axis displacement apparatus, the MR micridge

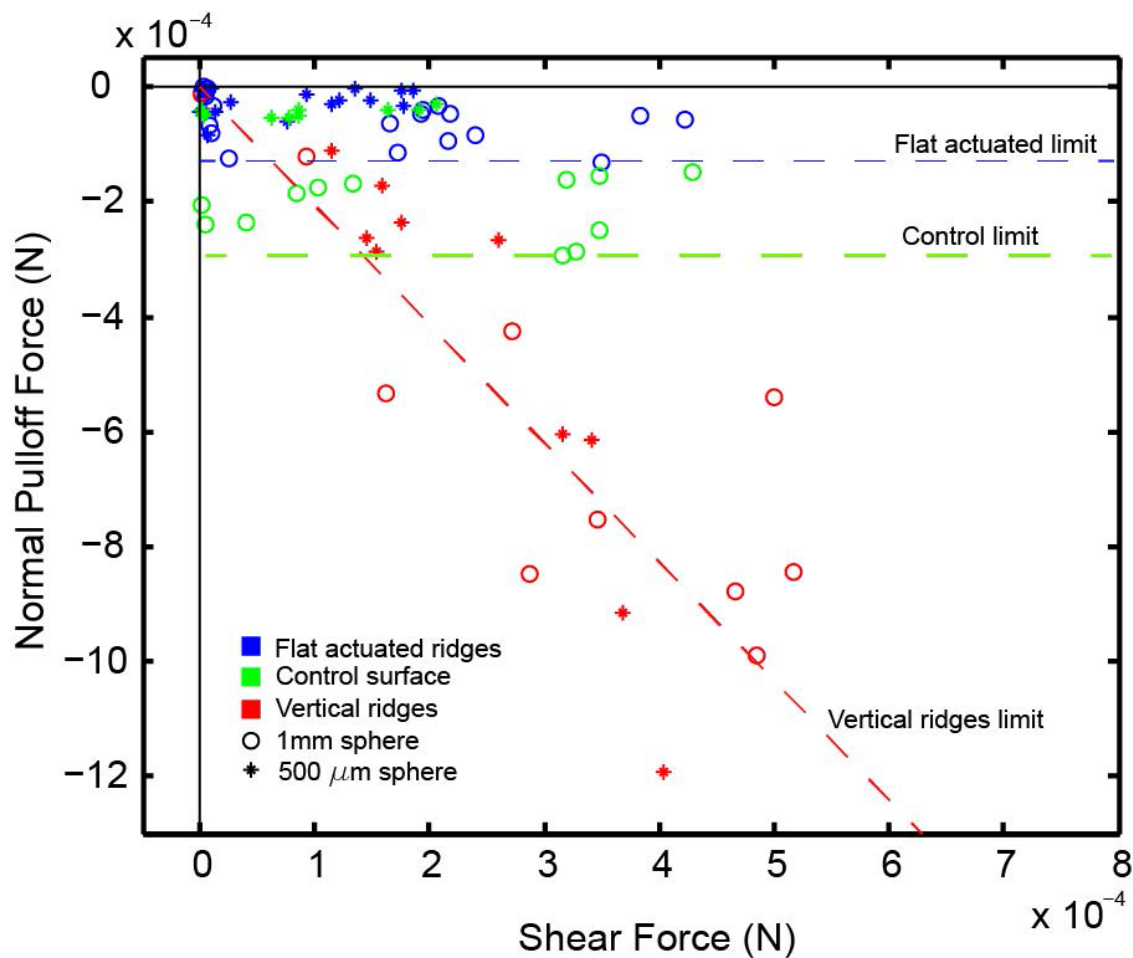


Figure 3.21: Data from sphere pull-off tests show that the microridge surface has a strong shear-induced normal adhesion effect while the ridges are vertical (red). Once ridges are activated and lie flat, the material acts the same as a smooth control sample and has 10x less normal adhesion (blue). A smooth flat control surface (green) shows slightly larger adhesion than the flat actuated ridges. Open circles are 1mm spheres, asterisks are 500 micron spheres.



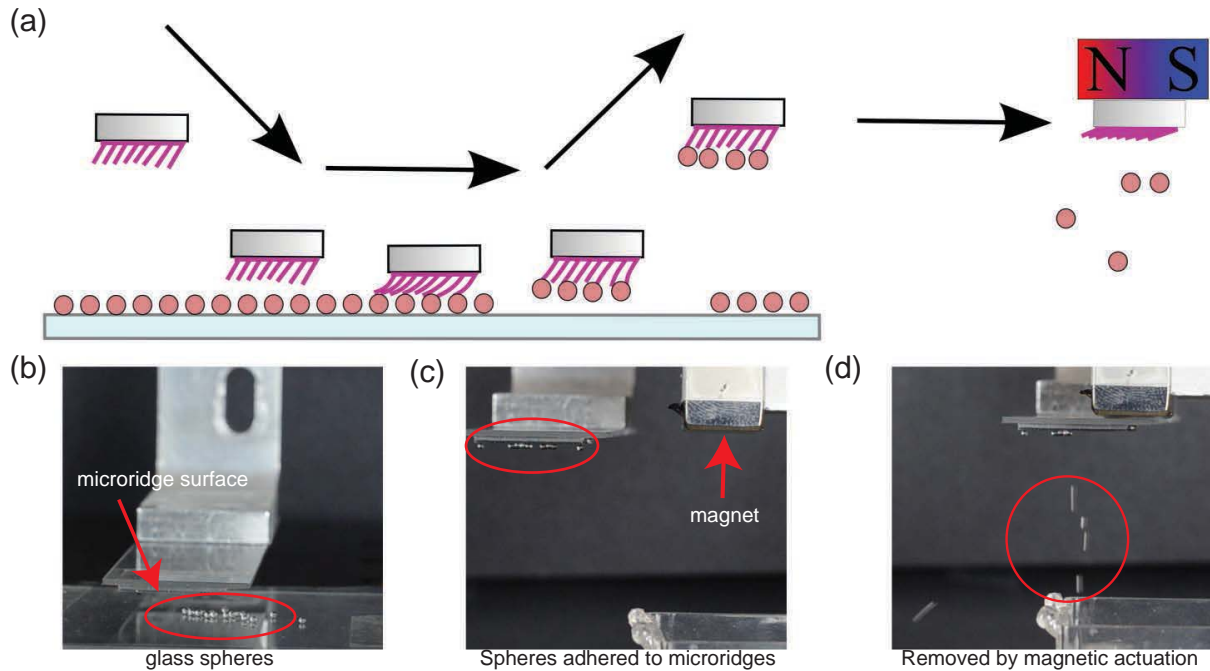


Figure 3.22: (a) A proof-of-concept test in which the ME composite microridges are used to remove particles from a surface before being transported and actuated to release the particles into an adjacent hopper. (b) Stills from video showing microridges (c) picking the particles off a surface and then (d) actuation of the microridges, causing particle detachment into the hopper. A video of the test is attached as supplementary information.

material was brought into contact with glass slide covered with 500-1000 micron glass spheres. When sheared, the microridges adhere to the glass spheres, and the material is retracted. It is then moved to a permanent magnet. Once near the magnet, the microridges collapse flat, the adhesion with the spheres is lost, and the spheres fall into a hopper (Fig. 3.22). A video of this test is available in the supplementary information, showing that nearly all the particles are transported from the glass surface into the hopper.

### 3.2.3 Modeling of fiber bending controlled by an external magnetic field

To determine the magnetic field strength necessary to flatten the ridges, we solve for the equilibrium of torques acting on the beam [71]. We consider two torques, the elastic torque arising from the bending stiffness of the ridge,  $T_{elastic}$ , and the magnetic field torque,  $T_{magnetic}$ . Considering the large deflections observed, the elastic term is developed by considering the microridge as a rigid plate with a torsional spring at its base, with  $T_{elastic} = K_{eq}\theta$ . The

equivalent stiffness of such a spring is:

$$K_{eq} = c_o \frac{EI}{l} \quad (3.10)$$

where  $E$  is the Youngs modulus of the magnetoelastomer composite,  $I$  is an approximation of the second moment of area,  $l$  is the length of the microridge and  $c_o$  is a parametric angle coefficient [57]. A magnetic material, such as carbonyl iron, having magnetization ( $M$ ), will experience a torque ( $T_m$ ) in a magnetic field. This torque will rotate the magnetic moment into alignment with the magnetic field, and has strength:

$$T_{magnetic} = V_m \vec{M} \times \vec{H} \quad (3.11)$$

where  $V_m$  is the volume of the magnetic material, and  $H$  is the magnetic field strength. The direction of the magnetization of the material is assumed to be along the length of the particle chains, parallel to the length of the ridges, while the strength of the magnetization is assumed to be at the saturation limit of carbonyl iron, 1.6 MA/m due to the presence of the strong magnetic field [1]. The resulting available torque from a misalignment between the external magnetic field and the ridge direction is:

$$T_{magnetic} = V_m \left| \vec{M} \right| \left| \vec{H} \right| \sin(\gamma - \theta) \quad (3.12)$$

Where  $\gamma$  is the angle of the fixed external magnetic field, and  $\theta$  is the angle the ridge has deflected from its neutral position. Considering the ridge to be at equilibrium when  $T_{elastic} = T_{magnetic}$  we get:

$$\theta = \frac{V_m \left| \vec{M} \right| \left| \vec{H} \right|}{K_{eq}} \sin(\gamma - \theta) \quad (3.13)$$

This transcendental equation is solved numerically using Matlab. Due to the large non-linearities and non-constant cross-section of the microridge profile, the approximate model was verified by using a simple macroscale prototype, which was created as a simple analog to verify the above analysis. The prototype consists of a nickel shim, 75  $\mu\text{m}$  thick, cut into flaps measuring 15 mm wide and 2.5 mm long. The flaps are attached to the base via a polyethylene terephthalate flexure layer, 12  $\mu\text{m}$  thick and 0.25  $\mu\text{m}$  wide. The nickel flaps approximate nickel plates with hinges at their base, which have a stiffness approximated by  $K_{eq} = EI/l$ , where  $E$ ,  $I$  and  $l$  are the polymer flexure modulus, second moment of inertia and length [57]. The deflection of the flaps is measured from horizontal in a magnetic field, and the strength of the magnetic field is controlled by placing a permanent magnet at varying distances from the flap in manner such that the orientation of the magnetic field is always vertical. Magnetic field strength is calculated using an online magnetic field strength calculator available at <http://www.kjmagnetics.com/calculator.asp>. Ridge deflection,  $\theta$  vs

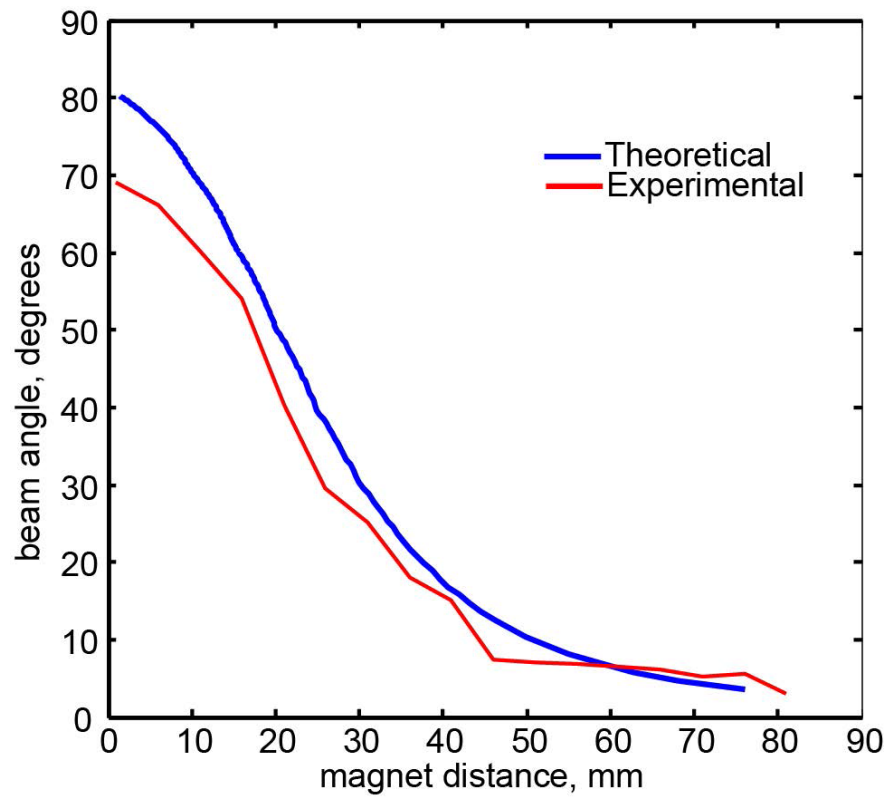


Figure 3.23: Theoretical analysis of beam angle has good agreement with a macroscale prototype of the ME composite microridges, and shows the beam angle dependence on the distance from a 2.5x2.5x1.25 cm neodymium magnet.

magnetic field strength is shown in Fig. 3.23, and the results show good agreement between the experiments on the macroscale prototype and the model.

A difference in the adhesive properties between the vertical and flattened positions can be explained by the change in effective stiffness between the two states. Previous studies have shown that below an elastic modulus of approximately 100kPa, known as the Dahlquist criterion, the material surface becomes tacky [26]. A stiffer material, with a modulus well above the Dahlquist criterion can be made to have an effective modulus below 100kPa through only the geometric design in its surface. Considering the surface of the microridge material to be made of cantilever beams, we can calculate the change in effective stiffness between the vertical and flattened ridge position [9, 44]. Assuming a sphere comes to rest between two ridges, we can approximate a contact with the ridges,  $\theta$ , to be  $75^\circ$ . Following Autumn's cantilever model, [9] we calculate the effective elastic modulus as:

$$E_{eff} = \frac{3EID \sin(\varphi)}{L^2 \cos^2 \varphi} \quad (3.14)$$

Using the ridge dimensions as above, and taking the Young's modulus of the ME composite to be 1.5 MPa (determined by indentation experiments), we get an effective elastic modulus of 35 kPa, well below the Dahlquist criterion. This change in effective stiffness of the surface can be used in the Johnson Kendall Roberts (JKR) theory of contacting elastic solids to explain the change in adhesion between the two states. We use, as an approximation, the change in shear strength of the interface to predict the shear induced adhesion seen in Figure 3.21, and described Schubert *et al.* [119] and Tian *et al.* [127] For a rigid sphere on a flat elastic plane, the area of contact is related to the elastic modulus in JKR theory [69] as:

$$A_{JKR} \propto E^{-2/3} \quad (3.15)$$

Looking at the ratio of contact areas between the two cases, we get  $A_{vertical}/A_{flat} \propto (E_{flat}/E_{vertical})^{2/3}$  and from the measured values above,  $E_{vertical}=75$  kPa and  $E_{flat}=1$  MPa, we find an area ratio of 5.6 between the two cases. Assuming that the shear strength is proportional to the area of contact,  $F_f \propto A_{JKR}$ , we would expect to see a 5.6x increase in shear strength between the two cases, which is slightly less than the 10x increase we see in figure 3.21.

Differences between the above model and the experimentally determined effective elastic modulus (Fig. 3.17) of the array can be explained by nonlinearities arising from the complex shape of the ridges, as well as the large strains not considered in the model. However, the underlying principle remains intact, that being, in the vertical position, the ridges approximate a tacky surface. When the ridges are in the flat state, the effective elastic modulus approximates the bulk properties of the PDMS composite material, and the adhesion is lost. The surface now acts as if it had no microridge structures.

### 3.3 Concluding remarks

The ability of gecko-inspired synthetic adhesives to dry self-clean during use has many potential interesting applications such as in wall crawling robots, reusable adhesives, microfabrication and solar panel cleaning and microparticle capture and control where other methods of particle control are not sufficient. With the rapid advancement that the GSA field has gone through in the past several years, we are getting closer to seeing these controllably adhesive systems employed for these uses. Work presented in this chapter represents important advancements in the properties and also the design of GSA that will hopefully contribute to making these uses a reality.

We have investigated the impact of two design parameters on the dry self-cleaning capability of GSAs by experimentally testing two GSAs after fouling with small ( $1\ \mu\text{m}$ ), medium ( $3\text{-}10\ \mu\text{m}$ ) and large ( $40\text{-}50\ \mu\text{m}$ ) particles. We found that a GSA made from a hard thermoplastic with nanoscopic fibers was able to recover 96-115% of its shear adhesion after fouling with small and large but not medium particles, while a GSA made from a soft polymer and microscopic fibers recovered 40-55% on medium and large particles. Further examination by SEM revealed that the PDMS structures were not shedding the smaller particles during recovery steps, but were instead being absorbed into the surface, and that, regardless of their size, particles did not release from the PDMS surface.

An analysis of the contact strength between fibers, particles and substrates of various dimensions and elasticity reveals that dry self-cleaning will be more effective for GSAs fabricated with smaller fiber diameters and for GSAs fabricated from materials with smaller loss functions, such as hard thermoplastics. This has important implications on the choice of materials and geometries used for GSAs when dry self-cleaning capability is a desired function in the material, and indicates that hard polymer GSAs with smaller fiber diameters are less prone to fouling.

As indicated by results of dry self-cleaning on a passive soft polymer fibrillar adhesive, we set out to design a system with active control and release of particles. We have demonstrated controllable adhesion to glass spheres with a new magnetically actuated synthetic gecko adhesive made from a magnetoelastomer composite. Capable of controlling adhesion to glass spheres  $500\ \mu\text{m}$  to  $1\ \text{mm}$ , this represents an important step in realizing an adhesive with dry self-cleaning capabilities across a wide range of particle sizes.

Clearly there is a compromise between the adhesive properties currently achievable with the soft polymer structures and the dry self-cleaning properties of the hard thermoplastic fibrillar surfaces. Future work may involve integrating the microscale adhesive properties of the soft adhesive with the nanoscale adhesive properties of previously published hard polymer adhesives. This will make possible the next generation of reusable controllable adhesives that demonstrate dry self-cleaning across many orders of magnitude in particle size.

# Chapter 4

## Fibrillar surface robustness

### 4.1 Material limits of hard polymer fibrillar surfaces

Natural gecko array wearless dynamic friction has recently been reported for 30,000 cycles on a smooth substrate [49]. Following these findings, stiff polymer gecko-inspired synthetic adhesives have been proposed for high cycle applications such as robot climbing [6], industrial gripping systems [67], and automobile tires where controllable adhesion, reusability, durability and long lifetime are desired properties.

There has been limited research done into the high cycle behavior of GSAs. Parness [99] reported a low elastic modulus polymer wedge shape structure that maintained 76% of shear and 67% of normal adhesion over 30,000 cycles in controlled conditions, however no failure mechanism was identified (although some have suggested fouling of low elastic modulus polymers during use may be problematic [3, 40]). GSAs made from high elastic modulus polymers such as polypropylene have shown high shear forces and frictional adhesion [119, 86] as well as the ability to self-clean during use [84] and adhere to certain non-planar surfaces [83], however there have been no investigations of their high cycle behavior. Wear of bulk high elastic modulus thermoplastics in long lifetime applications such as in prosthetic joints and bearings has also been well studied [35, 17], but GSA's radically different geometry and interfacial adhesive forces are likely to show a different failure mode. Here we examine the behavior of high density polyethylene (HDPE) and polypropylene (PP) microfiber arrays during repeated cycles of engagement on a glass surface to identify possible material limits for these polymers' use in GSAs.

#### 4.1.1 Experimental testing of hard polymer thermoplastic arrays

Fibrillar surfaces were fabricated using two polymers; polypropylene (PP,  $E=1.5$  GPa) and high density polyethylene (HDPE,  $E=0.4$  GPa) with a modification of a fabrication process previously reported [86]. The fibrillar surfaces in each case were fabricated by molding either a  $50\ \mu\text{m}$  thick PP film or a  $60\ \mu\text{m}$  thick HDPE film into a  $20\ \mu\text{m}$  thick polycarbonate (PC)

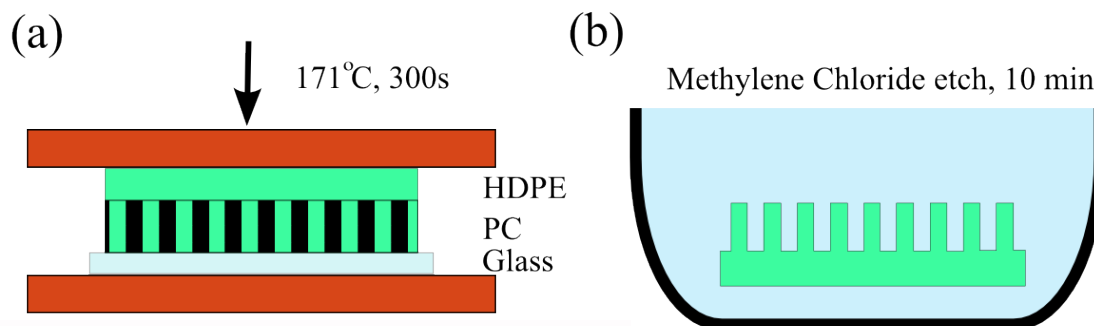


Figure 4.1: (a) Molding of HDPE film into PC filter (b) Etching of PC filter in methylene chloride.

track-etched membrane filter (ISOPORE, Millipore Inc) containing  $600\text{ nm}$  diameter pores. Samples were molded in a hydraulic press at  $171^\circ\text{C}$  for 300 seconds and allowed to cool for 45 minutes before being released (Figure 4.1). The PC filter was then etched in methylene chloride to release the molded fibers. The resulting samples were rinsed in isopropyl alcohol and air dried (Figure 4.5a & b).

We performed load-drag-pull step cycles on a custom built force displacement apparatus (Figure 3.7 (a)) that mimics the methods developed by Hansen and Autumn [53]. The apparatus consists of two main components. The first is an acrylic SEM stub chuck attached to a 6 axis force torque sensor (ATI AI Nano 43 F/T sensor) and a goniometer (Newport GON-U-60) and two linear slides (Newport 423 slide) with micrometers attached for fine adjustments and alignment. The second component is a custom built aluminum frame used to rigidly hold a glass microscope slide. This is mounted on two perpendicular stepper motor controlled linear stages (Zaber T-LSR 150B) and a second goniometer. The entire apparatus is mounted onto an air table (Newport VH series) to dampen vibrations and encased in an acrylic box to prevent external contamination, and also electrically grounded.

Load-drag-pull steps were performed on the apparatus under displacement control for the HDPE and PP loop mounted samples to simulate their use in robot feet or industrial grippers as seen in Figure 3.7b. Samples were mounted in a loop configuration in order to increase compliance of the system and improve alignment with the substrate to allow repeatable testing on the force displacement apparatus. Interestingly, the shear stress of 300 kPa generated by the PP loop samples are 3-4 times larger than the previously reported flat sample's 90 kPa for a similar fibrillar surface [86], and close to the reported 540 kPa for natural gecko lamella [86]. Each sample material was subjected to 150, 300 and 10,000 load-drag-pull cycles consisting of a 2 mm drag at 0.4 mm/s.

Figure 4.2 describes how contact area of the fiber patch was calculated.

The forces generated by an HDPE and PP sample during an engagement cycle for trial

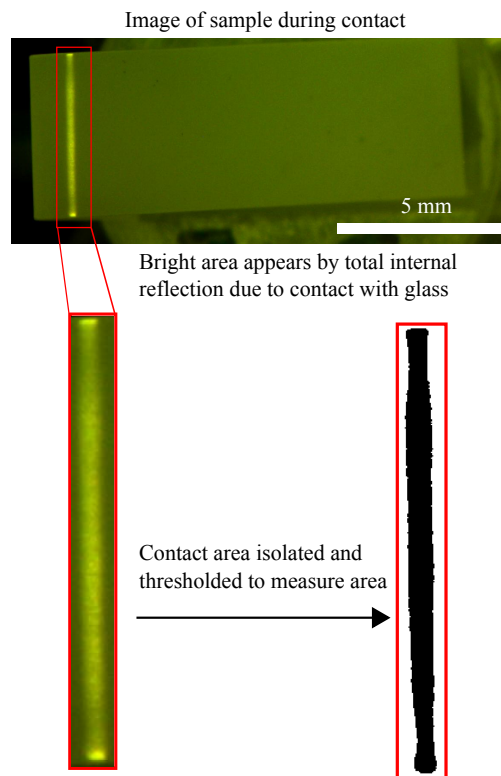


Figure 4.2: Contact area of the fiber sample is calculated by total internal reflection.



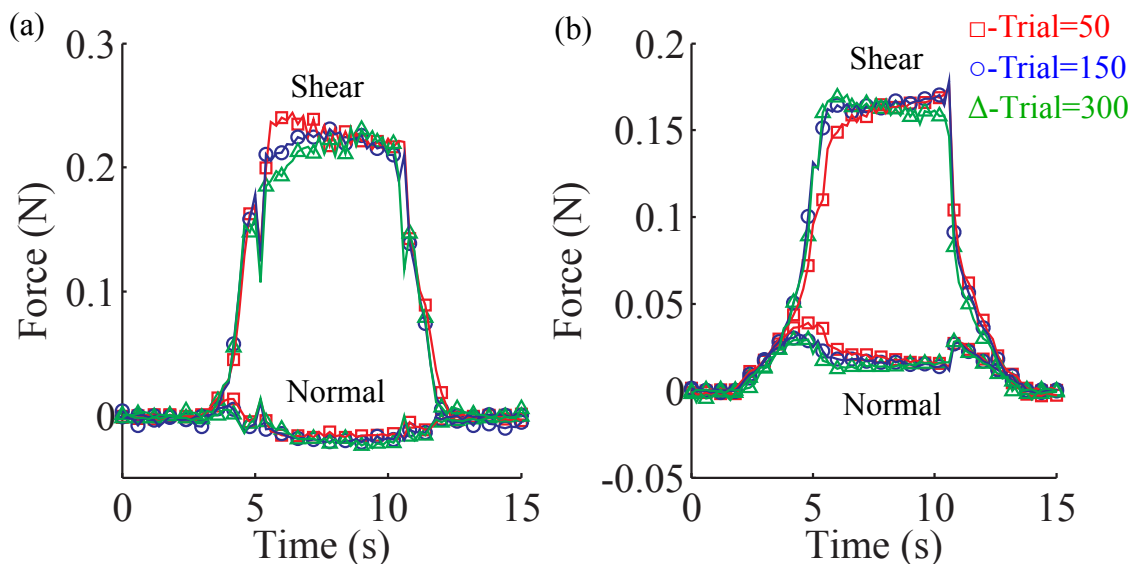


Figure 4.3: Load-drag-pull steps for (a) HDPE and (b) PP fiber samples for trial 50, 150 and 300, showing the three phases of a single trial and correlation between cycles 50, 150 and 300.

number 50, 150 and 300 are shown in Figure 4.3. A normal preload of 40 kPa for PP samples and 15 kPa for HDPE samples occurs during the load phase of the cycle. This is followed by a rapid increase in shear to 300 kPa as the samples adhere. During the drag phase, a high shear force is maintained while the normal force goes from compressive to tensile, indicating that frictional adhesion is taking place; a behavior typical of gecko adhesives (PP sample normal forces decrease to nearly zero, but never become tensile). All forces then return to zero as the sample leaves the surface.

Over the course of the 300 trials, the HDPE samples maintain high peak shear forces while the normal force remains tensile (Figure 4.4). During the first 20-30 trials, a large increase in shear force is seen, which has been previously described as a training phenomenon in which the fibers angle and cause a greater adhesion with the counter surface [86]. Over the course of 10,000 cycles, peak shear forces gradually decrease to 54% of initial for PP fibers, and 63% for HDPE fibers.

After 150 cycles, a small amount of deformation is observed on the HDPE tips, with increasing deformation after 300 cycles into 100 nm thick 'spatula' (Figure 4.5). PP samples only show deformation after 300 cycles, and much less than the HDPE samples. By 10,000 cycles, the HDPE and PP fibers are heavily deformed, and the observed spatulae appear to be fusing together. Previously published results [86] never showed this type of deformation, most likely because they were only tested for 150 cycles, which was insufficient to bring about the level of deformation reported here.

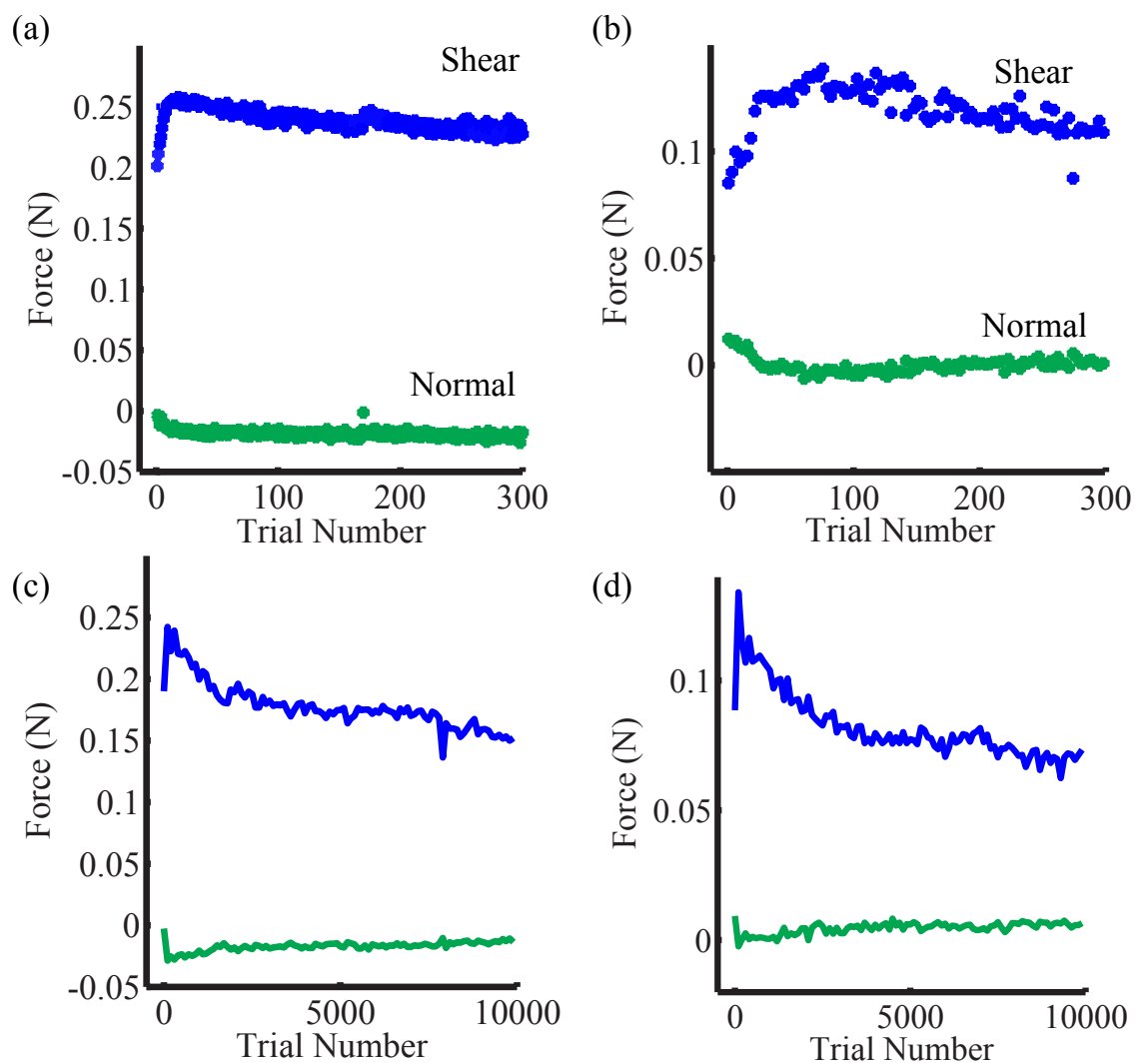


Figure 4.4: Maximum shear force and the corresponding normal force for 300 load-drag-pull steps of (a) HDPE and (b) PP fibers showing no significant change in peak force over the course of the first 300 trials. For 10,000 load-drag-pull steps of (c) HDPE and (d) PP fibers, shear forces eventually start to decrease.

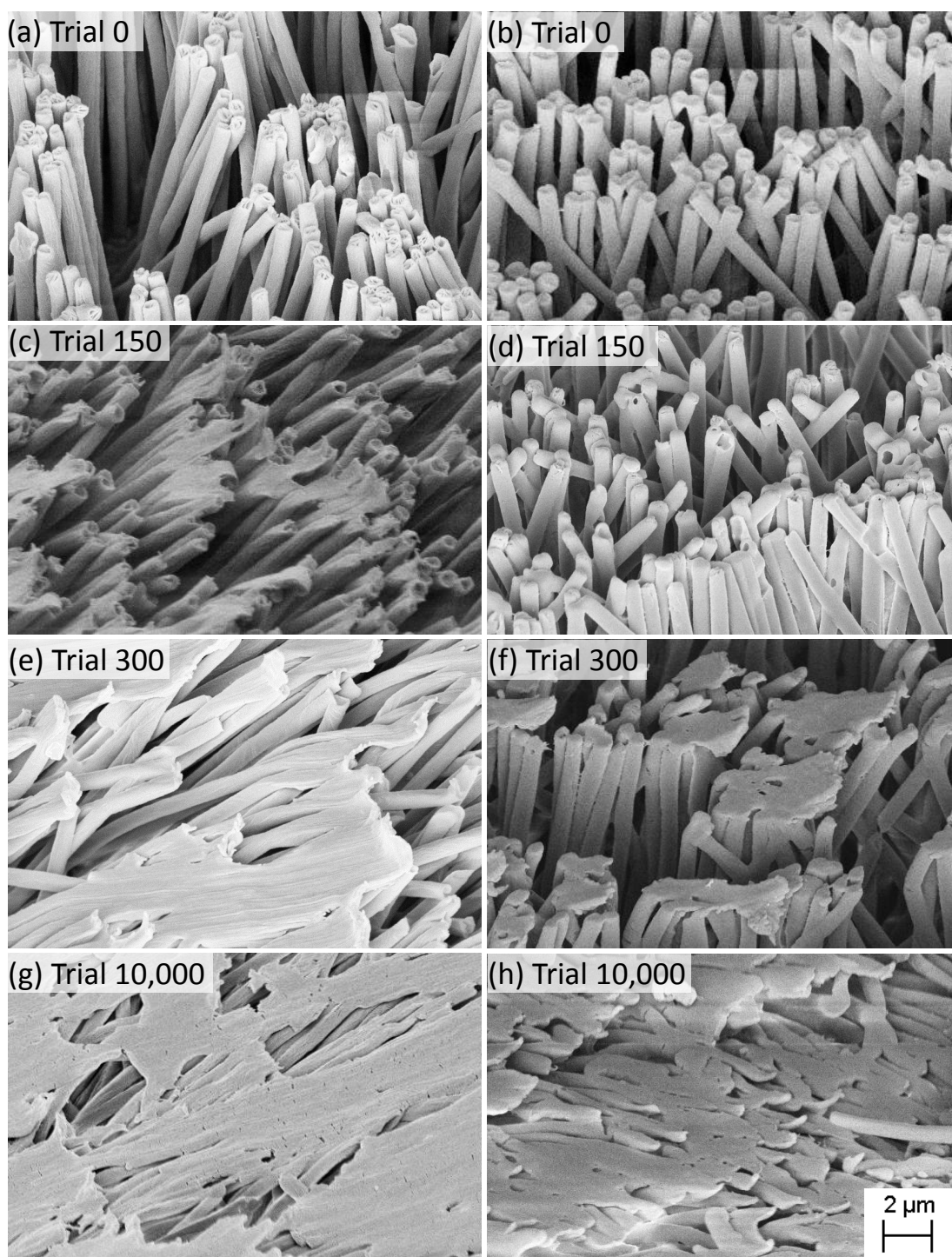


Figure 4.5: SEM images of HDPE (left column) and PP (right column) after 0, 150, 300 and 10,000 cycles, showing progressive plastic deformation of the fibers over the course of the trials.

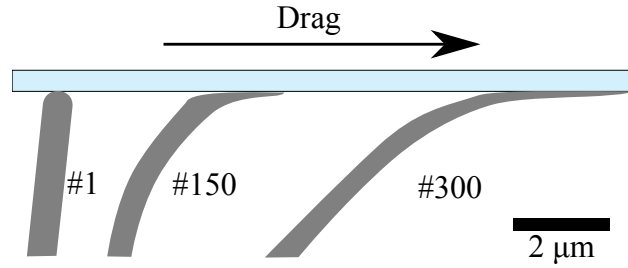


Figure 4.6: Progressive deformation observed on the fibrillar samples can be explained by visco-plastic creep deformation as described by Freed [37]. Stresses calculated at the fiber tips are consistent with values required to induce creep deformation.

### 4.1.2 Mechanisms of failure

To explain the large amount of plastic deformation observed in Figure 4.5, three possible mechanisms are discussed; fiber tip melting, visco-plastic creep deformation and adhesive wear.

#### Fiber-tip melting

A simple heat transfer calculation was used to estimate if sufficient power is produced at the surface to induce melting. By calculating the maximum force on a single fiber,  $F_{fiber}$ , the maximum force measured, 0.244 N, divided by the fiber density,  $42 \times 10^4 \text{ fibers}/\text{mm}^2$  multiplied by the contact area,  $A = 0.853 \text{ mm}^2$  as imaged by frustrated total internal reflection [85] (Figure 4.2), we estimated the power produced at a single fiber interface as:

$$P = F_{fiber} \vec{v} \quad (4.1)$$

where  $\vec{v} = 4 \times 10^{-4} \text{ m/s}$  is the sliding velocity, and  $P = 2.7 \times 10^{-10} \text{ W}$ . We treat this as a 1-D heat transfer problem, where the resistance of the glass and the fiber can be used to calculate the temperature at the fiber-glass interface. The interface temperature is determined using Fourier's heat equation:

$$\Delta T = \dot{Q} R \quad (4.2)$$

where  $\Delta T$  is the change in temperature between the interface and the backing,  $\dot{Q}$  is the heat generated (where  $\dot{Q} = P$ ) and  $R = 1.6 \times 10^8 \text{ K/W}$  is the combined resistance of the fibers and the glass. The calculation shows that the energy dissipated at the interface during the drag is only enough to raise the interface temperature by less than  $1 \text{ }^\circ\text{C}$ . This was also verified by the fact that no heating of the glass substrate could be measured during the course of the experiments with an IR thermometer (Extech model 42510A).

### Viscoplastic creep deformation

The large amounts of plastic deformation seen at the tips of the fibers could also be attributed to shear stresses that develop at the fiber tip due to adhesion with the glass by Van der Waals bonding, as illustrated in 4.6. These shear stresses could cause visco-plastic creep deformation as described by Freed [37] and Ward [134, 135]. Ward describes the viscoelastic nature of yield through the use of the Eyring theory, which gives the relationship between the strain rate, the applied stress and the temperature of the material. This explains that creep will occur at temperatures above the glass transition temperature and at stresses below the yield stress. By measuring the contact area during the drag phase, the density of the fiber array, and calculating the contact area of a single fiber as previously reported [85, 120], we calculated the stress on a single fiber to be approximately 1.5 MPa over a period of approximately  $5 \times 10^4$  seconds. This is about 10 times less than the yield stress of HDPE and PP, yet high enough to cause creep failure at room temperature. As well, since the fibers are inclined, the reported shear loads transform to a significant axial load on each adhering fiber, resulting in similar loads to those reported by Chrissman, who reported creep failure of a high density polyethylene at a load of 1 MPa after  $10^4$  seconds in uniaxial tension [25]. Creep deformation is also evidenced in the SEM images by the lengthening of the fibers with an increasing number of trials.

### Adhesive wear and plowing

It is also possible that there is some level of adhesive wear taking place at the interface. Adhesive wear occurs when bonding between two materials sliding under a compressive load causes one material to fail and remain adhered to the second material, followed by plastic deformation at the surface. This is evidenced in the SEM images, however, this generally occurs above a pressure-velocity threshold, which has not been reached in our experiments [13]. As well, the fibers do not appear to be wearing down, or losing a significant amount of material which would result in their shortening; in contrast, the fibers appear to become longer. Given that the geometry and size scale of our structures fall outside the classical definitions for creep deformation and adhesive wear failure mechanisms, it can not be ruled out that the actual mechanism for plastic deformation is a combination of both, occurring at a nanoscopic level. A comparison of the possible failure modes is given in Table 4.1.

Interestingly, although the fibers are being plastically deformed within the first 300 trials, the shear forces do not decrease until after many more cycles. This may be due to the formation of the observed 'spatulae' shapes at the fiber tips. However, after 300-10,000 cycles, the 'spatulae' appear to be fused together. This fused structure may not be able to make as intimate contact with the surface as the original fibrillar structure, and therefore may not form the same Van der Waals bonding, resulting in the decreased adhesive forces seen in 4.4 [50, 10, 9]. Below we discuss importance of the spatula structure and preliminary

Table 4.1: Comparison of failure modes.

Observation	Adhesive wear condition	Y/N?	Creep deformation condition	Y/N?	Melting	Y/N?
Pressure*Velocity < $1.2 \times 10^{-5}$ MPa m/s	PV Limit for HDPE > 0.1 MPa m/s [13]	N	Creep occurs > 10% of yield stress	Y	$\Delta T = 1^\circ\text{C} \ll \Delta T_{melt}$ for melting $\approx 130^\circ\text{C}$	N
Fiber elongation greater than 10%	Fibers shorten from material loss	N	Fibers stretch from chain mobility	Y		-
No wear debris	Removal of wear particles	N	Remains monolithic	Y		-
Plastic flow at fiber tips	Ploughing or material separation	Y	Stress near tip	Y		-

work on the fabrication of such structures.

## 4.2 Preliminary work on spatula fabrication

Many synthetic gecko adhesives currently being developed have approximately hemispherical tip shapes, which have contact forces described by the model outlined in Chapter 5. The analysis using the Johnson Kendall Roberts contact analysis for a sphere adhering to a flat surface, and comparing this to the pull-off force for a flap-terminated fiber, reveals that the film terminated fiber gives much larger adhesive forces. In contrast to the spatula plates found on the gecko system, hemispherical shaped tips also cannot adhere well to rough surfaces due to the high elastic energy required in straining the fiber tips to conform to the surface.

As well, work by Majidi and Fearing [89] has shown that the spatula feature is critical for adhesion on surfaces with roughness on the size order of the fiber tips. A contact analysis of a rectangular elastic plate adhering to a sphere, (exemplifying the spatular plate adhering to an asperity on a rough surface), shows that below a critical spatula plate thickness, the plate will spontaneously adhere to a spherical surface of radius  $\geq \rho$  (Equation 4.3). The study revealed that to adhere to 300 nm radius asperities, the spatula plate must be less than 20 nm in thickness.

$$\frac{w^2}{128(1-\nu^2)\rho^4} + \frac{H^2}{12(1-\nu)\rho^2} \leq \frac{W_{ad}}{EH} \quad (4.3)$$

The spatula can also be credited with the reversible nature of the gecko adhesion system. Models analyzing the spatula terminal plate as a peeling film have shown that at low angles of pull, detachment forces are quite high, and upon reversal of the pull direction, adhesion can be changed over 3 orders of magnitude [127]. As well, Persson [102] has shown analytically that the very thin geometry of the plate (10 nm), results in an extremely low bending elastic stiffness, allowing molecular forces to dominate the stored elastic energy and bring the plate into contact with the surface. This is critical on rough surfaces, where larger geometries are unable to conform to the surface, and the structures spontaneously detach due to low true contact area.

Results from Cheng, Chen and Gao [24] have shown that as the spatula plate adheres to a surface, pre-tension within the spatula may occur. This pre-tension has been shown analytically to be important in the reversible nature of the gecko adhesive system, and that the thickness of the spatula plate is a critical parameter for adhesion and reversibility. Specifically, given a certain pretension,  $P_o$ , they have determined that there is a critical angle below which strong attachment will occur, and above which the spatula will spontaneously detach (Equation 4.4).

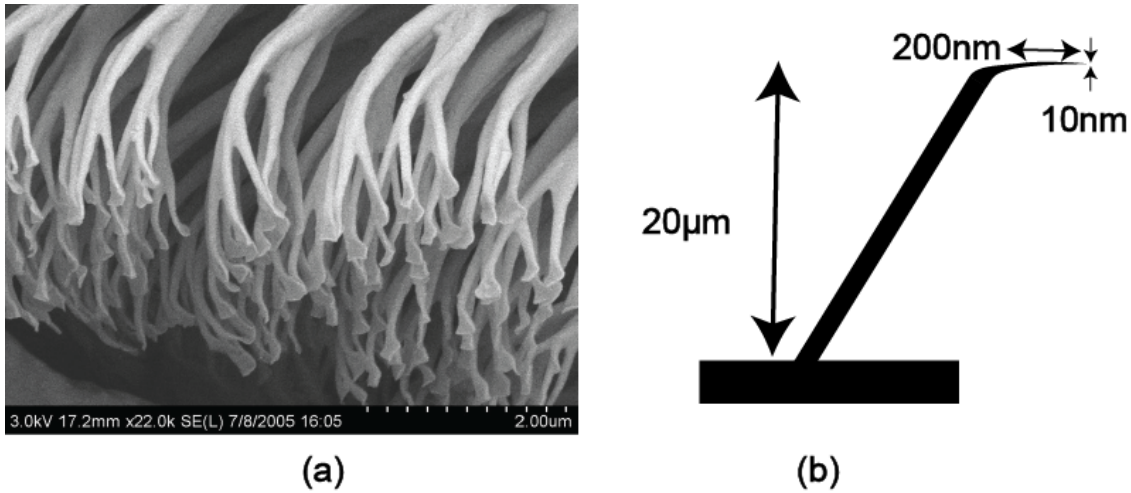


Figure 4.7: (a) Example image of spatula on *gecko gekko* (Image courtesy of Kellar Autumn) (b) Ideal angled fiber and terminal spatula plate geometry shown in various literature to be critical to high performance synthetic gecko adhesives [9].

$$\theta_{cr} = \cos^{-1} \left( 1 - \frac{P_o}{EH} + \sqrt{\left( \frac{P_o}{EH} \right)^2 + \frac{2\gamma}{EH}} \right) \quad (4.4)$$

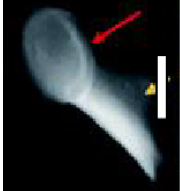
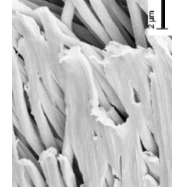
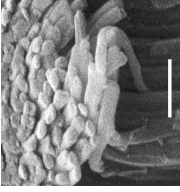
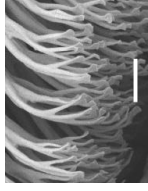
This critical angle is dependent on the generated pre-tension,  $P_o$ , Young's Modulus,  $E$ , surface energy,  $\gamma$ , and spatula thickness  $H$ . For the spatula to function in this manner, the spatula plate must be very thin ( $H = 5$  nm for Gao's model). The implication for synthetic gecko adhesives is clear: for strong and reversible adhesion, the terminal spatula plate must have thicknesses approaching 10 nm. This represents a significant manufacturing challenge that to date has not been achieved.

Despite recent advances in synthetic fibrillar fabrication techniques, to date, no synthetic fibrillar adhesive has been created with the same scale terminal plate features (Table 4.2). Attempts at fabricating similar structures have been made by several groups, and plate like structures have been shown to be superior to hemispherical shaped tips. Jeong and Suh [68] also showed a PUA fiber with a post-processed tip with 4 times higher adhesion than an unmodified counterpart. Xue and Gorb [138] also showed a similar 270 nm fiber with a flattened tip with similar results. However, none of these have approached the 10-20 nm thick terminal plate on a stiff 1-4 GPa fiber (necessary for overall compliance) shown by previous analysis [9] to be necessary for robust and reversible adhesion on rough surfaces (Fig. 4.7).

The proposed fabrication processes outlined in Figure 4.8 are based on abrading or plastically deforming partially fabricated features into the final desired shape, and are based on



Table 4.2: State of the art in spatula-like synthetic tip features. Scale bars:  $1\mu\text{m}$  for 1,2,4,5 and  $2\mu\text{m}$  for 3.

Group	Material	Feature Size	Young's Modulus	Technique	Group	Material	Feature Size	Young's Modulus	Technique	Image
Jeong and Suh, 2012	Polyurethane Acrylate	1100-1300 nm	1.3-1.6 GPa	Capillary UV molding and post tip deformation	Xue, Gorb, et al, 2012	Polystyrene	270nm	3 GPa	AAO molding and hot pressing	
Gillies and Fearing, 2011	Polyethylene	300 nm	1 GPa	Hot molding and shear deformation	Gillies and Fearing Group	Epoxy	150 nm	1 GPa	AAO molding and tip polishing	
										
										

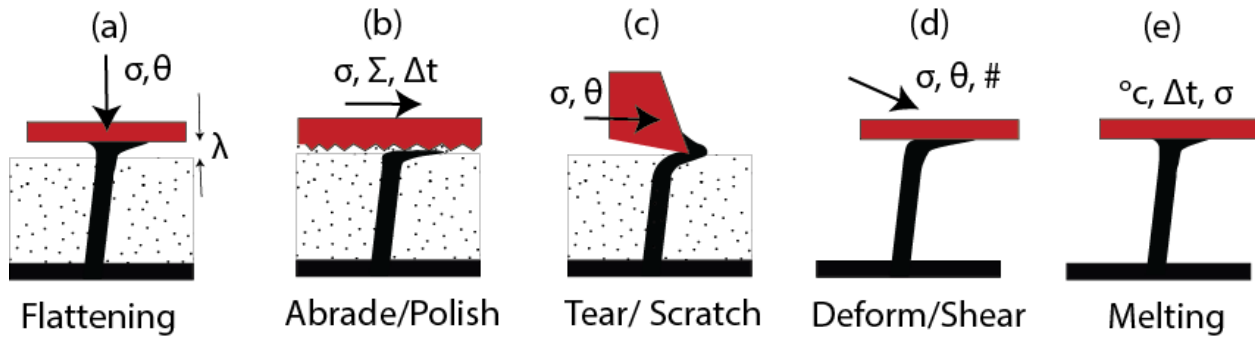


Figure 4.8: A variety of possible tip fabrication processes and parameters are presented for fibers still in a mold (a)-(c) and free standing (d)-(e). Spatula plates fabricated by: (a) flattening with a smooth tool with stress,  $\sigma$ , tip height,  $\lambda$ , and approach angle  $\theta$ . (b) Abrasion/polishing of the mold surface with stress,  $\sigma$ , surface roughness,  $\Sigma$ , and polishing time,  $\Delta t$ . (c) Tearing/scratching of fiber tips with a cutting tool with stress,  $\sigma$ , and approach angle  $\theta$ . (d) repeated cycles of shearing resulting in creep deformation with stress,  $\sigma$ , approach angle  $\theta$ , and number of cycles. (e) Hot melting of free standing fiber tips with temperature, time,  $\Delta t$ , and stress,  $\sigma$ .

the sub-100 nm thin-film features that were created on polymer microfibers above using a plastic creep-deformation process.

Based on preliminary results and on literature on nano-scale stiff polymer deformation, there are several promising fabrication pathways for realizing nano-scale spatular tips. The first three involve processes where the fiber is constrained by a mold or protective layer (Figure 4.8 (a-c)). This layer (dotted area) can either be the mold in which the fiber was formed, or added later through a dip or spin coating process (with similar techniques that have been developed in our lab for Germanium nanowires [78], as well as other groups with CNT [141]) followed by a timed etch process.

The first method involves epoxy in AAO templates and an abrading and polishing method in which both the mold and the fibers are polished via material removal by an abrasive counter surface (Figure 4.8b). Polishing on polyethylene surfaces has revealed that nano sized portions of material will plastically shift and deform with the polishing surface. Notably, Wong *et al.* [136] has shown nano-scale wall formation between intersecting lines during an abrasive scratch test, and described the process as a low-cycle localized fatigue.

The second method of tip deformation may be achieved by a shear and flattening process similar to the results seen above via creep deformation of the fibers above. Work by Xue and Gorb [138], has also shown that tip flattening is possible when fibers were exposed by removal of a cap layer on an AAO template, leaving 100 nm of the fibers exposed to the flattening tool. This work can be extended by optimizing fiber spacing, tip exposure length, pressure, and surface conditions in order to form the required 10-20 nm thick structures (Fig. 4.8a).

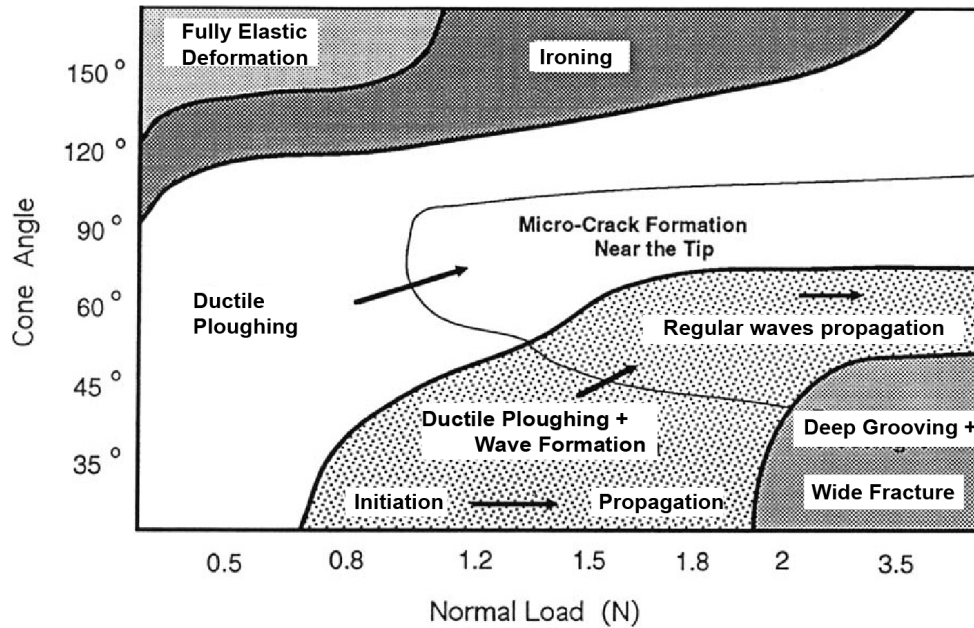


Figure 4.9: An example of a scratch map for PE (taken from [20]). The picture shows results from scratch tests performed at room temperature for a range of cone angles and normal loads and at a scratching velocity of 2.6 mm/s.

Although traditional cutting machining operations are not appropriate for nano-scale fabrication, recent work on the study of surface deformation by scratch indentation reveals that similar tensile deformation principles are at play. Work by Dasari [27] has shown that a number of modes of deformation are encountered during scratching. They include deformation bands, crazing, tearing, microcracking, regular cracking, and grooving. However they have found that crazing and tearing are the predominant modes of scratch deformation. As indicated by local strain rates, which are many orders of magnitude larger than the surrounding bulk material, it may be possible that when stiff thermoplastic fibers (made from materials like polyethylene and encased in a stiffer, rigid supporting material) may be deformed with a scratching or tearing process in order to reveal nano-sized spatula plates (Fig. 4.8). As well, a rich source of literature has been established describing scratching processes on stiff thermoplastic materials. In one instance, Briscoe *et al.* [20] reported results for the case of rigid conical indenters for various tip angles, bulk temperatures, scratch velocities, and applied normal loads (Fig. 4.9).

## Polishing of thermoset nano-fibers

Alternative materials to thermoplastic PP fibers are thermoset polymers such as polyimide (PI) or epoxy, which may better resist deformation due to stronger cross-linking. In this case, a regular ceramic template mold, such as AAO can be utilized by filling with the PI or epoxy material through capillary action. The AAO mold can then be partially etched, exposing the tips of the epoxy fibers that are partially cured. An adhesive block can be brought in contact with the top surface of the mold along with an adhesive slurry. A process similar to Chemical Mechanical Polishing (CMP) can be performed (Fig. 4.10) where the polishing process will plastically deform the exposed fiber tips into the desired position, where they will later be cross-linked, either by thermal or UV process. Material removal rates (MRR) for CMP processes have been described, and the relevant parameters identified as  $MRR = \rho_w N V ol_{removed}$ , where  $\rho_w$  is the density of wafer,  $N$  the number of active abrasives, and  $V ol_{removed}$  the volume of material removed by a single abrasive [34, 4]. The volume removed is dependent on pressure and velocity, and other important input parameters include the wafer hardness, pad hardness, pad roughness, abrasive size, and abrasive geometry. While the CMP process has been well described, adaptations need to be made because CMP is primarily used for planarizing hard/brittle materials, not for plastically shaping features in relatively soft polymers. However as shown above, results show promise for soft polymer nanodeformation [136].

Preliminary work in this area has shown some promising results, but significant challenges still exist. Figure 4.10 shows epoxy fibers formed by wetting in an AAO template, and sanded as outlined above (but not including pre-partially etching of the AAO template to expose the tips). The fiber tips exhibit some deformation, however this array is likely non-functional due to the observed self collapsing of the array. AAO templates generally have a density of pores the result in arrays that self-collapse due to self-adhesion [122]. One method to reduce the density of the array is to first seed the AAO template with an array of PS microspheres via a dip coating method [82]. The PS microspheres then effectively block some of the pores during filling with polymer reducing the density of the array, as seen in Figure 4.11. For full spatula tips to be formed with this method, further control over the processing steps will be required. As well, partial etching of the mold prior to the polishing step may allow the tips to more fully form into a spatula shape.

## Creep-trained spatulae on nano-fibers

Further controls to the creep training fabrication method reported in section 4.1 could be added. For example, by adding a protective coating to protect all but the tip of the nanofibers. The fabrication steps using the sacrificial coating method are shown in Fig. 4.12, using similar techniques that have been developed in our lab for Germanium nanowires [78], and in other groups used to coat CNT in PMMA [141]. After coating, a partial etch exposes the tips of the fibers, where the length exposed can be determined by a timed etch or an

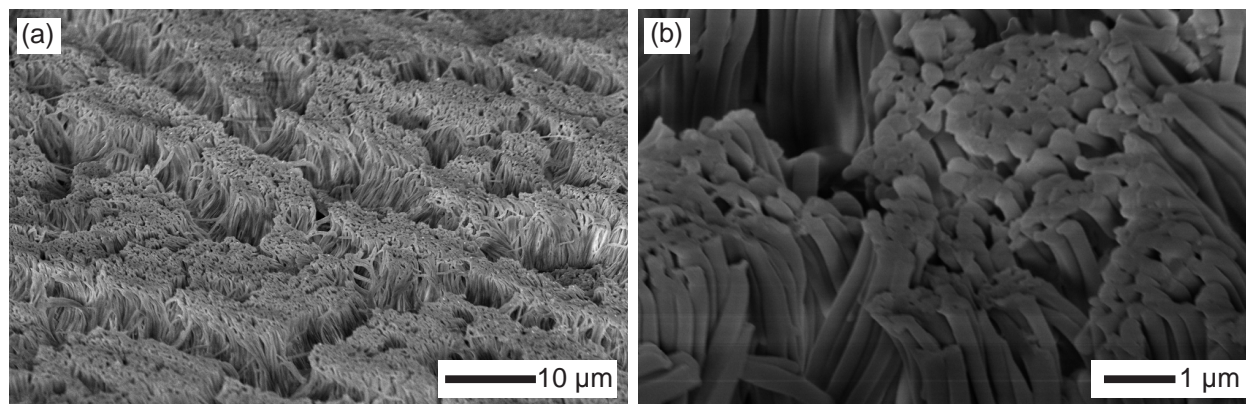


Figure 4.10: (a) Epoxy fibers fabricated via capillary wetting into an AAO template with 200 nm pores, then post processed with a sanding step. (b) Detail of the fiber tips showing slight deformation of the tips.

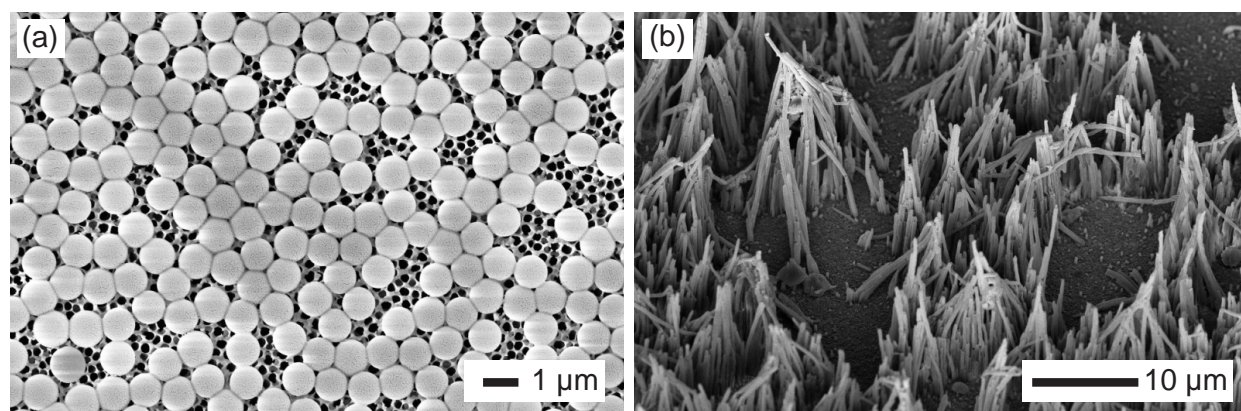


Figure 4.11: (a) An AAO template seeded with 900 nm PS microspheres before filling with polymer. (b) HDPE hairs with reduced density formed by heat molding in a PS seeded AAO template.

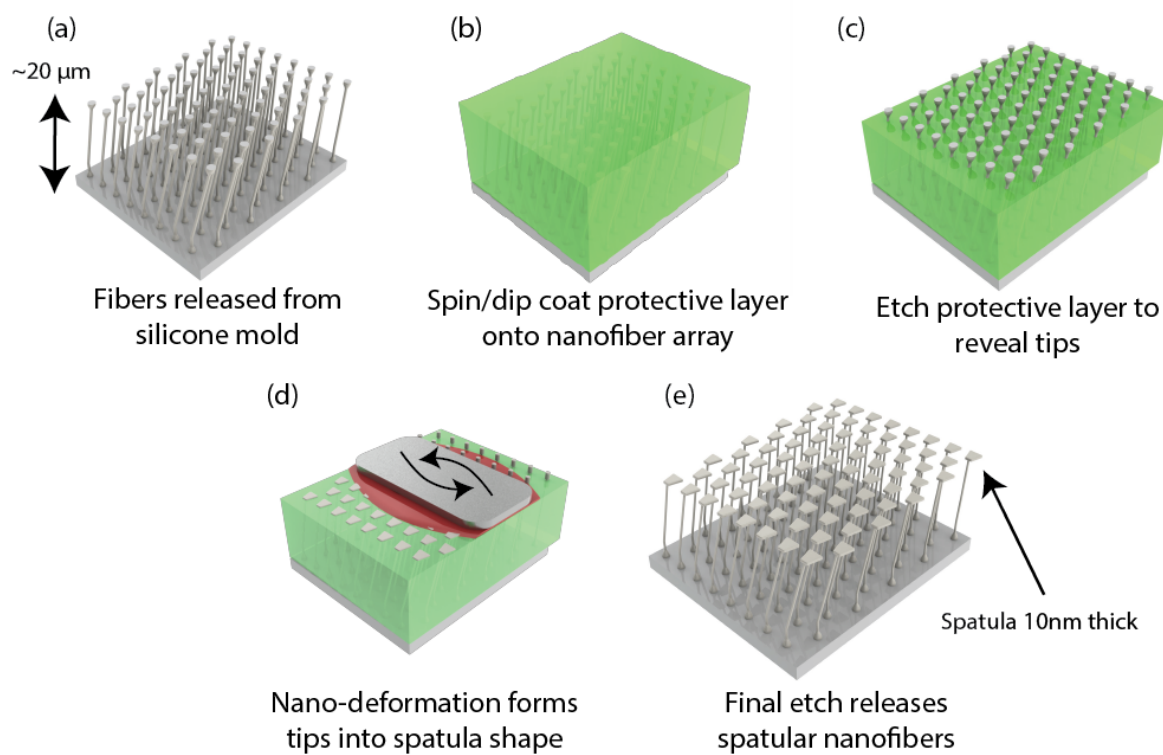


Figure 4.12: Proposed manufacturing process for fabrication of spatula plates. (a) Starting with fabricated stiff nanofiber arrays (b) Spin or dip coating to protect fibers during post processing (c) Partial etch of the protective coating to expose nanofiber tips (d) Post processing of tips by polishing or deformation (detail outlined in work plan) (e) Final etch release of fibers with spatula tips.

etch-stop layer. Using a plate or other dragging surface, the fiber tips will be plastically deformed. High friction due to fiber-surface adhesion leads to subsurface stresses beyond the plastic flow limit. Therefore, the upper layers of material, which adhere to the contacting surface, could slide along (float) in the direction of motion, after repeated passes of the working tool, a spatula-like tip emerges. In the final step, the sacrificial template can be removed, and further fiber deformation steps applied, such as angling fibers.

### 4.3 Concluding remarks

We conclude that a fundamental material limit has been reached for these fibrillated polymers, where the adhesive forces being generated with the counter surface are large enough to cause significant plastic deformation with the substrate during use. Thus, for repeated use applications on smooth substrates, the fiber adhesive is already limited by its material

strength, and improved adhesive strength would lead to earlier failure. A comparison can also be made to the natural gecko setae, which has been reported to last 30,000 cycles without any significant wear, and only a 5% decrease in shear adhesion [49]. This resistance to wear in the natural gecko setae may be attributed to the stability of the  $\beta$ -Keratin protein the fibers are made of, as well as uncorrelated nanoscale stick-slip events where contact spatular elements are either in static contact or in the process of slipping to a new static contact [49]. It is possible that future hard polymer GSAs fabricated from cross-linked materials, or with changed geometry that allows for nanoscale stick-slip events may avoid this failure mechanism due to the increased stability of cross-linked polymers and reduced sliding loads, respectively.

This creep-deformation phenomenon has been identified as a possible fabrication pathway that would allow for low cost and scalable nano-manufacturing of large arrays of spatulae-terminated nanofibrillar arrays. We have outlined several possible pathways and presented preliminary results which show promise for these techniques with further development. Emphasis is placed on moving to cross-linked polymer systems which better resist the creep deformation and wear mechanisms that arise from contact with the substrate.

## Chapter 5

# Adaptability of synthetic gecko arrays on rough surfaces

To better understand the role surface roughness plays in the adhesion of GSAs, a model is developed below that attempts to uncover the relationship between surface feature size and the adhesive terminal feature size, and also considers fiber stiffness, spacing and terminal feature shape. There are many examples in the literature of gecko fiber models that describe the adhesive properties of an individual fiber through varying fiber tip shape [125, 46, 24, 92], fiber dimensions [51], or robustness to roughness [62, 38], most of which model the fibers as elastic beams [102, 119, 91, 88]. There are fewer examples of models that describe how an array of fibers work together in concert to give rise to adhesive forces across the total array, which on rough surfaces will be different than just a sum of the adhesive forces generated by a single fiber [2, 61]. Some of these models consider several hierarchical levels [77, 14, 140, 23], and some consider shear on smooth or spherical indenters with a frictional adhesion cantilever or curved beam model [119, 139]. Another examines a logarithmic fit to experimental data to explain how the uncorrelated stick-slip behavior of fibers sliding on a surface gives rise to velocity dependence[49]. However, there have been no examples of models which include shearing of the array and attempt to capture the coupling between the shear adhesion and normal adhesion on rough surfaces across an array of fibers. The model below describes an approach which is designed to replicate the load-drag-pull style of GSA testing that is the common testing methodology throughout this body of work and is becoming widely adopted within the gecko adhesives community.

### 5.1 Fiber setup

As in many examples cited above, the fibers are modeled as spring elements approximated by a rotational spring at the base and a linear spring along the length of the fiber (Figure 5.1). These spring elements approximate the bending of the fiber by stiffness,  $K_t$ , and axial stiffness



of the fiber,  $K_a$ , which constitutes a pseudo-rigid body model of the fiber and simplifies the numerical calculation, as carried out by Schubert *et al.* and Tian *et al.* [119, 127]. Howell [57] describes that the bending of a thin elastic beam can be approximated for large deflections as a torsional spring with stiffness:

$$K_t = \pi\phi E_{fiber}I/L_o \quad (5.1)$$

Where  $\phi$  is a characteristic radius factor ( $\phi \approx 0.82$  for this case),  $E_{fiber}$  is the Young's modulus of the fiber material,  $L_o$  is the initial fiber length and  $I$  is the second moment of inertia of the fiber, which in the case of a circular fiber cross section is  $\pi r_f^4/4$  where  $r_f$  is the fiber radius. The axial stiffness of the fiber is:

$$K_a = \pi r_f^2 E_{fiber}/L_o \quad (5.2)$$

The assumption for both the axial stiffness and the bending stiffness is made that the change in fiber length does not significantly effect the stiffness of the structure. The fiber is prescribed an initial angle,  $\theta_{of}$ , and the current angle is calculated as  $\theta_{current} = \tan^{-1}((y_{tip} - y_{root})/(x_{tip} - x_{root}))$ . Forces acting on the fiber at the tip in the shear direction and normal direction are  $F_x$  and  $F_y$ , respectively. Forces are calculated by first determining the displacement of the fiber tip from its initial rest configuration, and then calculating the axial force  $F_A = K_a*(L_{current} - L_o)$  and the torsional force  $F_{tor} = K_t*(\theta_{current} - \theta_{of})/L_{current}$ . These are then used to calculate  $F_x$  and  $F_y$  via a transformation:

$$\begin{aligned} F_x &= F_A \cos(\theta_{current}) + F_{tor} \sin(\theta_{current}) \\ F_y &= F_A \sin(\theta_{current}) - F_{tor} \cos(\theta_{current}) \end{aligned} \quad (5.3)$$

The backing connecting the fibers is assumed to be rigid, and houses the fibers spaced at a constant pitch. The total shear and normal adhesive forces are taken as the sum of the individual fiber shear and normal forces.

For this particular execution of the simulation, dimensions and material properties of the fibers are chosen based on the stiff thermoplastic fibers published by the Fearing group [119, 83, 43] and outlined in Table 5.1. As well, a fiber height and angle variation are added via a random distribution to the array. Based on observation, a distribution of  $\pm 1.5 \mu m$  in length and  $\pm 5^\circ$  in angle are used. Furthermore, it is assumed that the fibers are sufficiently rigid and spaced so they do not collide or self adhere in order to simplify the calculations. Previous studies and observations have shown this to be a valid assumption [119].

## 5.2 Surface characterization and load-drag-pull path

For the model, two contact surface types are considered: a spherical probe with a radius of 2 cm and a sinusoidal surface with amplitude  $A$  and wavelength  $T$ . For each surface, the profile

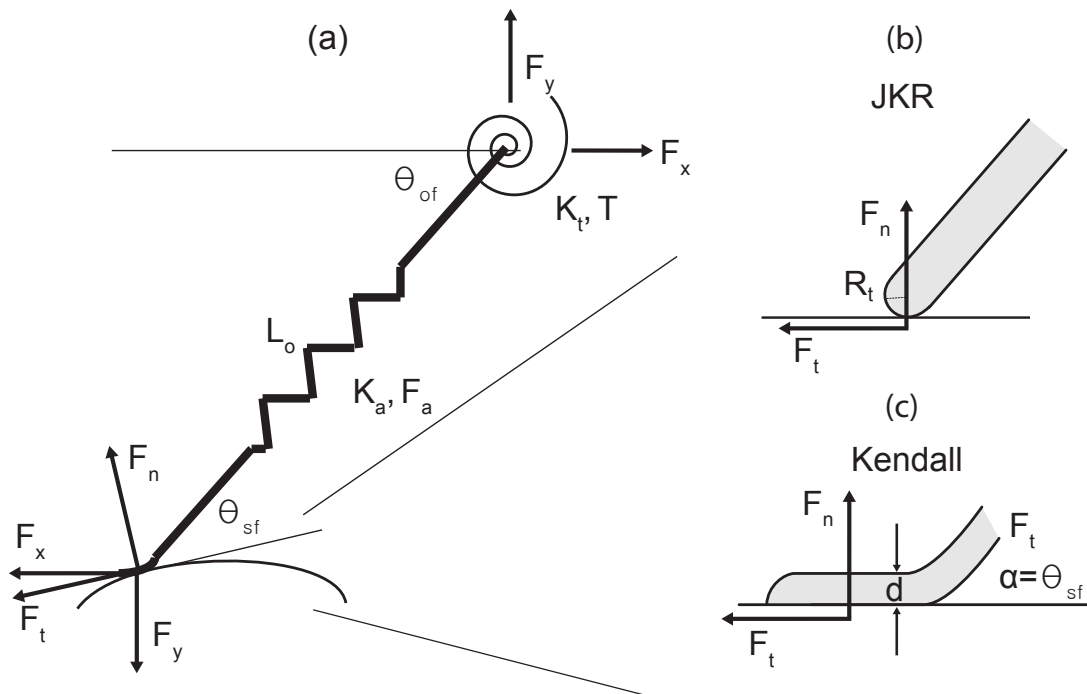


Figure 5.1: (a) Modeled approximation of the fiber and the relevant parameters indicated. The fiber is modeled with an axial spring and a torsional spring at its based that approximates fiber bending with a pseudo-rigid body model [57]. (b) Hemispherical tips approximated by the JKR contact model and (c) Spatula tips approximated by the Kendall peel model.

Table 5.1: Fiber properties used for simulation.

Property	Dimension
Young's Modulus	1 GPa
Fiber Radius	300 nm
Length	18.5 $\mu m$
Pitch	3 $\mu m$
Adhesion Energy	30 $mJm^{-2}$
Tip Radius	150 nm
Spatula Width	200 nm
Spatula Thickness	10 nm

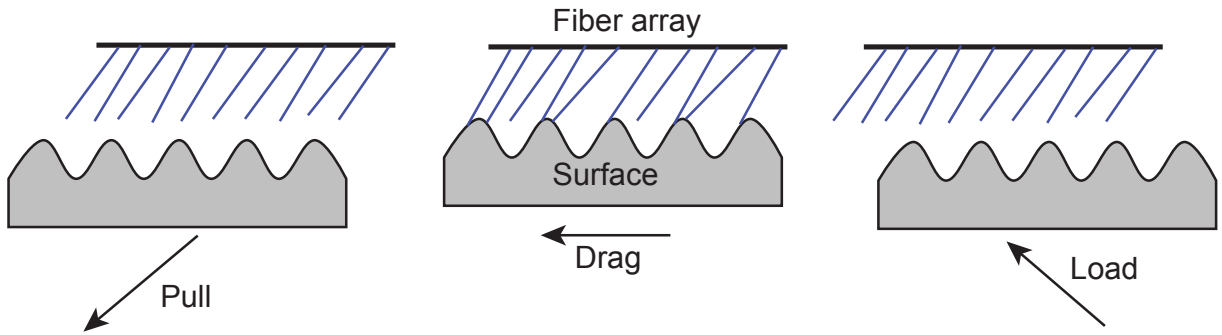


Figure 5.2: Illustration of the Load-Drag-Pull path.

is discretized into an array of  $x_{surface}$  and  $y_{surface}$  coordinates, with a spacing of  $e = 5 \times 10^{-9}$  m. The spherical indenter size is chosen so that at full indentation, a significant portion of the fibers make contact, as would be the case for a macroscopic adhesion measurement. For the sinusoidal surface, amplitudes and wavelengths are chosen to be on the same size order as the fiber length and spacing. Sinusoidal surfaces are chosen so that the effect of varying 'asperity' sizes can be studied in a systematic way by isolating feature sizes through amplitude and wavelength. This type of isolation would not be possible with a randomly generated rough surface.

Load-drag-pull path generation follows experimental methods outlined previously, and consists of three phases: a loading phase where the surface approaches the array on a fixed path at an angle of  $45^\circ$  to the surface, for a distance of  $25 \mu\text{m}$ . Immediately following loading, the surface is dragged parallel to the fiber array for a distance of  $10 \mu\text{m}$ , and finally during the unloading phase the surface moves away from the array at an angle of  $45^\circ$  for a distance of  $25 \mu\text{m}$  (Figure 5.2). For each load-drag-pull path, the surface indents into the fiber distance a fixed displacement,  $\Delta$ .

### 5.3 Fiber tip contact

To better understand the influence of tip geometry on the adhesion of an array of microfibers contacting a surface, we carry out the simulation using two contact models that represent the tip geometry of interest in each case; firstly we model the fiber tips as elastic hemispheres using the well-known Johnson-Kendall-Roberts (JKR) contact model, and secondly we model the fiber tips as plates (similar to the gecko's terminal spatula) that peel as a thin tape following the Kendall peel model.

### 5.3.1 JKR contact model

Fibers with hemispherical tips have been modeled using the JKR theory of contact adhesion and it has shown to be an effective tool for predicting adhesive forces between elastic bodies [119, 122, 51, 140, 10, 143]. Fabrication of stiff thermoplastic arrays of microfibers have been largely limited to hemispherical tipped fibers, therefore we use the JKR model to estimate the adhesive properties of this design. According to the JKR theory, an elastic sphere, when pressed against a rigid substrate with a force  $F_n$  will develop a true contact area with the surface governed by Equation 5.4 [69].

$$A_t(F_n) = \pi R_t \left\{ \frac{3(1-\nu^2)}{4E} \left( -F_n + 3\pi W_{ad} R_t + \sqrt{-6\pi F_n W_{ad} R_t + (3\pi W_{ad} R_t)^2} \right) \right\}^{2/3} \quad (5.4)$$

Where  $R_t$  is the tip radius,  $\nu$  is Poisson's ratio and  $W_{ad}$  is the work of adhesion (approximately  $30 \text{ mJm}^{-2}$  for a hard thermoplastic such as polypropylene on glass [47]). Equation 5.4 is linearized about  $F_n = 0$ , and the tangential force  $F_t$  is expressed as a function of the normal force as carried out by Schubert *et al.* [119] and Sitti and Fearing [122]:

$$\begin{aligned} F_t &= \pm \tau A_t(F_n) \\ &\approx \tau \left[ A_t(F_n = 0) + \frac{dA_t(F_n = 0)}{dF_n} F_n \right] \\ &\approx \mu (F_o + F_n) \end{aligned} \quad (5.5)$$

Where  $\tau$  is the interfacial shear strength,  $F_o = (9/2)\pi R_t W_{ad}$  is the assumed adhesive component of the contact and  $\mu = \tau(d/dF_n)A_t(F_n = 0) = 0.2$ . As the fiber reaches this  $F_t$  limit, we assume that the fiber remains in contact with the surface, but that the fiber slides in shear opposite to the direction of the shear force. In addition, a maximum pull-off force can be calculated, using the same sphere-on-flat assumption, and is given as  $F_{JKR} = (3/2)\pi R_t W_{ad}$  and represents the maximum normal load a fiber can sustain before detaching completely from the surface [69]. These equations constitute the adhesion limit for a hemispherical shape tip, beyond which the fiber will either slide or detach as discussed.

### 5.3.2 Kendall peel model

It has been hypothesized by many investigators studying the gecko adhesive system that the terminal spatula plates can be modeled as a continuum adhesive surface on a flexible strip that follows Kendall peeling mechanics and is governed by the peeling force [73]:

$$F = bdE \cos \left( \alpha - 1 + \sqrt{\cos^2 \alpha - 2 \cos \alpha + 1 + 2R/dE} \right) \quad (5.6)$$

where  $b$  is the width of the strip,  $d$  is the thickness of the strip,  $E$  is the Young's modulus of the strip material,  $R$  is the adhesion energy per area and  $\alpha = \theta_{sf}$  is the peel angle, which

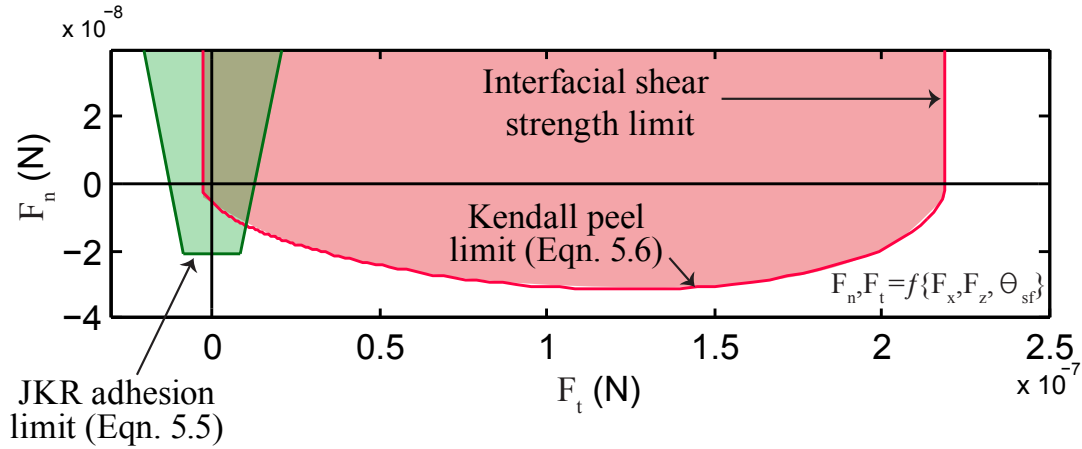


Figure 5.3: Adhesion limits for both the Johnson-Kendall-Roberts model as well as the Kendall peel model. A fiber undergoing axial strain and bending as outlined previously will fall within this force space as a function of the shear and normal load on the fiber,  $F_x$  and  $F_y$ , as well as the local surface angle,  $\theta_{sf}$ . Fibers will remain in contact as long as the forces are within the adhesion envelope. Fiber properties and dimensions are given in Table 5.1.

in this case is the angle between the fiber shaft and the surface; the difference between the current fiber angle and the local surface angle where the fiber is making contact,  $\theta_{sf} = \theta_{current} - \theta_{local}$ . Maximum and minimum peeling forces can be predicted at the limits of the peel angle, with the maximum peel force occurring at  $\alpha = 0^\circ$ , being  $F_{max} = \sqrt{2Rb^2dE}$ .

These equations constitute an adhesion limit beyond which the contacting terminal will either slide if normal forces are compressive or detach from the surface via peeling if normal forces are tensile. Although digital hyperextension exhibited by the gecko during detachment could be explained by detachment via a Kendall peel model, whole array forces do not represent Kendall peel behavior [5]. However, it is still unclear whether or not such a model applied to the individual elements would sum to the observed macroscopic behavior. The simulation attempts to predict the cumulative effect of an array of fibers each acting as independent Kendall peel fibers.

Adhesion limits are represented in Figure 5.3. A fiber undergoing axial strain and bending as outlined previously will fall within this force space as a function of the shear and normal load on the fiber,  $F_x$  and  $F_y$ , as well as the local surface angle,  $\theta_{sf}$ . Fibers will remain in contact as long as the forces are within the adhesion envelope.

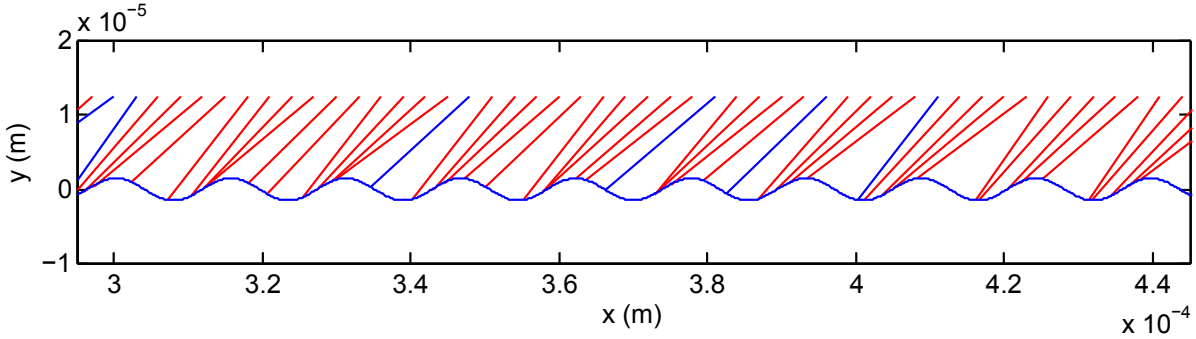


Figure 5.4: A snapshot of the simulation running on a sinusoidal surface. Fibers in red are in contact, fibers in blue are out of contact.

## 5.4 Numerical simulation

The numerical simulation runs as a displacement controlled system in which the surface is moved along the load-drag-pull path in increments of  $i = 10^{-8}$  m, in a quasi-static manner. As the system evolves, each fiber can switch between 5 possible contact modes: no contact (mode 0), stable tip contact (mode 1), sliding contact (mode 2), detaching contact (mode 3) and side contact (mode 4). A snapshot of the simulation being run on a sinusoidal surface is shown in Figure 5.4.

For a fiber in no contact (mode 0), at each step, it is possible for the fiber to switch into stable tip contact (mode 1), or side contact (mode 4). At each step, a contact detection algorithm is used to determine if each fiber is in contact. Contact can either occur along the length of the fiber (side contact) or at the tip. A linear approximation of the fiber between the fiber root and the fiber tip is used to determine if any portion of the surface interferes with the fiber through Equation 5.7.

$$\begin{aligned}
 a &= (y_{tips} - y_{roots}) / (x_{tips} - x_{roots}) \\
 b &= y_{tips} - a \cdot x_{tips} \\
 \delta &= (a \cdot x_{surface} + b) - y_{surface}
 \end{aligned} \tag{5.7}$$

The resulting array,  $\delta$ , is the vertical distance between the fiber and the surface at each point of the surface array  $x_{surface}$ . For the elements of  $\delta$ , tip contact occurs when the first element is found to be negative, and side contact occurs when elements between the second and last are found to be negative.

For a fiber in stable tip contact (mode 1), the fiber tip is stable in its adhered position on the surface at an index  $n$ , which identifies its location in space by the previously defined surface:  $x_{tip} = x_{surface}(n)$  and  $y_{tip} = y_{surface}(n)$ . The force on the base of each fiber is

then calculated as described in Equations 5.1 and 5.2 using the torsional stiffness,  $K_t$ , axial stiffness,  $K_a$ , and the transformation described in Equation 5.3. These forces are then used in conjunction with the adhesion limit models discussed in Sections 5.3.1 and 5.3.2 to determine whether the fiber will remain in stable tip contact (mode 1), or if it will cross the adhesion limit by sliding (mode 2) or detachment (mode 3). Furthermore, axial compressive loads are limited by Euler buckling, where  $F_{A_{max}} \leq \pi^2 EI / (kL)^2$ , where  $k$  is a characteristic factor determined by the beam boundary conditions, in this case assumed to be  $k = 0.69$  for a pinned-clamped beam. As well, contact detection is once again used to determine if the fiber will enter into side contact (mode 4).

For a fiber entering into sliding contact (mode 2), the fiber is assumed to remain in contact with the surface, and translate in the direction opposite of the shear force on the fiber,  $x_{tip} = x_{surface}(n - 1 \times \text{sign}(F_x))$  and  $y_{tip} = y_{surface}(n - 1 \times \text{sign}(F_x))$ , until a position is reached where the adhesion limit is no longer violated, or the fiber detaches (mode 3) or switches into side contact (mode 4).

For a fiber undergoing detachment (mode 3), the fiber is assumed to first retract from its extended position on the surface to a point in space defined by its current incline angle,  $\theta_{current}$ , by Equation 5.8.

$$\begin{aligned} x_{tip} &= x_{root} - \cos(\theta_{current})L_o \\ y_{tip} &= y_{root} - \sin(\theta_{current})L_o \end{aligned} \tag{5.8}$$

Once retracted, the fiber is assumed to immediately swing back to its initial angle  $\theta_{of}$ . As the fiber swings back to its initial angle, the contact detection algorithm is once again employed to determine whether the fiber will return to no contact (mode 0) at its initial rest configuration, or if there is an intermediate angle in which the fiber regains tip contact (mode 1), or side contact (mode 4).

During side contact (mode 4), the assumption is made that the bending forces at the tangential point of contact are exceptionally small compared to the adhesive and axial forces during contact, and are therefore neglected. The fiber will follow the surface making tangential contact until tip contact is regained (mode 1) or the surface pulls away and the fiber returns to its rest configuration (mode 0).

At the end of each path step  $i$ , the normal and shear forces from each fiber are summed to find the total array shear,  $F_{x\ total} = \sum F_x$ , and normal forces,  $F_{y\ total} = \sum F_y$ , at step  $i$ .

## 5.5 Comparison of JKR and Kendall peel contact models

The simulation was run for inclination angles,  $\theta_{of} = 35^\circ - 85^\circ$ , and indentation depths,  $\Delta = 2 - 5\mu\text{m}$  and with the fiber properties outlined in Table 5.1. Figure 5.5 shows two example load-drag-pull traces for  $\theta_{of} = 51^\circ$  and  $\Delta = 2\mu\text{m}$  in force space (a-c) and time

space (b-d). As can be seen in both traces, contact forces begin in compression as the fiber array is loaded, and then switch into tensile loading as the drag begins. Forces remain largely the same during the drag phase for both the spherical and spatula shaped tips. For the spatula tips (Figure 5.5a-b), there is greater variation in the force signal due to the uncorrelated detachment and re-attachment of the fibers as they peel and re-attach to the surface, and during unloading, the forces gradually decrease to zero as the fibers are pulled from the surface. The maximum tensile force occurs during the drag phase of the trace (green star). For the hemispherical shaped tips (Figure 5.5c-d), as the array is pulled from the surface the tensile force increases to its maximum (green star).

For the hemispherical tips using the JKR contact model, we wish to compare the effect of fiber angle inclination and indenter depth on adhesive forces of the system. Two measures of interest are the mean force during the drag phase, which corresponds to the force one would expect to see if dragging the array in shear on a surface (a common use scenario), and the maximum tensile load of the traces, indicating the maximal performance of the array. Figure 5.6 shows the maximum (a) and mean (b) forces on the array for the parameters tested. Maximum tensile forces are plotted as absolute values, mean forces are plotted as tensile being negative. Fiber inclination angle  $\theta_{of}$  can be seen to have a large effect on both the maximum and mean tensile loads, with nearly vertical fibers showing the lowest tensile loads, confirming some experimental results [56]. Indentation depth only impacts the mean tensile forces, having little effect on the maximum tensile load. This confirms other studies that have pointed to zero pre-load being a feature of the fibrillar adhesive system [86]. However, indentation depth does have an effect on the mean forces during the drag. Only an indentation depth of  $\Delta = 2\mu\text{m}$  shows tensile loads during drag, an exhibition of the frictional adhesion effect common in fibrillar adhesives [5]. Beyond this, forces become monotonically more compressive with indentation depth, and as well friction forces increase.

For the spatula shaped tips using the Kendall peel model, plot the forces using the same parameters as above. Figure 5.6 shows the maximum (a) and mean (b) forces on the array. For both the mean and maximum normal forces, indentation depth is not a significant factor, however, there is an increasing shear load with increasing indentation depth, likely because at a higher indentation depth, fibers become more inclined and this reduces the peel angle. Initial fiber angle has less of an effect on the maximal normal adhesion, however for mean adhesion, forces become compressive at angles near vertical as with the JKR modeled fibers. For fibers inclined above  $60^\circ$ , forces go from tensile during the drag to compressive.

We can directly compare the hemispherical tips to the spatula tips by selecting a subset of the data above and plotting together for direct comparison. Figure 5.8 shows (a) maximal, and (b) mean forces at an indentation depth of  $\Delta = 3\mu\text{m}$ . For the maximal forces, the spatula tipped fibers show more than 2.5 times the adhesion across all fiber angles, and about 5 times the shear, with the largest difference being for nearly vertical fibers. For mean forces during drag, the spatula tips show tensile normal forces, whereas the hemispherical tips remain compressive. Spatula tipped fibers also show much larger shear loads during the drag for lower angled fibers. However for fibers near vertical, both contact models result in



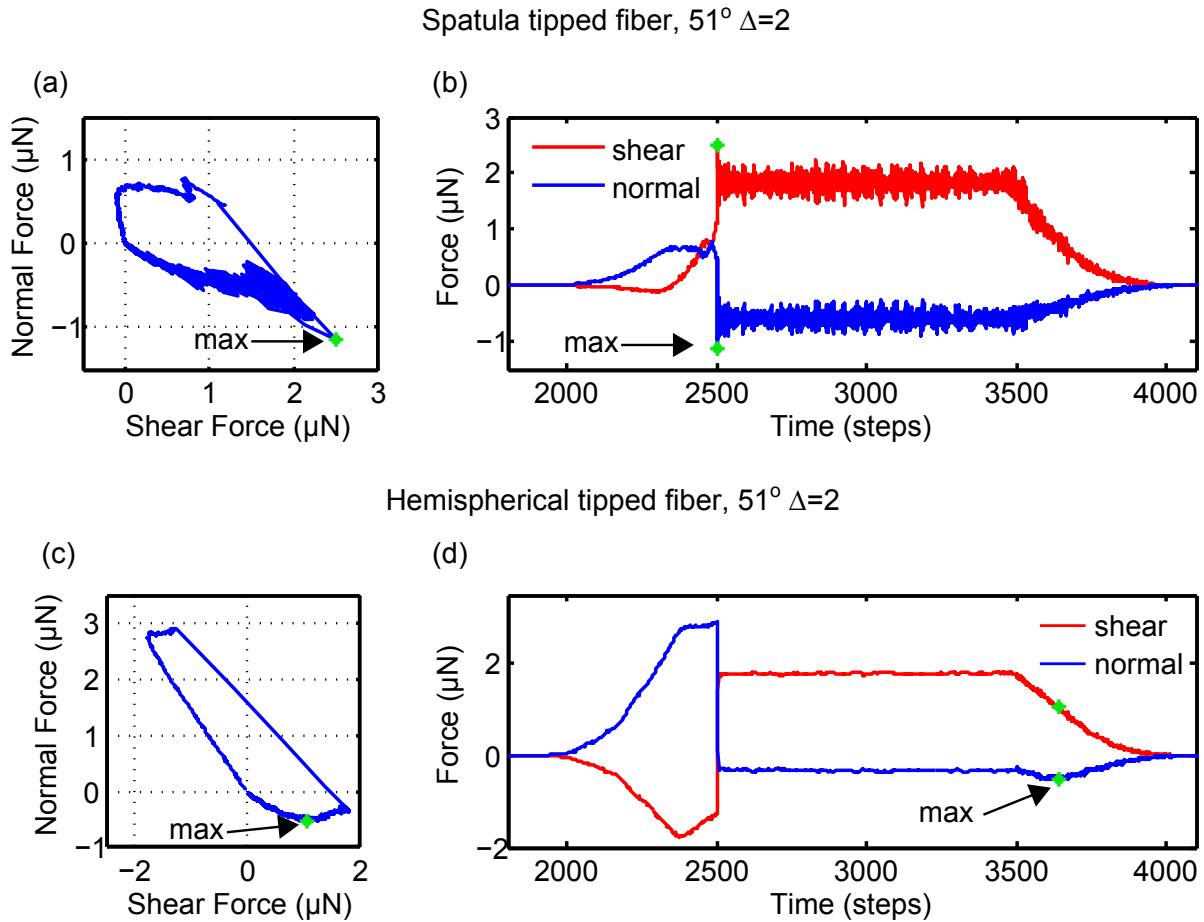


Figure 5.5: Example Load-Drag-Pull simulation results for 250 hemispherical tipped fibers using spatula tips with Kendall peel theory plotted in (a) force and (b) time space, and JKR contact theory in (a) force and (b) time space. The green star indicates the point of maximum tensile load on the array and the corresponding shear load. Each simulation was run on a spherical surface with a radius of 2 cm, an indentation depth of  $2 \mu\text{m}$  and an initial fiber inclination of 51 degrees.

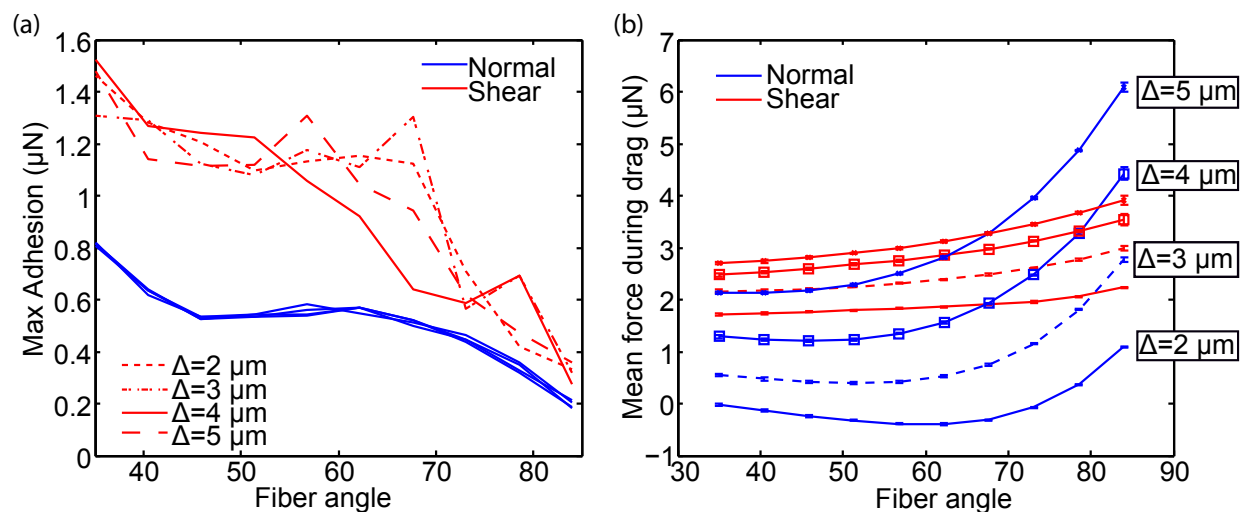


Figure 5.6: (a) Maximum adhesion forces and (b) mean forces during drag for an array of 250 fibers with hemispherical tips modeled with JKR theory for surface indentation depths of 2-5  $\mu\text{m}$ . Maximum tensile forces are plotted as absolute values, mean forces are plotted as tensile being negative.

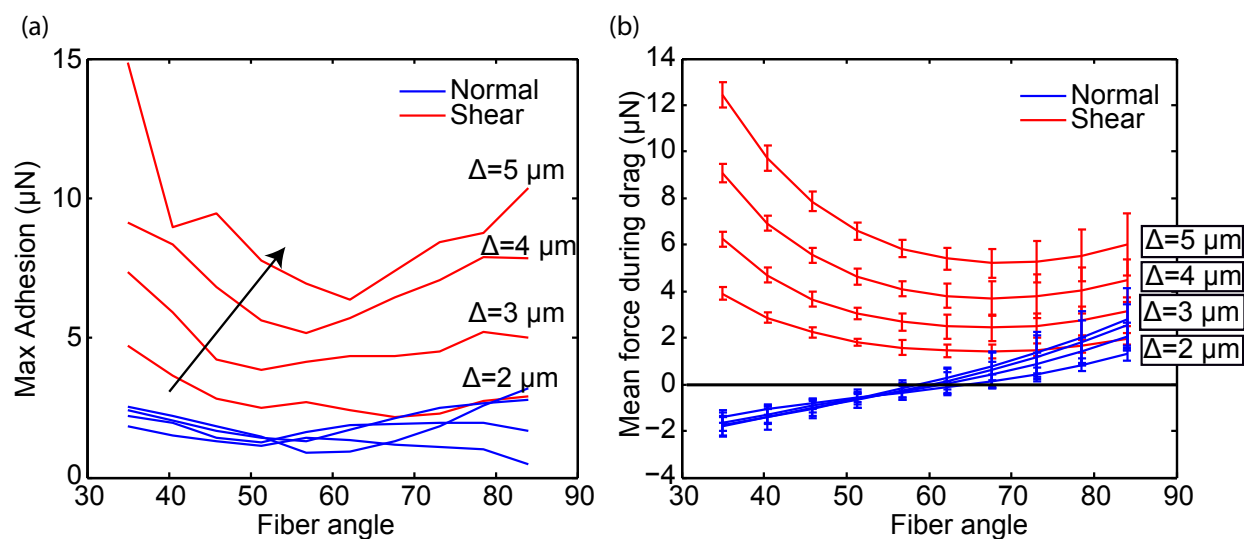


Figure 5.7: (a) Maximum adhesion forces and (b) mean forces during drag for an array of 250 fibers with spatula terminated tips for surface indentation depths of 2-5  $\mu\text{m}$ . Maximum tensile forces are plotted as absolute values, mean forces are plotted as tensile being negative.

fibers that give compressive loads during the drag. Figure 5.8 (c) shows the maximum point of detachment in force space and the  $\alpha$  angle for the JKR and Kendall cases, which represent the maximal force angle at detachment. Hemispherical tipped fibers show a maximal  $\alpha$  of  $25^\circ$ - $37^\circ$ , whereas spatula tipped fibers have an  $\alpha$  of  $15^\circ$ - $25^\circ$ . Both these values are approximately the same as the  $25^\circ$  reported for natural isolated gecko arrays [5]. The plot also shows the much larger magnitude of the maximal pulloff force of the spatula tipped Kendall peel model fibers.

Clearly the analysis above indicates that on smooth surfaces there is a distinct advantage to spatula terminated fibers in an array. As well, the model shows for the first time that the simple JKR and Kendall contact models, when applied to an array of angled fibers, show very similar behavior to experimental results on isolated gecko arrays [5] and synthetic fibrillar arrays [119]. The cumulative effect of individual fibers acting as Kendall peel exhibit behavior similar to the phenomenological frictional adhesion model presented by Kellar *et al.* [5].

## 5.6 Arrays on sinusoidal surfaces

The simulation was run on sinusoidal surfaces of varying amplitudes of 1 to 5  $\mu\text{m}$  and wavelengths 1-30  $\mu\text{m}$ , where  $y_{surface} = \frac{A}{2} \sin\left(\frac{2\pi}{T} x_{surface}\right)$ . Figure 5.9 shows simulation results for mean forces during drag and maximal adhesion during the trial. As anticipated, at the roughest of surfaces (  $A = 1 \mu\text{m}$ ,  $T=1 \mu\text{m}$ ), force drop to near zero, and grow as the wavelength is increased. Above wavelengths of  $\approx 20 \mu\text{m}$ , forces taper as the surface is nearly smooth at this point. Mean forces during drag were compressive for all surfaces tested, and show that the JKR model does not result in frictional adhesion on the sinusoidal surfaces tested. Interestingly, maximum adhesion shows a peak on rougher surfaces. This could be due to the local angle of contact, where fibers may actually show a greater resultant force at the surface due to the favorable angling of the surface. As amplitudes increase, forces begin to fall as the amplitude is large enough to push a significant number of fibers out of contact. For larger wavelengths, the amplitudes begin to converge.

The same surfaces were used to test spatula-tipped Kendall peel model fibers, and a comparison of the Kendall and JKR contact is made in Figure 5.10. Spatula tipped fibers show much larger forces for both mean adhesion and maximal adhesion, being almost 10 times larger for maximum adhesion. As well, mean forces become tensile during the drag phase, and for some amplitudes show larger tensile forces than for the same fiber array on a smooth surface (marked with star for Kendall and circle for JKR). Interestingly each amplitude shows a large spike in adhesion at smaller wavelengths. This could be again due to local surface angle reducing the effective peel angle of the fiber, and this has been pointed to experimentally that local orientation of the seta has a large impact on the adhesive forces [56]. As the surface amplitude increases, so does the wavelength at which this spike in adhesion occurs. As the wavelength of the surface increases, forces converge to the adhesion found on

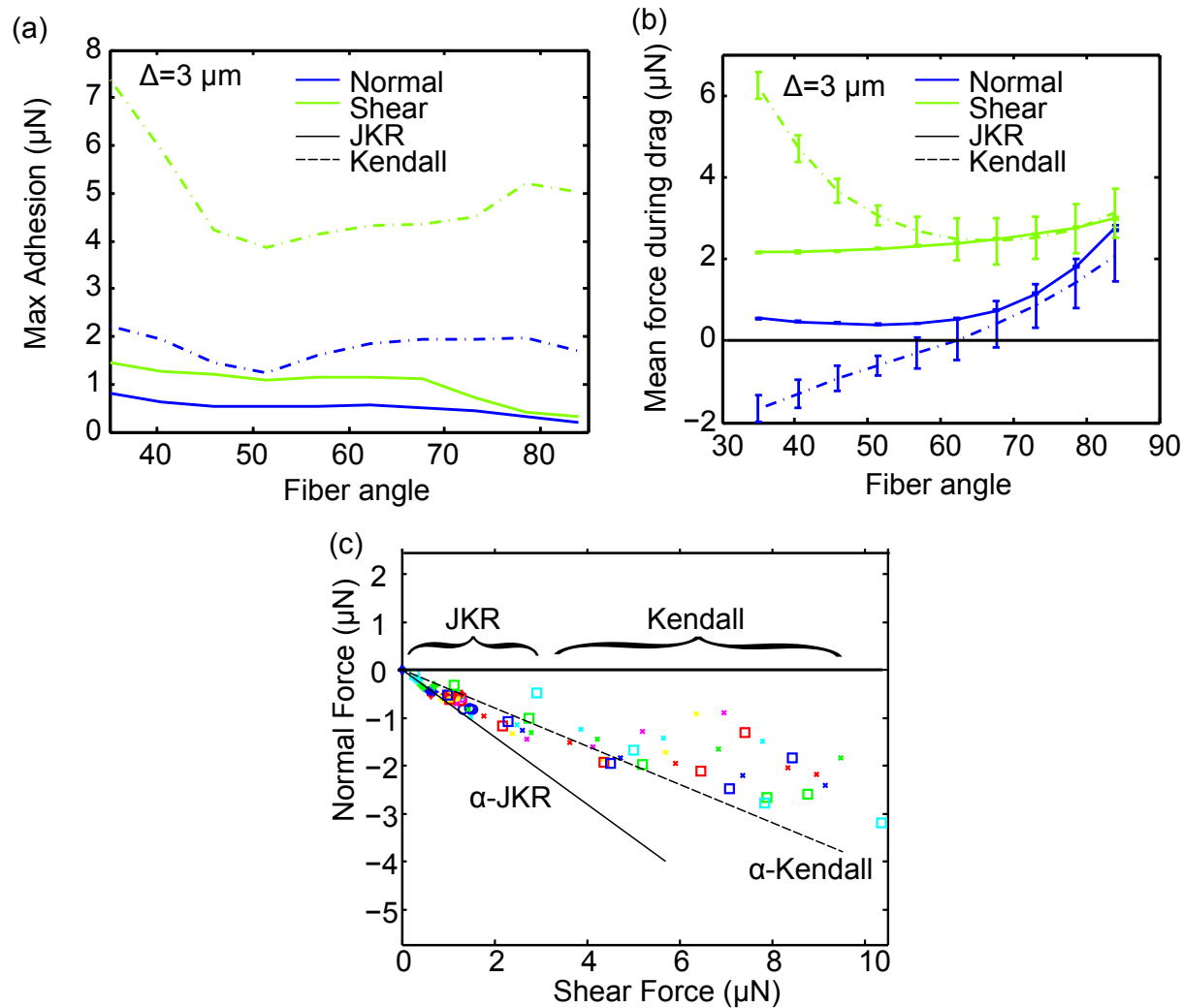


Figure 5.8: A comparison of the hemispherical tip JKR model fibers and the spatula tip Kendall model fibers for  $\Delta = 3 \mu\text{m}$  indentation on a spherical surface of 2 cm radius for (a) absolute maximum force, (b) mean force during drag and (c) maximum pulloff in force space.

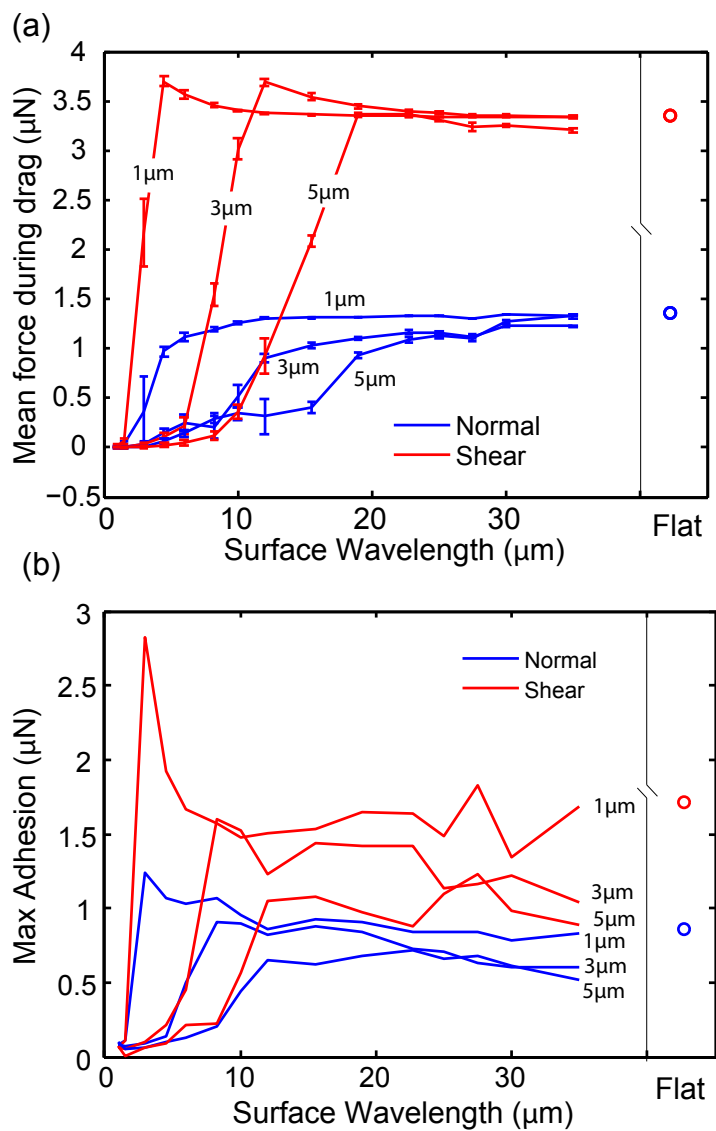


Figure 5.9: Simulation of 250 hemispherical JKR array of fibers on sinusoidal surfaces of amplitudes 1 to 5  $\mu\text{m}$  and wavelengths 1-30  $\mu\text{m}$  showing (a) mean normal and shear force during drag and (b) absolute maximal adhesion (tensile) during the trial. Fibers have an initial angle of  $60^\circ$ .

a flat surface.

## 5.7 Discussion of the results

Although many studies have clearly shown the benefit of a spatula shaped for adhesion on surfaces with roughness on the same size order as the spatula itself, this study is the first to show the efficacy of spatula tips compared directly to hemispherical tips with the same fiber geometry on an array of fibers on both smooth and sinusoidal surfaces. It appears that spatula tips modeled using the Kendall peel equation, when acting in concert through an array of fibers, show the frictional adhesion effect previously described in the literature [5], and have much larger adhesive forces than hemispherical tipped fibers. Furthermore, spatula tips show a large benefit in adhesion on sinusoidal surfaces with roughness on the size order of the fiber itself, and in some cases, sinusoidal surfaces allow for higher adhesion than on a smooth surface, likely due to local peel angles being smaller due to the slope of the surface.

Important to note is that the spatula tipped fibers are able to generate tensile loads during the drag phase of the cycle. This is in contrast to the compressive loads seen in the hemispherical tipped fibers, and could explain a self-engaging property by which fibers are able to pull more of the array in contact - an effect seen with spatula shaped natural gecko arrays, but not seen for arrays of synthetic fibers with hemispherical shaped tips. The analysis shows that even a single hierarchical level array of fibers could also show this effect on rough surfaces if spatula tips were a feature.

## 5.8 Concluding remarks

We sought to understand the impact of surface roughness on the adhesion of two types of GSA arrays: those with hemispherical-shaped tips and those with spatula-shaped tips. Our simulations showed that the nanoscale geometry of the tip shape alters the macroscale adhesion of the array of fibers by nearly an order of magnitude, and that on sinusoidal surfaces with roughness much larger than the nanoscale features, there is still a clear benefit to having spatula shaped features. Interestingly, the action of the fibers acting in concert shows behavior much more complex than what could be predicted with the pull-off model of a single fiber, and that both the JKR and Kendall peel models can explain the frictional adhesion effect previously described in the literature [5]. Similar to experimental results found with the macroscale features of the gecko adhesive system, when roughness approaches the size and spacing of the fiber features, adhesion drops dramatically.

This has clear implications for the design of future GSAs that may be used in environments with varying rough surfaces. It is clear that an integrated approach must be taken that considers the relationship between the surface roughness, the size of the adhesive structures, and their ability to conform at a variety of length scales. Understanding the abilities and

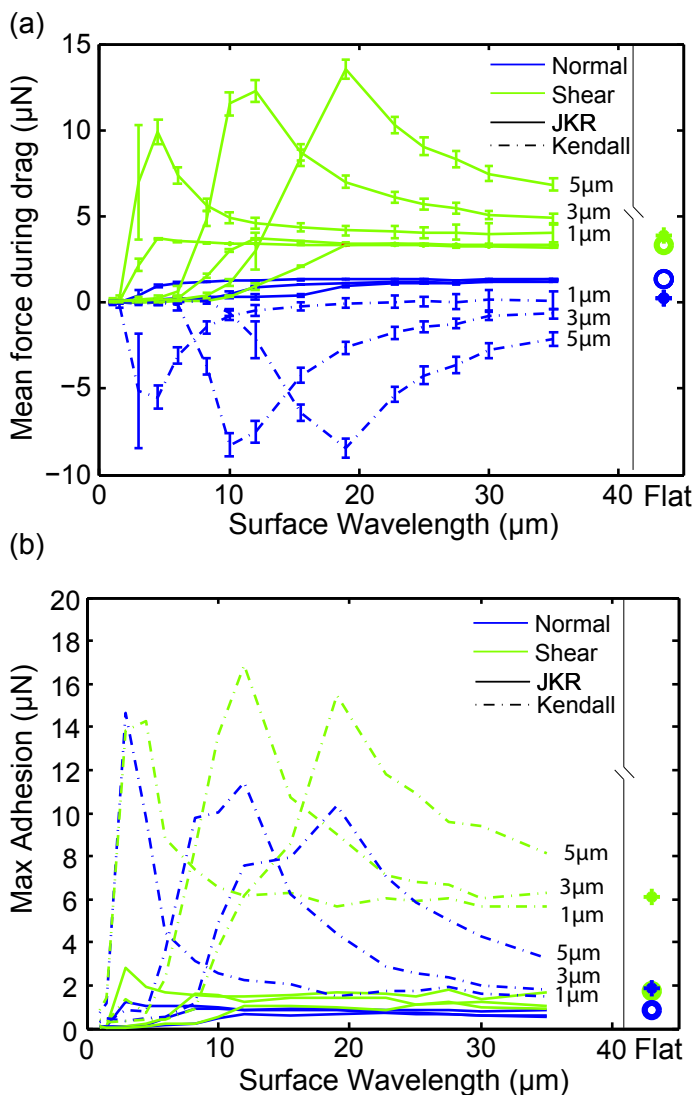


Figure 5.10: A comparison of the hemispherical tip JKR model fibers and the spatula tip Kendall peel model fibers for sinusoidal surfaces of amplitudes 1 to 5  $\mu\text{m}$  and wavelengths 1-30  $\mu\text{m}$  showing (a) mean normal and shear force during drag and (b) absolute maximal adhesion (tensile) during the trial. Fibers have an initial angle of  $60^\circ$ . Adhesive properties of the arrays on a flat surface are marked with star for Kendall and circle for JKR on the far right of the plot.

limitations of these structures on varying length scales of roughness is necessary to create an adhesive that is able to adhere to naturally rough surfaces.



## Chapter 6

# Conclusion

There still remains a gap between the capabilities of current GSAs, and the properties required for GSAs to perform as the gecko does: on natural undulating surfaces with several scales of roughness, in dirty environments where particle contamination is the norm, and for thousands or even tens of thousands of cycles. For continued progress to be made in GSAs, focus must shift from trying to attain high adhesive values under ideal conditions, to exploring the weaknesses in current GSAs and contrasting those with the principles that underpin the success of the natural gecko systems in real world challenging conditions. The body of this work focused on these issues, specifically on adhesion with rough surfaces, contaminating particles and wear mechanisms.

Lessons still continue to be learned from the gecko adhesive system, and work in Chapter 2 presented results on the geckos amazing ability to maintain adhesion on even very rough surfaces, and that the toes are capable of adhering to surfaces with amplitudes much larger than their dimensions even without engaging claws, maintaining 60% of shear adhesion on surfaces with amplitudes of 3 mm. However, there is a limit to the roughness that even the gecko can adhere to, and experimental data as well as a model developed in Chapter 2 showed that the ratio of adhesive feature size to surface feature size must be carefully considered in the design of the adhesive.

Similarly, dry-self cleaning capabilities must also be taken into consideration when making material and geometry choices for the GSA. Chapter 3 outlines results showing that a GSA made from a hard thermoplastic with nanoscopic fibers was able to recover 96-115% of its shear adhesion after fouling with small and large but not medium particles, while a GSA made from a soft polymer and microscopic fibers recovered 40-55% on medium and large particles. Further examination by SEM revealed that the PDMS structures were not shedding the smaller particles during recovery steps, but were instead being absorbed into the surface, and that, regardless of their size, particles did not release from the PDMS surface. We therefore concluded that dry self-cleaning will be more effective for GSAs fabricated with smaller fiber diameters and for GSAs fabricated from materials with smaller loss functions, such as hard thermoplastics. Although current soft polymer GSA systems show larger adhesive forces

than hard polymer GSAs, the expected use environment must be carefully considered for risk of contaminating the GSA irreversibly. To overcome this, it may be possible to add active control to the fibers for the purposes of shedding particles. We presented a prototype GSA capable of controlling adhesion to glass spheres 500  $\mu\text{m}$  to 1 mm, which represents an important step in realizing an adhesive with dry self-cleaning capabilities across a wide range of particle sizes.

Furthermore, we have outlined a failure mechanism rooted in the continued cycling of hard polymer GSAs and presented the results in Chapter 4. It appears a fundamental material limit has been reached for these fiber arrays, and that future gecko synthetic adhesive designs must take into account the high adhesive forces generated to avoid damage. Although the synthetic material and natural gecko arrays have a similar elastic modulus, the synthetic material does not show the same wear-free dynamic friction as the gecko.

Moving forward, the field of synthetic gecko adhesives still has challenges to overcome in order to achieve the same versatility and performance of its natural counterpart. Specifically, efforts should focus on the continuing development of nanoscopic spatula tips made from cross-linked stiff polymers to allow for greater nanoscale adhesion and dry-self cleaning, as well as integration with larger-scale soft hierarchical features that will allow for surface conformation across a wider range of surface feature roughness.

# Bibliography

- [1] R Adhikari, A Sarkar, and A K Das. A versatile cantilever beam magnetometer for *ex situ* characterization of magnetic materials. *The Review of Scientific Instruments*, 83(1):013903, January 2012.
- [2] B Aksak, M P Murphy, and M Sitti. Adhesion of biologically inspired vertical and angled polymer microfiber arrays. *Langmuir*, 23(6):3322–32, March 2007.
- [3] B Aksak, M P Murphy, and M Sitti. Gecko inspired micro-fibrillar adhesives for wall climbing robots on micro/nanoscale rough surfaces. *IEEE International Conference on Robotics and Automation*, pages 3058–3063, 2008.
- [4] D C Arnold, A Blake, J Quinn, D Iacopino, J M Tobin, C O’Mahony, J D Holmes, and M A Morris. Planarized and nanopatterned mesoporous silica thin films by chemical-mechanical polishing of gap-filled topographically patterned substrates. *IEEE Transactions on Nanotechnology*, 10(3):451–461, May 2011.
- [5] K Autumn, A Dittmore, D Santos, M Spenko, and M Cutkosky. Frictional adhesion: a new angle on gecko attachment. *The Journal of Experimental Biology*, 209(18):3569–79, September 2006.
- [6] K Autumn and N Gravish. Gecko adhesion: evolutionary nanotechnology. *Philosophical transactions. Series A, Mathematical, Physical, and Engineering Sciences*, 366(1870):1575–90, May 2008.
- [7] K Autumn, S T Hsieh, D M Dudek, J Chen, C Chitaphan, and R J Full. Dynamics of geckos running vertically. *The Journal of Experimental Biology*, 209(2):260–72, January 2006.
- [8] K Autumn, Y A Liang, S T Hsieh, W Zesch, W P Chan, T W Kenny, R Fearing, and R J Full. Adhesive force of a single gecko foot-hair. *Nature*, 405(6787):681–5, June 2000.
- [9] K Autumn, C Majidi, R E Groff, A Dittmore, and R S Fearing. Effective elastic modulus of isolated gecko setal arrays. *The Journal of Experimental Biology*, 209(18):3558–3568, September 2006.

- [10] K Autumn, M Sitti, Y A Liang, A M Peattie, W R Hansen, S Sponberg, T W Kenny, R S Fearing, J Israelachvili, and R J Full. Evidence for van der Waals adhesion in gecko setae. *Proceedings of the National Academy of Sciences*, 99(19):12252–6, September 2002.
- [11] W Barthlott and C Neinhuis. Purity of the sacred lotus, or escape from contamination in biological surfaces. *Planta*, 202(1):1–8, April 1997.
- [12] J Belardi, N Schorr, O Prucker, and J Rühle. Artificial cilia: generation of magnetic actuators in microfluidic systems. *Advanced Functional Materials*, 21(17):3314–3320, September 2011.
- [13] B Bhushan. *Introduction to tribology*. John Wiley & Sons, 2002.
- [14] B Bhushan. Adhesion of multi-level hierarchical attachment systems in gecko feet. *Journal of Adhesion Science and Technology*, 21(12):1213–1258, October 2007.
- [15] B Bhushan, B Galasso, C Bignardi, C V Nguyen, L Dai, and L Qu. Adhesion, friction and wear on the nanoscale of MWNT tips and SWNT and MWNT arrays. *Nanotechnology*, 19(12):125702, March 2008.
- [16] P Birkmeyer, A G Gillies, and R S Fearing. Dynamic climbing of near-vertical smooth surfaces. In *IEEE Intelligent Robots and Systems*, pages 286–292. IEEE, October 2012.
- [17] J Black and G Hastings. *Handbook of biomaterial properties*. Springer, 1998.
- [18] N Bloch and D J Irschick. Toe-clipping dramatically reduces clinging performance in a pad-bearing lizard. *Society for the Study of Amphibians and Reptiles*, 39(2):288–293, 2005.
- [19] R A Bowling. *Particles on surface 1: detection, adhesion and removal*. Plenum. Press, New York, 1988.
- [20] B J Briscoe, P D Evans, E Pellilo, and S K Sinha. Scratching maps for polymers. *Wear*, 200(1):137–147, 1996.
- [21] Carlson J D and Jolly M R. MR fluid, foam and elastomer devices. *Mechatronics*, 10(4):15, 2000.
- [22] R W Carpick, M Enachescu, D F Ogletree, and M Salmeron. Making, breaking, and sliding of nanometer-scale contacts. *Materials Research Society Symposium Proceedings*, 539:93–103, 1999.
- [23] B Chen, P D Wu, and H Gao. Hierarchical modelling of attachment and detachment mechanisms of gecko toe adhesion. *Proceedings of the Royal Society A: Mathematical, Physical and Engineering Sciences*, 464(2094):1639–1652, June 2008.

- [24] Q H Cheng, B Chen, H J Gao, and Y W Zhang. Sliding-induced non-uniform pre-tension governs robust and reversible adhesion: a revisit of adhesion mechanisms of geckos. *Journal of the Royal Society, Interface*, 9(67):283–91, February 2012.
- [25] J M Crissman and L J Zapas. Creep failure and fracture of polyethylene in uniaxial extension. *Polymer Engineering and Science*, 19(2):99–103, February 1979.
- [26] C A Dahlquist. Pressure-sensitive adhesives. In *Treatise on Adhesion and Adhesives*, 1969.
- [27] A Dasari, S J Duncan, and R D K Misra. Micro- and nano-scale deformation processes during scratch damage in high density polyethylene. *Materials Science and Technology*, 19(2):239–243, 2003.
- [28] J Davies, S Haq, T Hawke, and J P Sargent. A practical approach to the development of a synthetic Gecko tape. *International Journal of Adhesion and Adhesives*, 29(4):380–390, 2009.
- [29] P Day, E V Eason, N Esparza, D Christensen, and M Cutkosky. Micro-wedge machining for the manufacture of directional dry adhesives. *Journal of Micro and Nano-Manufacturing*, 1(1):1–10, 2013.
- [30] A del Campo, C Greiner, and E Arzt. Contact shape controls adhesion of bioinspired fibrillar surfaces. *Langmuir*, 23(20):10235–43, September 2007.
- [31] B V Derjaguin, V M Muller, and Y P Toporov. Effect of contact deformations on the adhesion of particles. *Journal of Colloid and Interface Science*, 53(2):314–326, November 1975.
- [32] A Desai, S W Lee, and Y C Tai. A MEMS electrostatic particle transportation system. *Sensors and Actuators A: Physical*, 73(1-2):37–44, March 1999.
- [33] R P Donovan. *Particle control for semiconductor manufacturing*. M. Dekker, 1990.
- [34] D A Dornfeld. Material removal mechanism in chemical mechanical polishing: theory and modeling. *IEEE Transactions on Semiconductor Manufacturing*, 14(2):112–133, May 2001.
- [35] G A Engh, K A Dwyer, and C K Hanes. Polyethylene wear of metal-backed tibial components in total and unicompartmental knee prostheses. *The Journal of Bone and Joint Surgery*, 74(1):9–17, January 1992.
- [36] B A Evans, A R Shields, R Ll Carroll, S Washburn, M R Falvo, and R Superfine. Magnetically actuated nanorod arrays as biomimetic cilia. *Nano letters*, 7(5):1428–34, May 2007.

- [37] A Freed. Viscoplasticity with creep and plasticity bounds. *International Journal of Plasticity*, 9(2):213–242, 1993.
- [38] H Gao, X Wang, H Yao, S Gorb, and E Arzt. Mechanics of hierarchical adhesion structures of geckos. *Mechanics of Materials*, 37(2-3):275–285, March 2005.
- [39] L Ge, S Sethi, L Ci, P M Ajayan, and A Dhinojwala. Carbon nanotube-based synthetic gecko tapes. *Proceedings of the National Academy of Sciences*, 104(26):10792–10795, June 2007.
- [40] A K Geim, S V Dubonos, I V Grigorieva, K S Novoselov, A A Zhukov, and S Y Shapoval. Microfabricated adhesive mimicking gecko foot-hair. *Nature Materials*, 2(7):461–3, July 2003.
- [41] A G Gillies and R S Fearing. Shear adhesion strength of thermoplastic gecko-inspired synthetic adhesive exceeds material limits. *Langmuir*, 27(18):11278–11281, August 2011.
- [42] A G Gillies, J Kwak, and R S Fearing. Controllable particle adhesion with a magnetically actuated synthetic gecko adhesive. *Advanced Functional Materials*, 23(26):3256–3261, 2013.
- [43] A G Gillies, J Puthoff, M J Cohen, K Autumn, and R S Fearing. Dry self-cleaning properties of hard and soft fibrillar structures. *Applied Materials & Interfaces*, 5(13):6081–8, July 2013.
- [44] N J Glassmaker, T Himeno, C Y Hui, and J Kim. Design of biomimetic fibrillar interfaces: 1. making contact. *Journal of the Royal Society, Interface*, 1(1):23–33, November 2004.
- [45] N J Glassmaker, A Jagota, CY Hui, W L Noderer, and M K Chaudhury. Biologically inspired crack trapping for enhanced adhesion. *Proceedings of the National Academy of Sciences*, 104(26):10786–91, June 2007.
- [46] S Gorb, M Varenberg, A Peressadko, and J Tuma. Biomimetic mushroom-shaped fibrillar adhesive microstructure. *Journal of The Royal Society Interface*, 4(13):271–275, 2007.
- [47] D H Gracias and G A Somorjai. Continuum force microscopy study of the elastic modulus, hardness and friction of polyethylene and polypropylene surfaces. *Macromolecules*, 31(4):1269–1276, February 1998.
- [48] N Gravish, M Wilkinson, and K Autumn. Frictional and elastic energy in gecko adhesive detachment. *Journal of the Royal Society, Interface*, 5(20):339–48, March 2008.

- [49] N Gravish, M Wilkinson, S Sponberg, A Parness, N Esparza, D Soto, T Yamaguchi, M Broide, M Cutkosky, C Creton, and K Autumn. Rate-dependent frictional adhesion in natural and synthetic gecko setae. *Journal of the Royal Society, Interface*, 7(43):259–269, February 2009.
- [50] C Greiner, A del Campo, and E Arzt. Adhesion of bioinspired micropatterned surfaces: effects of pillar radius, aspect ratio, and preload. *Langmuir*, 23(7):3495–502, March 2007.
- [51] C Greiner, R Spolenak, and E Arzt. Adhesion design maps for fibrillar adhesives: the effect of shape. *Acta Biomaterialia*, 5(2):597–606, February 2008.
- [52] A Haake and J Dual. Positioning of small particles by an ultrasound field excited by surface waves. *Ultrasonics*, 42(1-9):75–80, April 2004.
- [53] W R Hansen and K Autumn. Evidence for self-cleaning in gecko setae. *Proceedings of the National Academy of Sciences*, 102(2):385–389, January 2005.
- [54] E W Hawkes, E V Eason, A T Asbeck, and M R Cutkosky. The gecko’s toe: scaling directional adhesives for climbing applications. *IEEE Transactions on Mechatronics*, pages 1–9, 2012.
- [55] L Hecht. Particle adhesion to solid surfaces. *Journal of the Institute of Environmental Sciences & Technology*, 33:33–37, 1990.
- [56] G C Hill, D R Soto, A M Peattie, R J Full, and T W Kenny. Orientation angle and the adhesion of single gecko setae. *Journal of the Royal Society, Interface*, 8(60):926–33, July 2011.
- [57] L L Howell. *Compliant mechanisms*. John Wiley & Sons, Inc, New York, NY, 2001.
- [58] J Hrouz, V Vojta, and M Ilavský. Penetration behavior of the system sphere-cylinder. *Polymer Engineering and Science*, 20(6):402–405, April 1980.
- [59] S Hu, S Lopez, P H Niewiarowski, and Z Xia. Dynamic self-cleaning in gecko setae via digital hyperextension. *Journal of the Royal Society, Interface*, 9(76):2781–90, November 2012.
- [60] G Huber, S N Gorb, N Hosoda, R Spolenak, and E Arzt. Influence of surface roughness on gecko adhesion. *Acta Biomaterialia*, 3(4):607–10, July 2007.
- [61] C Y Hui, N J Glassmaker, and A Jagota. How compliance compensates for surface roughness in fibrillar adhesion. *The Journal of Adhesion*, 81(7-8):699–721, July 2005.

- [62] C Y Hui, N J Glassmaker, T Tang, and A Jagota. Design of biomimetic fibrillar interfaces: 2. mechanics of enhanced adhesion. *Journal of the Royal Society, Interface*, 1(1):35–48, November 2004.
- [63] C Y Hui, L Shen, A Jagota, and K Autumn. Mechanics of anti-fouling or self-cleaning in gecko setae. *Proceedings of the 29th Annual Meeting of The Adhesion Society*, pages 1–3, 2006.
- [64] D J Irschick, C C Austin, K Petren, R N Fisher, J B Losos, and O Ellers. A comparative analysis of clinging ability among pad-bearing lizards. *Biological Journal of the Linnean Society*, 59(1):21–35, September 1996.
- [65] D J Irschick, A Herrel, and B Vanhooydonck. Whole-organism studies of adhesion in pad-bearing lizards: creative evolutionary solutions to functional problems. *Journal of Comparative physiology. A, Neuroethology, Sensory, Neural, and Behavioral Physiology*, 192(11):1169–77, November 2006.
- [66] J Israelachvili. *Intermolecular and surface forces (2nd Ed.)*. Harcourt Brace and Co., London, UK, 1991.
- [67] H E Jeong, J K Lee, H N Kim, S H Moon, and K Y Suh. A nontransferring dry adhesive with hierarchical polymer nanohairs. *Proceedings of the National Academy of Sciences*, 106(14):5639–44, April 2009.
- [68] H E Jeong and K Y Suh. Precise tip shape transformation of nanopillars for enhanced dry adhesion strength. *Soft Matter*, 2012.
- [69] K L Johnson, K Kendall, and A D Roberts. Surface energy and the contact of elastic solids. *Proceedings of the Royal Society A: Mathematical, Physical and Engineering Sciences*, 324(1558):301–313, September 1971.
- [70] M Johnson, A Russell, and S Delannoy. *Functional surfaces in biology: chapter 5: the gekkonid adhesive system*, volume 2. Springer, Dordrecht, 2009.
- [71] J W Judy, R S Muller, and H H Zappe. Magnetic microactuation of polysilicon flexure structures. *Journal of Microelectromechanical Systems*, 4(4):162–169, 1995.
- [72] M Kamperman and A Synytska. Switchable adhesion by chemical functionality and topography. *Journal of Materials Chemistry*, 22(37):19390, 2012.
- [73] K Kendall. Thin film peeling - the elastic term. *Journal of Physics D: Applied Physics*, 8(13):1449, 1975.
- [74] S Kim, B Aksak, and M Sitti. Enhanced friction of elastomer microfiber adhesives with spatulate tips. *Applied Physics Letters*, 91(22):221913, November 2007.



- [75] S Kim, E Cheung, and M Sitti. Wet self-cleaning of biologically inspired elastomer mushroom shaped microfibrillar adhesives. *Langmuir*, 25(13):7196–9, July 2009.
- [76] S Kim, J Wu, A Carlson, S H Jin, A Kovalsky, P Glass, Z Liu, N Ahmed, S L Elgan, W Chen, P M Ferreira, M Sitti, Y Huang, and J A Rogers. Microstructured elastomeric surfaces with reversible adhesion and examples of their use in deterministic assembly by transfer printing. *Proceedings of the National Academy of Sciences*, 107(40):17095–17100, October 2010.
- [77] T W Kim and B Bhushan. Adhesion analysis of multi-level hierarchical attachment system contacting with a rough surface. *Journal of Adhesion Science and Technology*, 21(1):1–20, January 2007.
- [78] H Ko, J Lee, B E Schubert, Y L Chueh, P W Leu, R S Fearing, and A Javey. Hybrid core-shell nanowire forests as self-selective chemical connectors. *Nano letters*, 9(5):2054–8, May 2009.
- [79] E Kroner, R Maboudian, and E Arzt. Effect of repeated contact on adhesion measurements involving polydimethylsiloxane structural material. *IOP Conference Series: Materials Science and Engineering*, 5(1):012004, September 2009.
- [80] T S Kustandi, V D Samper, D K Yi, W S Ng, P Neuzil, and W Sun. Self-assembled nanoparticles based fabrication of gecko foot-hair-inspired polymer nanofibers. *Advanced Functional Materials*, 17(13):2211–2218, September 2007.
- [81] M K Kwak, C Pang, H E Jeong, H N Kim, H Yoon, H S Jung, and K Y Suh. Towards the next level of bioinspired dry adhesives: new designs and applications. *Advanced Functional Materials*, 21(19):3606–3616, October 2011.
- [82] D H Lee, Y Kim, R S Fearing, and R Maboudian. Effect of fiber geometry on macroscale friction of ordered low-density polyethylene nanofiber arrays. *Langmuir*, 27(17):11008–16, September 2011.
- [83] J Lee, B Bush, R Maboudian, and R S Fearing. Gecko-inspired combined lamellar and nanofibrillar array for adhesion on nonplanar surface. *Langmuir*, 25(21):12449–12453, 2009.
- [84] J Lee and R S Fearing. Contact self-cleaning of synthetic gecko adhesive from polymer microfibers. *Langmuir*, 24(19):10587–10591, October 2008.
- [85] J Lee, R S Fearing, and K Komvopoulos. Directional adhesion of gecko-inspired angled microfiber arrays. *Applied Physics Letters*, 93(19):191910, 2008.

- [86] J Lee, C Majidi, B Schubert, and R S Fearing. Sliding-induced adhesion of stiff polymer microfibre arrays. I. macroscale behaviour. *Journal of the Royal Society, Interface*, 5(25):835–844, August 2008.
- [87] J Li, M Zhang, L Wang, W Li, P Sheng, and W Wen. Design and fabrication of microfluidic mixer from carbonyl iron-PDMS composite membrane. *Microfluidics and Nanofluidics*, 10(4):919–925, October 2010.
- [88] C Majidi. Shear adhesion between an elastica and a rigid flat surface. *Mechanics Research Communications*, 36(3):369–372, April 2009.
- [89] C Majidi and R S Fearing. Adhesion of an elastic plate to a sphere. *Proceedings of the Royal Society A: Mathematical, Physical and Engineering Sciences*, 464(2093):1309–1317, May 2008.
- [90] C Majidi and R J Wood. Tunable elastic stiffness with microconfined magnetorheological domains at low magnetic field. *Applied Physics Letters*, 97(16):164104, October 2010.
- [91] C S Majidi, R E Groff, and R S Fearing. Attachment of fiber array adhesive through side contact. *Journal of Applied Physics*, 98(10):103521, 2005.
- [92] J C Mergel and R A Sauer. On the optimum shape of thin adhesive strips for various peeling directions. *The Journal of Adhesion*, page 130920154830009, September 2013.
- [93] S Momozono, K Nakamura, and K Kyogoku. Theoretical model for adhesive friction between elastomers and rough solid surfaces. *The Journal of Chemical Physics*, 132(11):114105, March 2010.
- [94] M P Murphy, B Aksak, and M Sitti. Gecko-inspired directional and controllable adhesion. *Small*, 5(2):170–5, February 2009.
- [95] M P Murphy, S Kim, and M Sitti. Enhanced adhesion by gecko-inspired hierarchical fibrillar adhesives. *Applied Materials & Interfaces*, 1(4):849–55, April 2009.
- [96] N Nadermann, J Ning, A Jagota, and C Y Hui. Active switching of adhesion in a film-terminated fibrillar structure. *Langmuir*, 26(19):15464–71, October 2010.
- [97] M T Northen, C Greiner, E Arzt, and K L Turner. A Gecko-Inspired Reversible Adhesive. *Advanced Materials*, 20(20):3905–3909, October 2008.
- [98] Y Otani, N Namiki, and H Emi. Removal of fine particles from smooth flat surfaces by consecutive pulse air jets. *Aerosol Science and Technology*, 23(4):665–673, 1995.

- [99] A Parness, D Soto, N Esparza, N Gravish, M Wilkinson, K Autumn, and M Cutkosky. A microfabricated wedge-shaped adhesive array displaying gecko-like dynamic adhesion, directionality and long lifetime. *Journal of The Royal Society, Interface*, 6(41):1223–1232, December 2009.
- [100] A M Peattie. Functional demands of dynamic biological adhesion: an integrative approach. *Journal of Comparative physiology. B, Biochemical, Systemic, and Environmental Physiology*, 179(3):231–9, April 2009.
- [101] A Peressadko, N Hosoda, and B Persson. Influence of surface roughness on adhesion between elastic bodies. *Physical Review Letters*, 95(12), September 2005.
- [102] B N J Persson. On the mechanism of adhesion in biological systems. *The Journal of Chemical Physics*, 118(16):7614, 2003.
- [103] B N J Persson. Biological adhesion for locomotion on rough surfaces: basic principles and a theorist’s view. *MRS bulletin*, 32(June), 2007.
- [104] A V Pocius. *Adhesion and Adhesive Technology*. Hanser, Munich, 2002.
- [105] N M Pugno. Towards a spiderman suit: large invisible cables and self-cleaning releasable superadhesive materials. *Journal of Physics: Condensed Matter*, 19(39):395001, October 2007.
- [106] N M Pugno and E Lepore. Observation of optimal gecko’s adhesion on nanorough surfaces. *BioSystems*, 94(3):218–22, December 2008.
- [107] J B Puthoff, M S Prowse, M Wilkinson, and K Autumn. Changes in materials properties explain the effects of humidity on gecko adhesion. *The Journal of Experimental Biology*, 213(Pt 21):3699–704, November 2010.
- [108] L Qu and L Dai. Gecko-foot-mimetic aligned single-walled carbon nanotube dry adhesives with unique electrical and thermal properties. *Advanced Materials*, 19(22):3844–3849, November 2007.
- [109] I Rodriguez, C T Lim, S Natarajan, A Y Y Ho, E L Van, N Elmouelhi, H Y Low, M Vyakarnam, and K Cooper. Shear adhesion strength of gecko inspired tapes on surfaces with variable roughness. *The Journal of Adhesion*, page 130305080341001, March 2013.
- [110] R Ruibal and V Ernst. The structure of the digital setae of lizards. *Journal of Morphology*, 117(3):271–93, November 1965.

- [111] A P Russell. A contribution to the functional analysis of the foot of the tokay, gekko gecko (Reptilia : Gekkonidae). *Journal of Zoological Society, London*, 176:437–476, 1975.
- [112] A P Russell. Descriptive and functional anatomy of the digital vascular system of the tokay, Gekko gecko. *Journal of Morphology*, 169(3):293–323, September 1981.
- [113] A P Russell. The morphological basis of weight-bearing in the scensors of the tokay gecko (Reptilia: Sauna). *Canadian Journal of Zoology*, 64:948–955, 1986.
- [114] A P Russell. Integrative functional morphology of the gekkotan adhesive system (reptilia: gekkota). *Integrative and Comparative Biology*, 42(6):1154–63, December 2002.
- [115] A P Russell and T E Higham. A new angle on clinging in geckos: incline, not substrate, triggers the deployment of the adhesive system. *Proceedings of The Royal Society. B. Biological Sciences*, 276(1673):3705–9, October 2009.
- [116] A P Russell and M K Johnson. Real-world challenges to, and capabilities of, the gekkotan adhesive system: contrasting the rough and the smooth. *Canadian Journal of Zoology*, 85(12):1228–1238, December 2007.
- [117] A P Russell and M K Johnson. Between a rock and a soft place: microtopography of the locomotor substrate and the morphology of the setal fields of Namibian day geckos (Gekkota: Gekkonidae: Rhoptropus ). *Acta Zoologica*, pages n/a–n/a, March 2013.
- [118] D Sameoto and C Menon. Recent advances in the fabrication and adhesion testing of biomimetic dry adhesives. *Smart Materials and Structures*, 19(10):103001, October 2010.
- [119] B Schubert, J Lee, C Majidi, and R S Fearing. Sliding-induced adhesion of stiff polymer microfibre arrays. II. microscale behaviour. *Journal of the Royal Society, Interface*, 5(25):845–853, August 2008.
- [120] B Schubert, C Majidi, R E Groff, S Baek, B Bush, R Maboudian, and R S Fearing. Towards friction and adhesion from high modulus microfiber arrays. *Journal of Adhesion Science and Technology*, 21(12):1297–1315, October 2007.
- [121] Su Sethi, Li Ge, L Ci, P M Ajayan, and A Dhinojwala. Gecko-inspired carbon nanotube-based self-cleaning adhesives. *Nano letters*, 8(3):822–825, March 2008.
- [122] M Sitti and R S Fearing. Synthetic gecko foot-hair micro/nano-structures as dry adhesives. *Journal of Adhesion Science and Technology*, 17(8):1055–1073, August 2003.
- [123] A M Smith, J A Callow, and K Autumn. *Biological Adhesives*. Springer Berlin Heidelberg, Berlin, Heidelberg, 2006.

- [124] R Spolenak, S Gorb, and E Arzt. Adhesion design maps for bio-inspired attachment systems. *Acta Biomaterialia*, 1(1):5–13, January 2005.
- [125] R Spolenak, S Gorb, H Gao, and E Arzt. Effects of contact shape on the scaling of biological attachments. *Proceedings of the Royal Society A: Mathematical, Physical and Engineering Sciences*, 461(2054):305–319, February 2005.
- [126] R Sriwijaya, A Rachmat, K Jatmiko, and K Takahashi. An analytical approach for the adhesion of a semi-infinite elastic body in contact with a sinusoidal rigid surface under zero external pressure. *Journal of Adhesion Science and Technology*, 21(10):899–909, 2007.
- [127] Y Tian, N Pesika, H Zeng, K Rosenberg, B Zhao, P McGuiggan, K Autumn, and J Israelachvili. Adhesion and friction in gecko toe attachment and detachment. *Proceedings of the National Academy of Sciences*, 103(51):19320–5, December 2006.
- [128] Y Tian, Ji Wan, N Pesika, and M Zhou. Bridging nanocontacts to macroscale gecko adhesion by sliding soft lamellar skin supported setal array. *Nature Publishing Group: Scientific Reports*, 3:1382, January 2013.
- [129] Y C Tsai, P J Shih, T H Lin, and W P Shih. Self-cleaning effects of biomimetic dry adhesives. In *IEEE Nano/Micro Engineered and Molecular Systems*, pages 1388–1391. IEEE, January 2006.
- [130] Bieke Vanhooydonck, Anemone Andronescu, Anthony Herrel, and Duncan J. Irschick. Effects of substrate structure on speed and acceleration capacity in climbing geckos. *Biological Journal of the Linnean Society*, 85(3):385–393, June 2005.
- [131] M Varenberg and S Gorb. Shearing of fibrillar adhesive microstructure: friction and shear-related changes in pull-off force. *Journal of the Royal Society, Interface*, 4(15):721–5, August 2007.
- [132] Z Varga, G Filipcsei, and M Zrínyi. Magnetic field sensitive functional elastomers with tuneable elastic modulus. *Polymer*, 47(1):227–233, January 2006.
- [133] R Vehring, C L Aardahl, E J Davis, G Schweiger, and D S Covert. Electrodynamical trapping and manipulation of particle clouds. *Review of Scientific Instruments*, 68(1):70, 1997.
- [134] I M Ward. Review: the yield behaviour of polymers. *Journal of Materials Science*, 6(11):1397–1417, November 1971.
- [135] M A Wilding and I M Ward. Creep and recovery of ultra high modulus polyethylene. *Polymer*, 22(7):870–876, July 1981.

- [136] B K P Wong, S K Sinha, J P Y Tan, and K Y Zeng. Nano-wear mechanism for ultra-high molecular weight polyethylene (UHMWPE) sliding against a model hard asperity. *Tribology Letters*, 17(3):613–622, October 2004.
- [137] K Xu, R Vos, G Vereecke, G Doumen, W Fyen, P W Mertens, M M Heyns, C Vinckier, and J Fransaer. Particle adhesion and removal mechanisms during brush scrubber cleaning. *Journal of Vacuum Science & Technology B: Microelectronics and Nanometer Structures*, 22:2844–52, 2004.
- [138] L Xue, A Kovalev, F Thöle, G T Rengarajan, M Steinhart, and S N Gorb. Tailoring normal adhesion of arrays of thermoplastic, spring-like polymer nanorods by shaping nanorod tips. *Langmuir*, 28(29):10781–8, July 2012.
- [139] T Yamaguchi, N Gravish, K Autumn, and C Creton. Microscopic modeling of the dynamics of frictional adhesion in the gecko attachment system. *The Journal of Physical Chemistry B*, 113(12):3622–3628, March 2009.
- [140] H Yao and H Gao. Mechanics of robust and releasable adhesion in biology: Bottom up designed hierarchical structures of gecko. *Journal of the Mechanics and Physics of Solids*, 54(6):1120–1146, June 2006.
- [141] B Yurdumakan, N R Raravikar, P M Ajayan, and A Dhinojwala. Synthetic gecko foot-hairs from multiwalled carbon nanotubes. *Chemical Communications*, 1(30):3799–801, August 2005.
- [142] P A Zani. The comparative evolution of lizard claw and toe morphology and clinging performance. *Journal of Evolutionary Biology*, 13(2):316–325, March 2000.
- [143] H Zeng, N Pesika, Y Tian, B Zhao, Y Chen, M Tirrell, K L Turner, and J Israelachvili. Frictional adhesion of patterned surfaces and implications for gecko and biomimetic systems. *Langmuir*, 25(13):7486–95, July 2009.
- [144] X Zhang, B Kong, O K C Tsui, X Yang, Y Mi, C M Chan, and B Xu. Effect of pattern topology on the self-cleaning properties of textured surfaces. *The Journal of Chemical Physics*, 127(1):14703, July 2007.
- [145] Yi Zhang, C W Lo, J A Taylor, and S Yang. Replica molding of high-aspect-ratio polymeric nanopillar arrays with high fidelity. *Langmuir*, 22(20):8595–601, September 2006.